KERR SWITCHING FOR TEMPORAL NOISE FILTERING IN OPTICAL TELECOM QUANTUM COMMUNICATION

TIMOTHY LEE

Thesis submitted to the University of Ottawa
in partial fulfillment of the requirements for the degree of
Master of Science in Physics

Under the supervision of
Jeff S. Lundeen

Department of Physics
Faculty of Science
University of Ottawa

uOttawa

Abstract

Implementing quantum key distribution in existing optical telecommunication infrastructure requires the employment of appropriate spatial, spectral, and temporal filtering to achieve high tolerance to noise from classical optical signals present in fibre networks. Electronic temporal filtering may be limited by the nanosecond-scale timing jitter of typical single-photon detectors; this requires us to use faster physical processes to rapidly gate the desired optical signal, while rejecting random noise photons arriving outside of a narrow passing window.

In this work, we use ultrashort optical pulses to implement a Kerr switch in a 1-metre length of single-mode fibre to perform all-optical temporal filtering of noise in a telecom-wavelength quantum channel. Using our switch, we demonstrate 2.4-ps temporal gating of 1.3 µm-wavelength signal photons with a near-unity switching efficiency of $98.77 \pm 0.01\%$. We also show that our switch can be used as an effective ultrafast temporal filter capable of reducing noise introduced into a quantum channel by up to 18.2 dB.

Acknowledgements

First, I would like to first thank my supervisor, Jeff Lundeen, for his mentorship throughout this project. His enthusiasm for science and emphasis on clarity in communication continue to inspire me. Above all, I am grateful for his patience, understanding, and feedback as I strive to develop myself as a researcher.

I thank all past and present members of the Lundeen Lab for fostering a supportive atmosphere in the group, whether it means providing insights during meetings, sanity-checking experimental setups in the lab, or engaging with each other during social outings. I look forward to further opportunities to work with everyone in the years ahead.

Throughout this project, I had the pleasure of collaborating with many wonderful researchers through the National Research Council-University of Ottawa Joint Centre for Extreme Photonics. I would like to thank Ben Sussman, Phil Bustard, Duncan England, Frédéric Bouchard, and Kate Fenwick, whose experience and guidance were essential in determining the best way forward. I am fortunate to have worked directly with several other key individuals in the lab who I would like to thank, including Andrew Proppe, James Hubble, and Alicia Sit.

I would like to thank my family for their love and support throughout my academic endeavours.

Lastly, I would like to acknowledge the financial support I received from the Natural Sciences and Engineering Research Council (NSERC) during my master's program.

Contributions

The work presented in this thesis is the result of contributions from many individuals. The original idea for this project arose from discussions primarily between Jeff Lundeen and members of the National Research Council (NRC) Ultrafast Quantum Optics group, including Benjamin Sussman, Philip Bustard, Duncan England, and Frédéric Bouchard; it was one of many project ideas suggested to build off the recent work in references [1–3]. These individuals provided ongoing guidance and feedback at all stages of the project timeline.

The background information and theory provided throughout Chapters 1 and 2 is summarized from existing published work, primarily references [1, 2], and [4–7]. Fig. 2.2 is reproduced from reference [7][a]. Figures 2.3 and 2.4 were created using a MATLAB script based on code provided by Kate Fenwick, with minor modifications made by me.

The idea of using a photonic crystal fibre (PCF) as a wavelength-tunable signal source using supercontinuum generation was suggested by Philip Bustard. The PCF we used was supplied by Photonics Bretagne and was custom-designed for our application. The two PCF samples described in Section 3.2.1 were prepared by Huimin Ding at the NRC who cleaved the 30-cm lengths of fibre and spliced on the end pieces. Huimin Ding also provided the images in Fig. 3.2, which have been reproduced with permission.

The experimental setup in Chapter 3 was primarily assembled by myself, with assistance from James Hubble and Andrew Proppe. Andrew Proppe also wrote a Python script to control the motorized translation stage and interface with the single photon detection

[a]Reproduced with the permission of Elsevier Science & Technology Journals; permission was conveyed through Copyright Clearance Center, Inc.

electronics, which facilitated data collection. Denis Guay of the NRC provided ongoing assistance and troubleshooting with laboratory infrastructure, including the cooling systems for the single photon detectors and femtosecond laser, and built the acrylic enclosure for the PCF sample used in the setup. All data leading to the results depicted in Chapters 3 and 5 was collected by me.

I wrote the script described in Chapter 4 to model the evolution of the Kerr switch pump field, following a split-step Fourier method prescription suggested in reference [7]. The script which models the full behaviour of the Kerr switch, accounting for pump pulse evolution, was written by me with the addition of some elements adapted from the simple numerical model provided by Kate Fenwick. Both scripts are provided in Appendix A. The background content in Chapter 4 is largely drawn from reference [7].

All figures in this thesis were created by me, unless otherwise cited. Figures 2.1 and 3.1 were made using elements from ComponentLibrary by Alexander Franzen.[b]

[b]Available at https://www.gwoptics.org/ComponentLibrary/ under a Creative Commons Attribution-NonCommercial 3.0 Unported License: https://creativecommons.org/licenses/by-nc/3.0/.

Table of contents

List of Figures

List of Tables

Chapter 1

Introduction

1.1 Motivation

The emerging fields of quantum technologies promise new paradigms in computation, communication, encryption, and metrology by exploiting the laws of quantum mechanics [8]. The Government of Canada's National Quantum Strategy recognizes the potential of such technologies to disrupt and transform how Canadians live and do business, and highlights the importance of enabling Canadian academia and industry to work towards practical implementation of such systems and devices. In particular, it establishes the specific mission of "[ensuring] the privacy and cyber-security of Canadians in a quantum-enabled world through a national secure quantum communications network and a post-quantum cryptography initiative" [9].

What *is* a quantum communications network? As the term suggests, it must be capable of transmitting some sort of quantum mechanical entity—carrying a piece of information—from one location to the other. These information carriers should behave quantum mechanically, be able to travel quickly, and have a reasonable chance of actually arriving from a sender to a receiver. It so happens that photons—individual quanta of light—fulfill these requirements quite readily. Information can be easily encoded onto a photon, namely in its polarization

state [4], using optical components commonly available in laboratory and commercial settings. Moreover, photons travel fast (literally at *light-speed*), and can be transmitted over large distances through free space or optical fibres with relatively low loss [10].

In the digital era, secure communications are a critical area of concern given that many data transactions involve sensitive information. The security of conventional encryption protocols such as Rivest–Shamir–Adleman (RSA) typically depends on the assumption that it is difficult for classical computers to factorize very large numbers [11, 12]. However, such schemes may be vulnerable to future advances in technology. In particular, Shor's algorithm has been proposed as a method for efficient factorizing integers using a quantum computer [13]. In the event that Shor's algorithm is successfully implemented on a quantum computer, even encrypted data that has been stored for a long time may retroactively become vulnerable to decryption by an unauthorized, potentially adversarial, eavesdropper [12]. Quantum key distribution (QKD)[4] has been proposed as a means of performing cryptography with long-term unconditional security by leveraging the laws of quantum mechanics [12].

Fibre-based QKD has been of particular interest due to the widespread availability of optical fibres used for telecommunications purposes. An economic argument can be made that existing telecommunications (telecom) infrastructure could be used to implement quantum channels, which would enable low-cost, practical implementation of QKD [14]. However, it must be emphasized that QKD is implemented at the scale of single photons. Given that telecom fibre networks often accommodate not just one, but many wavelength-separated optical channels [10], there may be plenty of residual light present within such a system which acts as noise and can contaminate a quantum signal and cause errors in measurement [14, 15].

With this in mind, the overarching goal of this project is to implement a filter to remediate the impact of noise present in an optical quantum channel. In Section 1.2, we provide relevant background information to establish the context for this work. We begin with a conceptual overview of quantum cryptography, primarily based on established theory pro-

vided in references [4] and [5], before moving on to discuss the impact of noise in real-world fibre-based implementations of QKD. Next, we will introduce the concept of using optical Kerr switching as a means of temporally filtering out noise in a quantum channel, based on recent literature from collaborators. Section 1.3 provides an outline for the rest of the thesis.

1.2 Principles of quantum key distribution

We first provide a theoretical overview/review of QKD in order to motivate the idea of communicating information on single photons. For our purposes, we will study the archetypal QKD protocol developed in 1984 by Bennett and Brassard which has come to be known as BB84 [4]. Although there are many different quantum key distribution protocols which use different methods of optically encoding quantum information [14], discussing BB84 will be sufficient for motivating the design of our noise filter.

Suppose a private message is to be communicated between two persons; a sender, often referred to as "Alice," and a receiver, "Bob." A provably secure method of encrypting the desired message is to use a one-time pad [16]. As depicted in Fig. 1.1, this procedure involves generating a randomized "key," consisting of a sequence of letters or numbers which is the same length as the message to be encrypted. After generating the key, Alice use modular arithmetic to add each entry of the key to the corresponding entry in the original message. The resulting encrypted message is a sequence of entries that appears to be as random as the key itself. Alice can then send the key to Bob over a private, secure channel (i.e. a communication medium), while the encrypted message can be safely be sent to Bob over a public channel. As long as the private channel over which the key is sent is truly secure and free from outside interception, Bob can then subtract the key from the encrypted message to recover the original without any risk of the message being read by an outside observer. Crucially, only the key itself needs to be sent privately for this scheme to work. The central idea behind BB84 is to generate and send such a key for encrypting digital

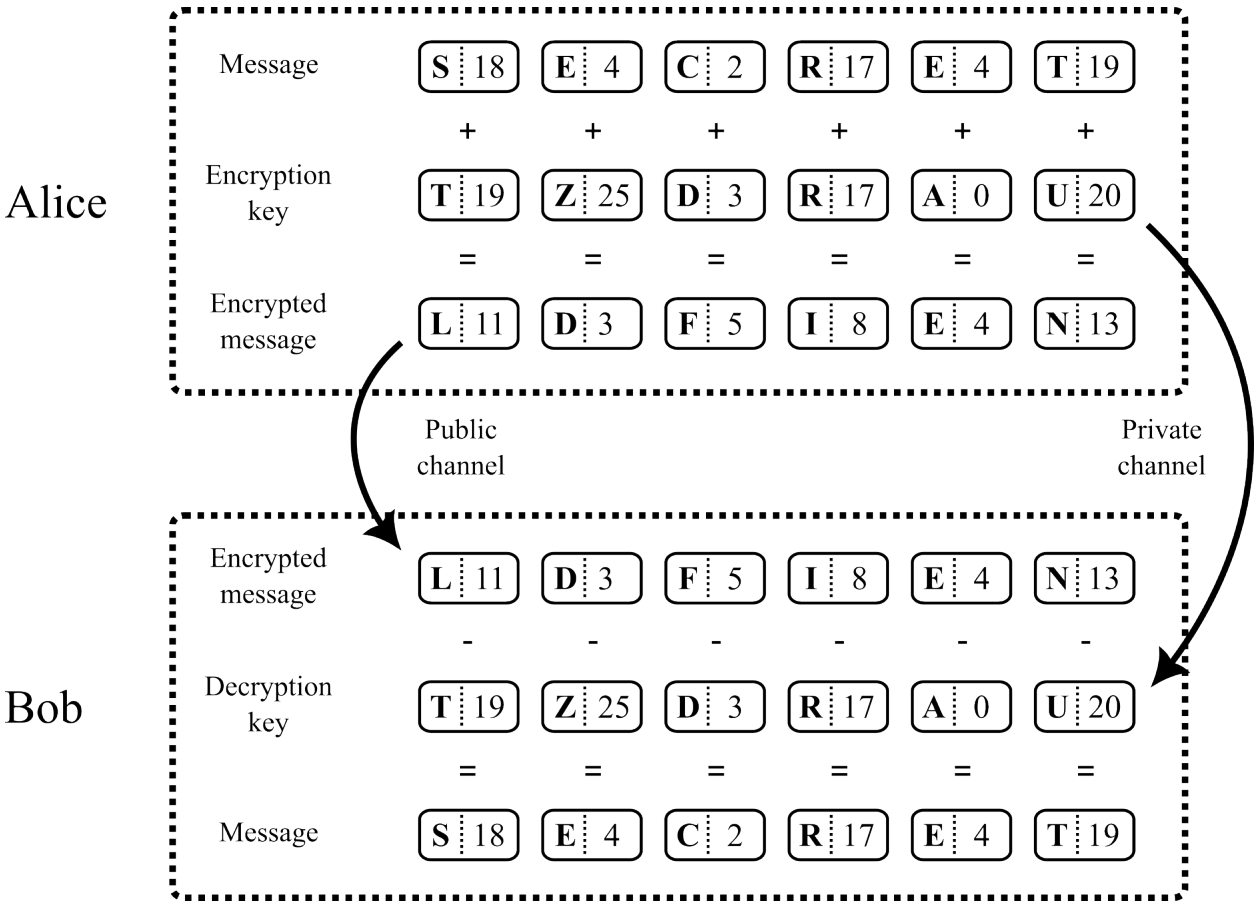

Figure 1.1: An example of encryption using a one-time pad. The letters of the alphabet A to Z are assigned numbers in order from 0 to 25. Each letter in the key string ("TZDRAU") is individually added to the corresponding letter in the message string ("SECRET") with modulo 26 to produce the encrypted message. The encrypted message may be safely sent via a public channel, while the key must be kept secret and shared only through a private/secure channel. The original message is retrieved by subtracting the same key letter-by-letter from the encrypted message.

(binary) information, while ensuring that the private channel is secure [4].

In classical communication, digital information is comprised of "bits" which have definitive values of either 0 or 1. In quantum communication, information is instead comprised of "quantum bits" or "qubits." A qubit's quantum state $|\psi\rangle$ is mathematically described as a superposition between two states representing 0 and 1:

$$|\psi\rangle = c_0 |0\rangle + c_1 \beta |1\rangle , \tag{1.1}$$

where c_0 and c_1 are the complex probability amplitudes which satisfy $|c_0|^2 + |c_1|^2 = 1$. As their name suggests, they define the relative probability of measuring a single qubit to be in states $|0\rangle$ or $|1\rangle$. The set of orthogonal states $\{|0\rangle, |1\rangle\}$ is also referred to as the "computational" basis [5].

Qubits can be encoded in the polarization state of a photon, which defines the transverse direction of the electric field oscillation, relative to the direction of propagation. The state of a photon can be described as a superposition between two linear polarizations in an orthogonal basis:

$$|\psi\rangle_+ = c_H |H\rangle + c_V |V\rangle , \tag{1.2}$$

or,

$$|\psi\rangle_\times = c_D |D\rangle + c_A |A\rangle . \tag{1.3}$$

Here we consider two such bases: the "rectilinear" (+) basis $\{|H\rangle, |V\rangle\}$ which represents horizontal (H, $\rightarrow$) and vertical (V, $\uparrow$) polarizations; and the "diagonal" ($\times$) basis $\{|D\rangle, |A\rangle\}$ which represents diagonal (D, $\nearrow$) and anti-diagonal (A, $\nwarrow$) polarizations. The diagonal basis is off-set from the rectilinear basis by 45°. The polarization of a photon can be rotated between any 4 of these states using a half-wave plate (HWP). For each choice of polarization basis, the basis states can be directly assigned to a corresponding state in the computational basis. Explicitly, we can choose $|H\rangle$ and $|D\rangle$ to both correspond to $|0\rangle$, and $|V\rangle$ and $|A\rangle$ to

both correspond to $|1\rangle$.

Suppose Alice wishes to send a single bit, either 0 or 1, to Bob using polarization encoding. She first decides which basis (+ or $\times$) to prepare the photon in, then can use a half-wave plate to rotate the photon polarization to the desired direction (H or D for 0, V or A for 1). Meanwhile, Bob has a polarizing beamsplitter (PBS) which transmits horizontally-polarized photons and reflects vertically-polarized photons with 100% probability, sending them to different photodetectors. This allows him to project $|H\rangle$ and $|V\rangle$ onto the computational basis states $|0\rangle$ and $|1\rangle$, respectively: if he detects a transmitted photon, he records a "0"; if he detects a reflected photon, he records a "1." However, if a diagonally- or anti-diagonally-polarized photon arrives at the PBS it will instead be reflected or transmitted with 50:50 probability, and thus have an equal chance of corresponding to a 0 or 1. Bob can use a HWP before the PBS to add a 45° offset to the incoming polarization, allowing him to instead project $|D\rangle$ onto $|0\rangle$ and $|A\rangle$ onto $|1\rangle$; in this case, a photon that is initially either H- or V-polarized would now result in a measurement of 0 or 1 with 50:50 probability. In other words, Bob uses the HWP to choose a linear basis for detection, just as Alice selects a basis for preparation. If he and Alice share the same basis, then they should agree whether a 0 or 1 was sent with 100% probability; otherwise, they will disagree 50% of the time.

Alice and Bob can now generate a secret key using the BB84 protocol as follows [4]:

1. Alice first prepares a random sequence of bits.

2. For each bit, she randomly chooses a linear basis (+ or $\times$), prepares the photon in the appropriate polarization, and sends it to Bob along a secure channel.

3. For each incoming photon, Bob randomly chooses a linear basis (+ or $\times$), and records the resulting measurement.

4. Over another channel (which may be public), Alice and Bob share the sequence of bases they used to prepare and measure each qubit.

5. They discard any bits for instances when they did not agree on the basis. The remaining bits are used to form their one-time pad secret key.

An example of this procedure is depicted in Table 1.1.

An eavesdropper, Eve, attempting to clandestinely intercept the secret key would need to have access to the private channel over which Alice and Bob are sending their photons, measure the states prepared by Alice, then send perfect copies of Alice's photons to Bob in order to avoid detection. However, the no-cloning theorem in quantum information states that it is impossible to generate a complete copy of an unknown or arbitrary quantum state [4, 5, 17]. Therefore, Eve cannot determine with certainty the quantum state of a given qubit since she does not know *a priori* the basis chosen by Alice, and because it is impossible to copy the qubit's quantum state to try and measure it in multiple bases. Since there is also only a 50% chance that Eve will measure in the same basis as Bob, she cannot reliably send him a spoofed sequence of bits based on her own measurements.

Alice and Bob can therefore verify the security of their channel, and hence their key, by sharing a portion of the bits they each have left over after Step 5. If there are unexpected disagreements in the bits which share the same basis, then they conclude that the errors are a result of Eve's attempts to intercept their key and that their channel is therefore not secure. They would then discard all the shared bits, switch to a new channel, and attempt to generate a new key.

1.2.1 Noise in fibre-based QKD

The above theoretical implementation of QKD assumes Alice and Bob have access to a perfect channel which is free of communication errors. Given that a one-time pad is required to be as long as the message to be encrypted, a practical QKD network should produce secret keys with a generation rate comparable to the rate of classical information transmission. However, real-world implementations of QKD face challenges which ultimately impact the rate at which secret keys can be generated, such as channel loss or noise [14, 18, 19].

Alice's random bits	1	1	0	0	1	1	0	1
Alice's source basis	D/A	H/V	H/V	H/V	H/V	D/A	D/A	D/A
Alice's photon polarizations	↖	↑	→	→	↑	↖	↗	↖
Bob's measurement basis	H/V	D/A	H/V	H/V	D/A	D/A	H/V	D/A
Bob's measured bits	1	0	0	0	0	1	0	1
Alice and Bob's secret key			0	0		1		1

Table 1.1: Example of BB84 quantum key distribution protocol using polarization encoding. Bold columns indicate bits for which Alice and Bob share the same basis for state preparation and measurement. Errors in Bob's measurements are indicated in red. Alice and Bob reject any bits where they used different bases for photon preparation and measurement.

In the context of QKD, "noise" primarily refers to extraneous light entering the quantum channel. Because QKD relies on the reliable detection of single photons, even low-intensity ambient light can cause errors in measurements. This poses a challenge for implementing QKD, since communication errors between Alice and Bob could be the result of channel noise instead of indicating the presence of an eavesdropper. Although QKD protocols can be employed which are resistant to noise and loss, the presence of these errors will limit possible secret key rates [20–23].

Optical fibres have been well-studied as a medium for implementing QKD, and have much greater stability and lower cost compared to free-space systems (e.g. satellites) [14]. Fibre-based QKD systems have been demonstrated over distances of hundreds of kilometres, making them suitable for inter-city use [24–26]. However, demonstrations have mostly been performed using dedicated lengths of "dark" fibre (i.e. fibre which is free of any classical signals) laid over these distances, which is costly. The economic attractiveness of fibre-based QKD could be improved by using pre-existing fibre infrastructure already in use for classical telecommunication purposes. Selecting a common telecommunications wavelength, such as in the O-band region near 1.3 µm or the C-band region near 1.55 µm, may also enable

compatibility with many commercially-available components. These wavelengths also benefit from being in the low-dispersion and/or low-loss regimes of typical commercial fibres such as SMF-28. However, fibres are often used to support many coexisting classical signals on wavelength-separated channels which can introduce significant ambient noise. Enabling QKD signals to coexist with classical signals would require methods of substantially reducing the ambient noise in the quantum channel to levels acceptable for viable secret key generation rates [21].

1.2.2 Temporal noise filtering

Filtering out noise amounts to preventing any unwanted photons from reaching Bob's detectors. This can be achieved through three approaches: spatial, spectral, and temporal filtering. Single-mode optical fibres themselves act as good spatial filters by restricting the path, or optical mode, of the photons reaching the detectors. Spectral filtering entails choosing and employing spectral filters which attenuate any light from wavelengths different from that of the signal. In order to eliminate remaining noise, temporal filtering can be employed in which a noisy signal is gated by limiting the window of time during which a photon can be detected. Spectral and temporal filtering is conceptually depicted in Fig. 1.2. To maximize noise elimination, Bob may position such filters in front of each of his detectors as illustrated in Fig. 1.3. Although time gating could be achieved using detection electronics, typical single-photon detectors can have timing jitters on the order of nanoseconds, and the presence of noise can limit the overall detection rates (and hence secret key rates) due to finite detector reset times [1]. In order to improve temporal gating, faster physical processes must be used to restrict photon detection.

Rather than using electronic approaches, we propose to use ultrafast optical effects in order to temporally gate a quantum signal using femtosecond pulses in a process known as Kerr switching. In a Kerr switch setup, a strong pump pulse and a weak signal pulse with different wavelengths propagate through a material with a nonlinear refractive index, such

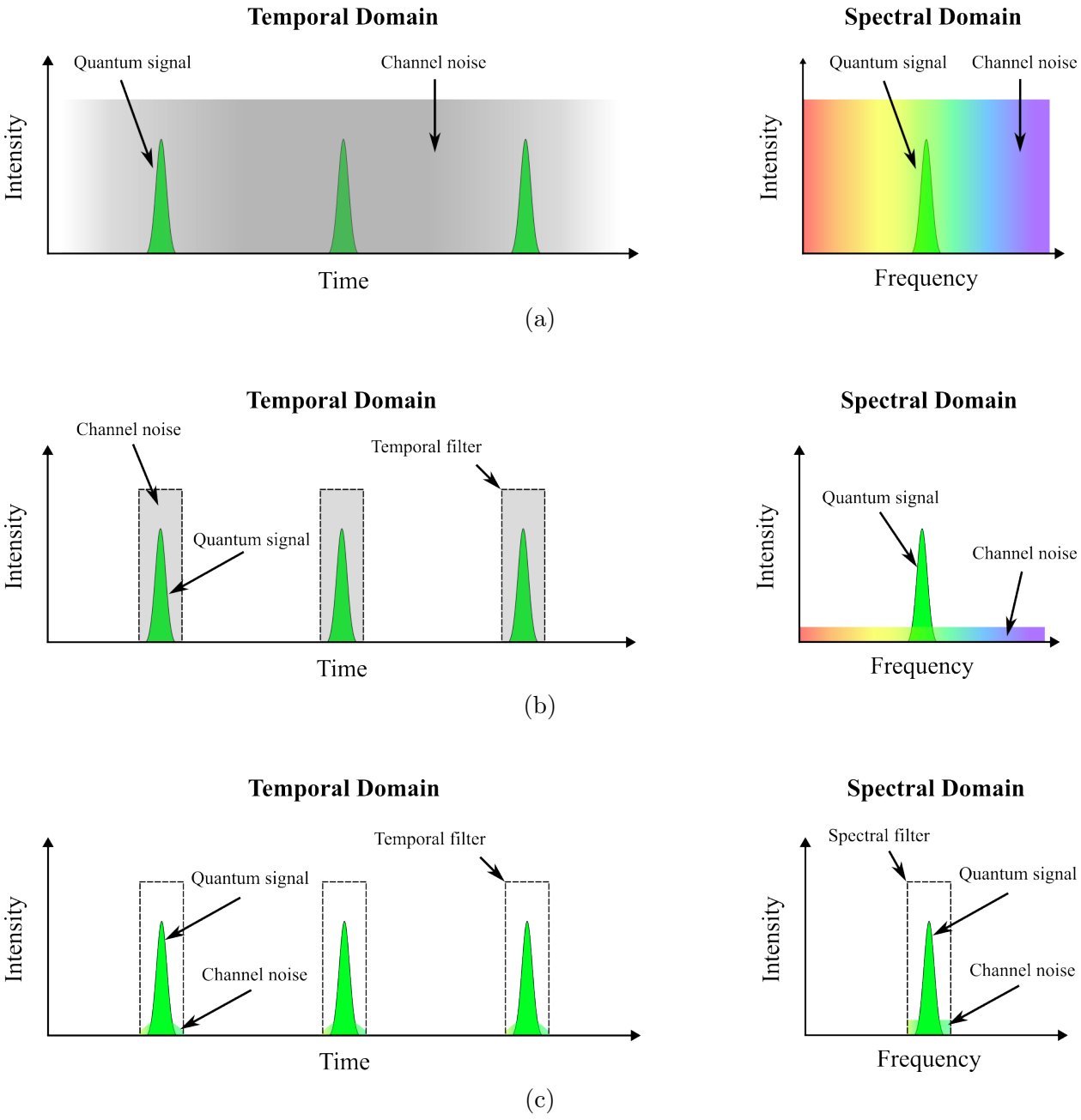

Figure 1.2: Depiction of temporal and spectral filtering in a noisy quantum channel. (a) The quantum signal consists of a train of pulses which have a well-defined temporal and spectral profile, while the channel noise is randomly distributed in both time and frequency. (b) A periodic temporal filter is first used to gate the signal, eliminating noise which falls outside of the pass window. However, the remaining noise is still randomly distributed in frequency. (c) A spectral filter is subsequently applied to eliminate noise outside of the pass band. The remaining noise consists only of the few photons that coincide with the temporal and spectral filter windows.

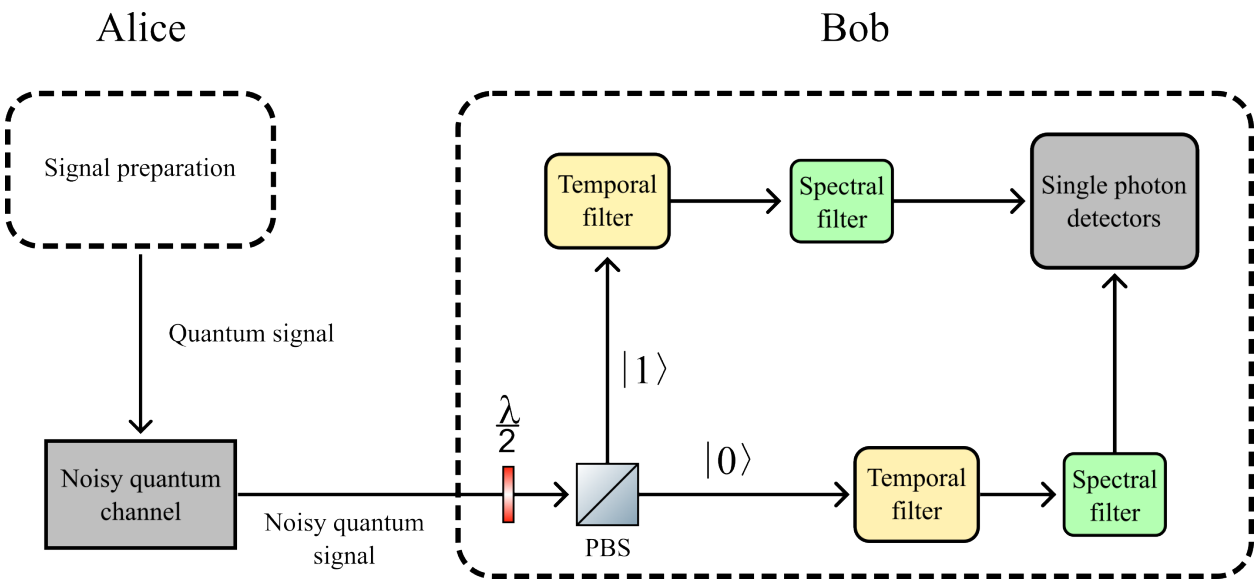

Figure 1.3: Conceptual signal flow for noise filtering in polarization-encoded BB84. Bob rotates a half-wave plate to change between H/V and D/A bases, and implements temporal and spectral filtering stages for each orthogonal state in the chosen measurement basis. PBS: polarizing beamsplitter; $\lambda/2$: half-wave plate.

as a silica fibre. As the pulses walk through each other due to the group velocity mismatch, the presence of the pump causes the polarization of the signal pulse to rotate. Recent work has shown potential of using Kerr switching to rapidly rotate the polarization of a 720.8 nm signal photon, allowing for gating of photons based on their switched polarization state while rejecting extraneous noise photons. This gating is performed within a picosecond-scale window, representing a 10^3-fold improvement over conventional electronics. It was also shown that using this Kerr switch-based temporal filter in a QKD experiment results in significant improvement in secret key rates across various levels of channel noise and loss [1, 2]. In this work, we show that a similar Kerr switch design can also be implemented for telecom wavelengths, and subsequently use it temporally filter out noise in a quantum communication channel.

1.3 Outline

Chapter 2 discusses the theoretical background necessary to understand the principles of Kerr switching, including an overview of relevant nonlinear optical phenomena, and presents a simple numerical model for predicting the experimental performance of the switch. In Chapter 3, we describe the experimental setup, provide preliminary results for switching C- and O- band signals, and indicate challenges that arose due to noise intrinsic to the Kerr switch itself. Chapter 4 presents further numerical modeling of the Kerr switch, which was performed to better understand how to reduce this intrinsic noise. In Chapter 5, we implement the lessons learned from numerical modeling in our experimental setup to improve the Kerr switch performance, and we provide results demonstrating temporal noise filtering in a telecom quantum channel. Chapter 6 provides final remarks and an outlook on future work. Finally, Appendix A contains MATLAB scripts for the numerical models discussed in Chapter 4.

Chapter 2

Theory of all-optical Kerr switching

2.1 Summary

Before we can construct a Kerr switch, we must first understand the underlying phenomena which gives rise to all-optical Kerr switching. In this chapter, we review relevant concepts in nonlinear optics based on established theory and provide background information largely drawn from references [1, 2] and [6, 7]. Next, we use a simple numerical model to simulate Kerr switching in order to determine necessary restrictions on key experimental parameters. This knowledge is used to build the setup later described in Chapter 3.

All-optical Kerr switching relies on the use of nonlinear optical effects. The study of nonlinear optics is based around the central idea that the optical response of a material is *nonlinear* relative to the amplitude of an applied electric field. In the limit where the material response is instantaneous, the dependence of the induced dipole moment per unit volume, or polarization, $P(t)$ can be written as a power series expansion in terms of a time-varying electric field $E(t)$ as [6]:

$$\tilde{P}(t) = \epsilon_0 \left[\chi^{(1)}E(t) + \chi^{(2)}E(t)^2 + \chi^{(3)}E(t)^3 + ...\right] \tag{2.1}$$

where ϵ_0 is the permittivity of free space. $\chi^{(1)}$ is the linear susceptibility of the material, and

$\chi^{(2)}$ and $\chi^{(3)}$ are the second- and third-order nonlinear optical susceptibilities (and so on).

The values of $\chi^{(i)}$ depend on the material structure. For example, if the material is centrosymmetric, as is the case in fused silica fibres, then the second-order term with $\chi^{(2)}$ vanishes [7]. Although Eq. 2.1 is written in terms of scalar values for simplicity, in reality, the polarization and electric field are vectors, with the $\chi^{(i)}$ being expressed as tensors of rank i.

The relationship described by Eq. 2.1 is responsible for many different nonlinear optical effects which can be observed at high optical field intensities characteristic of ultrafast pulses, such as self-phase modulation (SPM), cross-phase modulation (XPM), four-wave mixing (FWM), sum- and difference-frequency generation, and so on. Of these, SPM and XPM are the most important for this work. Later sections in this chapter will provide an overview of how SPM and XPM arise as third-order nonlinear optical processes, and how all-optical polarization switching can be achieved using XPM.

2.2 Gaussian pulses

Throughout this work, we will frequently be discussing the evolution of optical pulses with a finite temporal width, as opposed to continuous-wave (CW) optical fields with a constant intensity. For simplicity, it is often useful to define time with respect to the moving reference frame of a pulse, rather than the "laboratory" or "rest" frame. The time in this moving frame T is related to time in the laboratory frame t and propagation distance z through:

$$T = t - \frac{z}{v_g} \tag{2.2}$$

where v_g is the group velocity of the pulse. For the remainder of the theory section, we assume that our optical pulses are Gaussian in time so that the intensity I has the general

form:

$$I(T) = I_0 \exp\left(-4 \ln 2 \, \frac{T^2}{T_{\text{FWHM}}^2}\right) \tag{2.3}$$

where T_{FWHM} is the temporal full width at half maximum (FWHM) of the pulse, and I_0 is the peak intensity. Critically, this should not be confused with a related quantity often called the "temporal width" of the pulse, $T_0 = 2\sqrt{\ln 2}\, T_{\text{FWHM}}$ which is the time between the peak and the $1/e^2$ intensity points. Similarly, the spectral width $\Delta\omega$ describes the spectral width from the peak intensity to the and the $1/e^2$ intensity points of the pulse in the spectral domain and satisfies $\Delta\omega T_0 = 1$ [7]. For clarity, this text will refer to T_{FWHM} as the "temporal FWHM" and T_0 as the "temporal $1/e^2$ width."

Note that if the pulse duration is sufficiently short relative to the material response time, then the susceptibilities $\chi^{(i)}$ in Eq. 2.1 must be treated as time-dependent. It may then be necessary to analytically or numerically solve a differential equation to accurately study the evolution of the optical pulse. This is explored in further detail in Chapter 4. However, the instantaneous response approximation is still useful for examining the optical Kerr effect, SPM, and XPM in the subsequent sections.

2.3 Optical Kerr effect

If a material has a non-zero third-order nonlinear susceptibility $\chi^{(3)}$, an optical field can experience an effective "total" refractive index n which varies with the field intensity I [6]. This is quite contrary to the situation in linear optics, where the refractive index is independent of the intensity of light. The dependence of the refractive index on the incident field intensity is referred to as the optical Kerr effect [7], and we can refer to the material we use to generate this effect as a "Kerr medium." In this section, we provide a mathematical description of the Kerr effect as presented in references [6] and [7].

The effective refractive index obeys the relationship:

$$n = n_0 + n_2 I. \tag{2.4}$$

Here, n_0 is the linear refractive index (i.e. that experienced by a field in the low-intensity limit), and n_2 is the nonlinear index coefficient, or Kerr coefficient. To understand how this effect comes about due to third-order nonlinearity, we can derive an expression for n_2 in terms of $\chi^{(3)}$. We start by considering a monochromatic electric field of the form

$$E(t) = \mathcal{E} \cos \omega_0 t \tag{2.5}$$

propagating through a Kerr medium. Although this expression does not quite accurately represent a Gaussian pulse, this treatment assumes for simplicity that the electric field envelope of the optical field varies very slowly relative to the oscillation frequency ω_0, so that it is approximately constant over a few cycles of oscillation. The intensity I of the field is related to the electric field amplitude $\mathcal{E}$ through:

$$I = \frac{1}{2} n_0 \epsilon_0 c \mathcal{E}^2. \tag{2.6}$$

The third-order term for the induced nonlinear polarization is then given by

$$P^{(3)}(t) = \epsilon_0 \chi^{(3)} \mathcal{E}^3 \cos^3 \omega_0 t. \tag{2.7}$$

We can use the identity $\cos^3 x = \frac{1}{4} \cos 3x + \frac{3}{4} \cos x$ to rewrite the above as:

$$P^{(3)}(t) = \epsilon_0 \chi^{(3)} \mathcal{E}^3 \left(\frac{1}{4} \cos 3\omega_0 t + \frac{3}{4} \cos \omega_0 t \right). \tag{2.8}$$

The first term here corresponds to third-harmonic generation (THG), in which a field with frequency $3\omega_0$ is generated. In practice, phase-matching is required for THG to build up

significantly, so we can ignore this term and keep only the term with frequency ω_0 [7].

Assuming an isotropic Kerr medium (i.e. $\chi^{(2)} = 0$), the total induced polarization up to third-order can therefore be written as [6]:

$$P_{\text{tot}}(t) = \epsilon_0 \left(\chi^{(1)} + \frac{3}{4}\chi^{(3)}\mathcal{E}^2 \right) \mathcal{E} \cos \omega_0 t = \epsilon_0 \chi_{\text{eff}} E(t), \tag{2.9}$$

where we introduce

$$\chi_{\text{eff}} = \chi^{(1)} + \frac{3}{4}\chi^{(3)}\mathcal{E}^2 \tag{2.10}$$

as an "effective" susceptibility which relates the polarization $P(t)$ to the field $E(t)$. The effective susceptibility χ_{eff} is related to the overall refractive index n through [6]:

$$n^2 = 1 + \chi_{\text{eff}}. \tag{2.11}$$

Using Eqs. 2.4 and 2.10, we can write:

$$(n_0 + n_2 I)^2 = 1 + \chi^{(1)} + \frac{3}{4}\chi^{(3)}\mathcal{E}^2. \tag{2.12}$$

Expanding the left-hand side using Eq. 2.6, and noticing that $n_0^2 = 1 + \chi^{(1)}$ from linear optics, we can write:

$$n_0^2 + 2n_0 n_2 I + n_2^2 I^2 = n_0^2 + \frac{3}{2n_0\epsilon_0 c}\chi^{(3)} I. \tag{2.13}$$

Because the value of n_2 is generally quite low (cf. Table 2.1), $n_2^2 I^2$ is sufficiently small that we can ignore this term on the left-hand side and only keep the terms up to first-degree in I. By direct comparison, we can see that:

$$n_2 = \frac{3}{4n_0^2\epsilon_0 c}\chi^{(3)} \tag{2.14}$$

which neatly expresses the dependence of n_2 on the third-order nonlinearity.

In the context of single-mode fibres, the Kerr nonlinearity is often alternatively quantified

Method used	**λ (µm)**	**Measured n_2 (10^{-20} m^2/W)**	**Experimental conditions**
SPM	1.550	2.20	50-GHz modulation
XPM	1.550	2.63	7.4-MHz modulation
	1.548	2.73	10-MHz modulation
	1.548	2.23	2.3-GHz modulation

Table 2.1: Comparison of measured values of the Kerr coefficient n_2 near $\lambda = 1.55$ µm for a single-mode fibre. Values adapted from [7].

by the nonlinear parameter γ which is related to n_2 by [7]:

$$\gamma = \frac{\omega_0 n_2}{c A_{\text{eff}}}. \tag{2.15}$$

ω_0 is the centre frequency of an optical field or pulse. A_{eff} is the effective mode area of the fibre, itself defined as [7]:

$$A_{\text{eff}} = \frac{\left(\iint_{-\infty}^{\infty} |F(x,y)|^2 \, dx \, dy\right)^2}{\iint_{-\infty}^{\infty} |F(x,y)|^4 \, dx \, dy}, \tag{2.16}$$

where $F(x, y)$ describes the transverse electric field spatial distribution of the fundamental optical mode in the fibre. In practice, $F(x, y)$ is often approximated by a Gaussian function; therefore, we can instead use the mode field radius w which gives the $1/e^2$ intensity point, so that $A_{\text{eff}} = \pi w^2$ [7].

The value of n_2 in a given medium depends on the wavelength of the optical field and can vary by as much as 10% in fused silica. Methods used to measure n_2 in fibres typically involve using measuring a nonlinear effect such as SPM, XPM, or FWM to deduce the value of γ. Because of the variability in experimental optical pulse parameters and estimates of the value of A_{eff}, slightly different values can be obtained for the same wavelength. Table 2.1 provides some examples of measured values of n_2 for a standard single-mode fibre at around 1550 nm.

2.3.1 Self-phase modulation

The intensity dependence of the refractive index of a Kerr medium can result in the optical field gaining an additional *nonlinear phase* as it propagates. The first type of nonlinear phase we can consider arises from self-phase modulation (SPM), which is when an optical field with a time-varying intensity $I(T)$ gains a corresponding time-dependent phase. In general, this phase ϕ_{SPM} is given by [6]:

$$\phi_{\text{SPM}}(T) = -\frac{n_2 \omega_0 L}{c} I(T), \tag{2.17}$$

where L is the length of the Kerr medium, neglecting optical losses in the medium. For example, with Gaussian pulses of the form given by Eq. 2.3, the phase shift across the profile of the pulse is:

$$\phi_{\text{SPM}}(T) = -\frac{n_2 \omega_0 L}{c} I_0 \exp\left(-4 \ln 2 \frac{T^2}{T_{\text{FWHM}}^2}\right). \tag{2.18}$$

When one considers that the frequency of a wave describes the rate at which the phase evolves, the time-dependence of ϕ_{SPM} implies that the instantaneous frequency of the propagating pulse also evolves with time so that it varies from the central frequency ω_0 by an amount $\delta\omega(T) = \frac{d}{dT}\phi_{\text{SPM}}(T)$. As a result, an optical pulse can undergo significant spectral broadening for large variations in $\phi_{\text{SPM}}(T)$. In the context of telecommunications, SPM is normally unwanted or "parasitic" in that it can significantly increase the bandwidth of an optical pulse, especially for large values of propagation distance L and peak optical intensity I_0 [10]. Therefore, if a strong pump field is present in an optical fibre along with a weak signal field, the pump can potentially undergo significant spectral broadening due to SPM and spectrally overlap with the signal field. This can result in excess channel noise which cannot be spectrally filtered out.

2.3.2 Cross-phase modulation

Similarly, if two optical fields of different frequencies ω_1 and ω_2 are present in a Kerr medium, then the fields can impart an intensity-dependent phase shift onto each other in a process called cross-phase modulation (XPM) due to a nonlinear refractive index. Although both fields would gain a phase due to their own intensities via SPM, it can be shown that XPM is twice as effective in imparting phase for two fields of the same intensity [7].

We start by assuming that the optical field obeys the slowly-varying envelope approximation, but contains terms with two distinct frequencies ω_1 and ω_2, and two amplitudes $\mathcal{E}_1$ and $\mathcal{E}_2$. It is useful to describe the field in terms of complex exponentials:

$$E(t) = \frac{1}{2}\left(\mathcal{E}_1 e^{-i\omega_1 t} + \mathcal{E}_2 e^{-i\omega_2 t} + \mathcal{E}_1^* e^{i\omega_1 t} + \mathcal{E}_2^* e^{i\omega_2 t}\right) \tag{2.19}$$

Here, $\mathcal{E}_1$ and $\mathcal{E}_2$ are permitted to be complex (allowing for a relative phase difference between the two fields), and $\mathcal{E}_1^*$ and $\mathcal{E}_2^*$ denote the complex conjugates. To compute the third-order nonlinear polarization term $P^{(3)}(t) = \epsilon_0 \chi^{(3)} E(t)^3$, we can use the identity:

$$\begin{aligned}(a+b+c+d)^3 = a^3 + b^3 + c^3 + d^3 \\ + 3a^2b + 3a^2c + 3a^2d \\ + 3b^2a + 3b^2c + 3b^2d \\ + 3c^2a + 3c^2b + 3c^2d \\ + 6abc + 6acd + 6bcd + 6abd\end{aligned} \tag{2.20}$$

After expanding and gathering terms with like frequencies, we find that $P^{(3)}(t)$ can be

expressed as:

$$\begin{aligned} P^{(3)}(t) = \frac{1}{2}\big[&P^{(3)}(\omega_1)e^{-i\omega_1 t} + P^{(3)}(\omega_2)e^{-i\omega_2 t} + P^{(3)}(2\omega_1-\omega_2)e^{-i(2\omega_1-\omega_2)t} \\ &+P^{(3)}(2\omega_1+\omega_2)e^{-i(2\omega_1+\omega_2)t} + P^{(3)}(-\omega_1+2\omega_2)e^{-i(-\omega_1+2\omega_2)t} \\ &+P^{(3)}(\omega_1+2\omega_2)e^{-i(\omega_1+2\omega_2)t} + P^{(3)}(3\omega_1)e^{-i3\omega_1 t} + P^{(3)}(3\omega_2)e^{-i3\omega_2 t}\big] \\ &+ \text{c.c.} \end{aligned} \tag{2.21}$$

Where:

$$\begin{aligned} P^{(3)}(\omega_1) &= \frac{3}{4}\epsilon_0\chi^{(3)}\left(|\mathcal{E}_1|^2 + 2|\mathcal{E}_2|^2\right), & P^{(3)}(\omega_2) &= \frac{3}{4}\epsilon_0\chi^{(3)}\left(2|\mathcal{E}_1|^2 + |\mathcal{E}_2|^2\right), \\ P^{(3)}(2\omega_1-\omega_2) &= \frac{3}{4}\epsilon_0\chi^{(3)}\mathcal{E}_1^2\mathcal{E}_2^*, & P^{(3)}(2\omega_1+\omega_2) &= \frac{3}{4}\epsilon_0\chi^{(3)}\mathcal{E}_1^2\mathcal{E}_2, \\ P^{(3)}(-\omega_1+2\omega_2) &= \frac{3}{4}\epsilon_0\chi^{(3)}\mathcal{E}_1^*\mathcal{E}_2^2, & P^{(3)}(\omega_1+2\omega_2) &= \frac{3}{4}\epsilon_0\chi^{(3)}\mathcal{E}_1\mathcal{E}_2^2, \\ P^{(3)}(3\omega_1) &= \frac{1}{4}\epsilon_0\chi^{(3)}\mathcal{E}_1^3, & P^{(3)}(3\omega_2) &= \frac{1}{4}\epsilon_0\chi^{(3)}\mathcal{E}_2^3. \end{aligned} \tag{2.22}$$

The terms in Eq. 2.21 with frequencies other than ω_1 and ω_2 correspond to either THG or FWM. Both phenomena require phase-matching to become significant and can hence be neglected [7]. Up to third-order, the total induced polarizations $P_{\omega_1,\text{tot}}(t)$ and $P_{\omega_2,\text{tot}}(t)$ corresponding to ω_1 and ω_2, respectively, are then:

$$P_{\omega_1,\text{tot}}(t) = \epsilon_0\left[\chi^{(1)} + \frac{3}{4}\chi^{(3)}\left(|\mathcal{E}_1|^2 + 2|\mathcal{E}_2|^2\right)\right]\mathcal{E}\cos\omega_1 t \tag{2.23}$$

$$P_{\omega_2,\text{tot}}(t) = \epsilon_0\left[\chi^{(1)} + \frac{3}{4}\chi^{(3)}\left(2|\mathcal{E}_1|^2 + |\mathcal{E}_2|^2\right)\right]\mathcal{E}\cos\omega_2 t \tag{2.24}$$

We can see that both Eqs. 2.23 and 2.24 have terms corresponding to SPM and XPM. The factor of 2 shows that, given equal intensities in the two fields, the XPM contribution is twice as significant as SPM [7]. It follows that the phase gained by an optical pulse due to XPM would also be twice as large.

In the context of this work, we are concerned with the case where we use a strong pump

field and a weak signal field so that the signal has a minimal impact on the pump through either SPM or XPM. As presented in reference [2], in the case of two CW fields which are co-polarized (say, along the x-axis defined by the signal polarization) the phase imparted by the pump onto the signal due to XPM is given by:

$$\phi_{\mathrm{XPM,x}} = -\frac{2n_2\omega_s L}{c} I_p = -\frac{4\pi n_2 L}{\lambda_s} I_p \tag{2.25}$$

where I_p is the pump intensity, and ω_s and λ_s are the frequency and wavelength of the signal field, respectively. However, if the two fields are orthogonally polarized, then the added phase is instead [2]:

$$\phi_{\mathrm{XPM,y}} = -\frac{2n_2\omega_s L}{c} bI_p = -\frac{4\pi n_2 L}{\lambda_s} bI_p. \tag{2.26}$$

Here, b is a constant which reflects the tensor nature of $\chi^{(3)}$ and is equal to $\frac{1}{3}$ when the material is isotropic and the susceptibility is purely electronic in nature (i.e. the induced material polarization is due to the displacement of electrons only), as is the case in a single-mode fibre [6, 7].

2.4 Optical Kerr switching

The central idea behind the optical Kerr switch is to utilize XPM in order to create an effective birefringence in a Kerr medium [2]. This birefringence, induced by a strong pump pulse, is used to rotate the polarization of the signal between two orthogonal "switched" and "unswitched" states as depicted in Fig. 2.1.

Our switch is comprised of a single-mode fibre (SMF) which acts as our Kerr medium. A linearly-polarized signal field is combined with a linearly-polarized pump field using a beamsplitter, and coupled into the SMF. If the polarizations of the signal and pump fields are offset by an angle of $\theta = 45°$, then the pump will induce an effective birefringence in the medium as the signal will experience a different phase shift along the two orthogonal

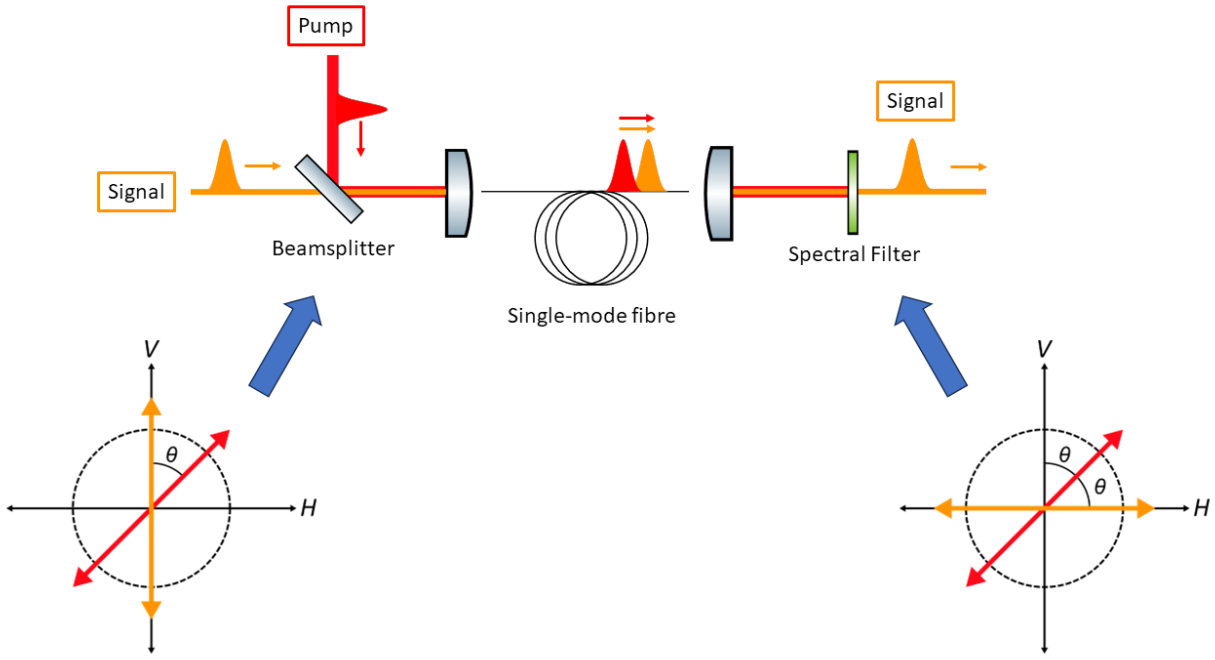

Figure 2.1: Basic operation of an optical Kerr switch, where a single-mode fibre is used as the Kerr medium. Pulse trains corresponding to a strong pump (red) and weak signal (orange) are combined with a beamsplitter and coupled into the fibre, with the polarization of the pump field offset from that of the signal by an angle $\theta = 45°$. As a result of XPM-induced birefringence in the fibre, the signal polarization is "switched" and rotated by an angle $2\theta = 90°$, while the pump is spectrally filtered out. The diagrams on the lower left and right indicate the pump (red) and signal (orange) polarizations before and after the fibre, respectively.

polarization axes. As shown in [2], this difference in phase shift $\Delta\phi$ is found by subtracting Eqs. 2.25 and 2.26. For a CW pump field and $b = \frac{1}{3}$, we have:

$$\Delta\phi = \phi_{\mathrm{XPM,xy}} - \phi_{\mathrm{XPM,xx}} = \frac{8\pi n_2 L}{3\lambda_s} I_p. \tag{2.27}$$

In order for the switch to convert a signal between two linear polarization states, the birefringence must satisfy the relation $\Delta\phi = \pi$. In other words, the signal must behave as though it has passed through a half-wave plate (HWP) when the pump is present. Once the signal has been rotated, the pump can be spectrally filtered out.

However, in our case, we are instead using a pump pulse train whose repetition rate

is synchronized with our signal pulse train. This is crucial because in order to work as a temporal filter, the switch must only act on photons whose arrival at the switch coincides with the arrival of the pump pulses. If the pump was CW, then it would simply switch all the incoming light without discriminating between noise photons (which arrive at random times) and signal photons (which arrive with a fixed repetition rate).

For a pulsed pump and signal, full polarization switching can be achieved by ensuring that the signal and pump fields have mismatching group velocities v_{gs} and v_{gp}, respectively, in the Kerr medium. Due to the resulting walk-off, the signal and pump pulses will pass through each other over the length of the fibre. The pump pulse thereby "samples" each part of the signal pulse to ensure that the signal picks up the birefringent phase $\Delta\phi$ over its entire temporal profile.

In the reference frame of the signal pulse, this phase is taken by integrating the intensity profile of the pump $I_p(t)$ over the length of the fibre L at each time during which the pump and signal pulses overlap. As given in references [1] and [2], this can be expressed as:

$$\Delta\phi(T) = \frac{8\pi n_2}{3\lambda_s} \int_0^L I_p(T - d_w z)\, dz, \tag{2.28}$$

where $d_w = v_{gp} - v_{gs}$ is the walk-off parameter between the pump and signal. Here, the time T in the frame of the signal pulse also corresponds to a temporal delay between the signal and pump. Because of the finite temporal width of the pump pulses, $\Delta\phi(T)$ is equal to zero when the pump and signal do not overlap. As suggested by the above equation, the key parameters we can manipulate in a Kerr switch are the signal and pump wavelengths, pump intensity, walk-off, and fibre length. Note that this equation assumes that the temporal profile of the pump does not change over the length of the fibre.

Using $\Delta\phi(T)$, we can define a switching efficiency $\eta(T)$ which quantifies the fraction of the signal pulse power that is converted between two orthogonal polarizations, given a

signal-pump delay T. This is given by [1–3]

$$\eta(T) = \sin^2(2\theta)\sin^2\left(\frac{\Delta\phi(T)}{2}\right), \tag{2.29}$$

where θ is the difference between the initial signal and pump polarizations. Clearly, the switching efficiency η can range from 0 to 1, and is maximum when $\theta = 45°$ and $\Delta\phi = \pi$, which is indeed similar to the action of a HWP.

In the limit of a signal pulse that is a delta function in time, the experimentally-measured switching efficiency vs signal-pump delay would be fully represented by Eq. 2.29. However, because a real signal pulse has a finite temporal width, the quantity measured in the lab would instead be represented by the cross-correlation, or sliding inner-product, of the switching efficiency and the signal intensity profile. Thus, the quantity measured in the lab is the switching efficiency for the complete pulse, which is instead represented by

$$\eta_{\text{pulse}}(T) = \int_{\infty}^{\infty} \eta(t)\bar{I}_s(t+T)\,dt \tag{2.30}$$

where $\bar{I}_s$ the signal intensity profile, normalized to a peak value of 1. To avoid ambiguity, $\eta_(T)$ is hereafter referred to as the "*instantaneous*" switching efficiency, and $\eta_{\text{pulse}}(T)$ is referred to as the "*pulse*" switching efficiency.

It is therefore necessary for $\eta(T)$ to have a flat-top profile and maintain a value of 1 for the full duration of the signal pulse, so that the entire pulse gets switched. The duration of the flat top can be increased or decreased by lengthening or shortening the fibre, respectively. Ideally, the fibre length should be kept to a minimum to ensure optimal temporal filtering since any excess length will needlessly widen the filter window.

To use the Kerr switch as a filter in quantum communication, it is placed after Bob's polarization projection stage so that both signal and noise are linearly co-polarized as they are coupled into the fibre. After the pump is spectrally removed after the fibre, the signal and noise pass through a crossed polarizer which is aligned orthogonally to the initial signal

polarization. If the switch achieves maximum switching efficiency, then both signal and noise photons should only pass through the polarizer and ultimately get detected if they have been switched in the presence of the pump. While the signal and pump pulses should coincide in the fibre consistently, noise photons will arrive randomly and are far less likely to coincide with the pump and be switched, resulting in a much smaller noise count compared to the case without the switch.

2.5 Parasitic nonlinear effects

Although we exploit nonlinear optics to our benefit, care must be taken to avoid parasitic nonlinear effects which can generate excess noise [2]. After all, a noise filter must reduce noise, not increase it. In our case, we are mainly concerned with nonlinear effects which can broaden our pump spectrum and generate noise that cannot be spectrally filtered out. Two particular effects which can contribute to such noise via spectral broadening include SPM (as discussed earlier) and stimulated Raman scattering (SRS). SRS occurs when energy from the pump partially transfers into the vibrational modes of a medium, generating a frequency-downshifted Stokes wave [6, 7]. In silica fibres, this process has a broad gain spectrum which extends over approximately 40 THz and peaks near 13 THz (as depicted in Fig. 2.2).

To avoid issues due to nonlinear spectral broadening, the pump wavelength should be chosen to be far enough away from the signal wavelength so that it can be filtered out even if the pump spectrum broadens considerably. Stimulated Raman scattering imposes an additional restriction in that the λ_p should be *longer* than λ_s, so that the downshifted Stokes field does not spectrally overlap with the signal.

2.6 Simple model of switching response

We numerically evaluate the integral given by Eq. 2.28 in order to predict the switching response $\eta(T)$ (given by Eq. 2.29) for a given set of experimental parameters (such as signal

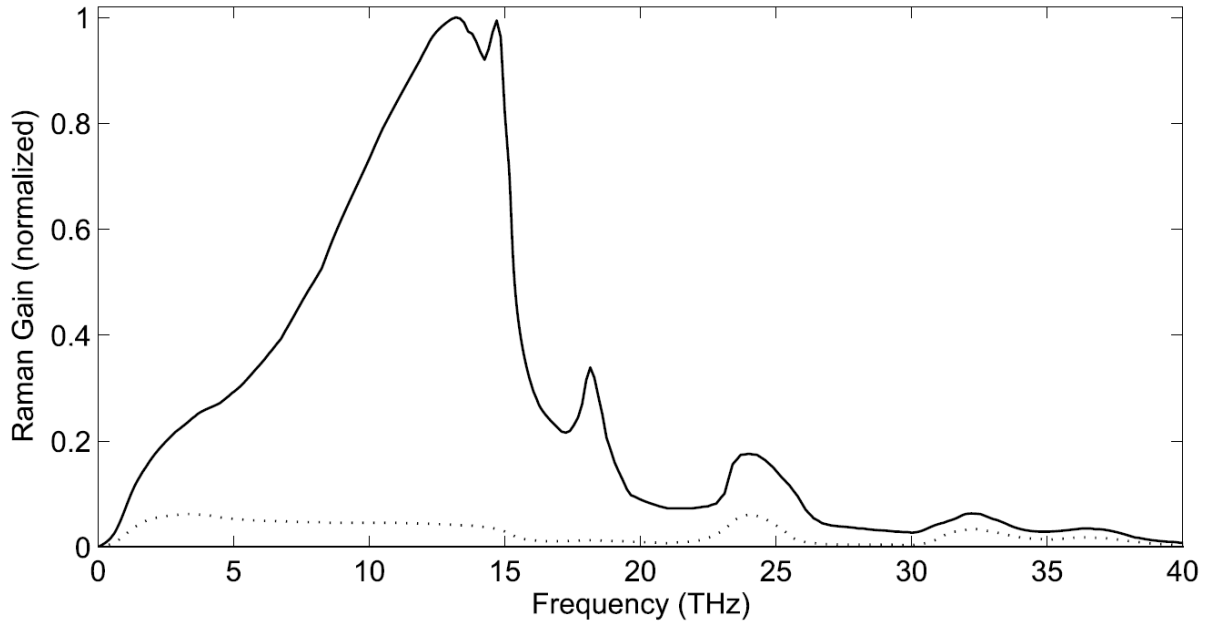

Figure 2.2: Normalized Raman gain for fused silica when pump and Stokes waves are co-polarized (solid curve). The dotted curve shows the situation in which the pump and Stokes waves are orthogonally polarized. This figure is reproduced from reference [7] with the permission of Elsevier Science & Technology Journals; permission was conveyed through Copyright Clearance Center, Inc.

and pump wavelengths, Kerr medium dispersion and length, and pump power). For our simple numerical model, which is adapted from a MATLAB script provided by the authors of reference [1], we assume that our pump pulses have a Gaussian shape given by Eq. 2.3 with a temporal FWHM of 150 fs and neglect any evolution in the temporal and spectral profile of the pump due to dispersion or nonlinear processes. The inclusion of these effects in a numerical Kerr switch model is later explored in Chapter 4.

For a given pair of signal and pump wavelengths λ_s and λ_p, we estimate the walk-off parameter d_w from the dispersion parameter $D_{\text{fibre}}(\lambda) = \frac{d}{d\lambda}(1/v_g)$ of the single-mode fibre used as the Kerr medium. For Corning SMF-28 Ultra (a standard telecom fibre), $D_{\text{fibre}}(\lambda)$ is modeled using a Sellmeier-type equation of the form [27]:

$$D_{\text{fibre}}(\lambda) = \frac{s_0}{4}\left[\lambda - \frac{\lambda_{\text{ZDW}}^4}{\lambda^3}\right] \tag{2.31}$$

where λ_{ZDW} is the zero-dispersion wavelength and S_0 is the zero dispersion slope; for SMF-28 Ultra, these values are 1317 nm and 0.088 ps/(nm^{2}km), respectively [28]. d_w is then obtained by integrating $D_{\mathrm{fibre}}(\lambda)$ between the signal and pump wavelengths:

$$d_w = \frac{1}{v_{gp}} - \frac{1}{v_{gs}} = \int_{\lambda_s}^{\lambda_p} D_{\mathrm{fibre}}(\lambda)\, d\lambda. \tag{2.32}$$

We implement the numerical model in MATLAB to evaluate $\eta(T)$ for a 1-metre length of single-mode fibre (this being the shortest length of fibre readily available to us). Fig. 2.3 depicts the results for a C-band signal wavelength of 1550 nm and a pump wavelength of 1650 nm; and Fig. 2.4 depicts the results for a O-band signal wavelength of 1300 nm and a pump wavelength of 1550 nm. We find that for both wavelength configurations, the switching efficiency is predicted to reach unity at a pump power of around 4 nJ/pulse and provide a temporal filter width of around 2 ps.

It should be noted that the approximation given by Eq. 2.31 is nominally considered valid for wavelengths between 1200 nm and 1600 nm. However, because the C-band signal wavelength of 1550 nm is close to the upper limit, the corresponding pump wavelength was chosen fall slightly outside of this range in order to ensure that it can be spectrally filtered from the signal and that there is a large enough walk-off between pulses. We therefore assume that Eq. 2.31 is still reasonably accurate at a wavelength of 1650 nm in our model. Moreover, the instantaneous switching efficiency curve simulated in this simple model does not account for the signal intensity profile per Eq. 2.30, and thus does not fully represent the quantity to be measured experimentally. Rather, the purpose of this model is to inform on potential wavelengths and optical powers that could be used for the pump field.

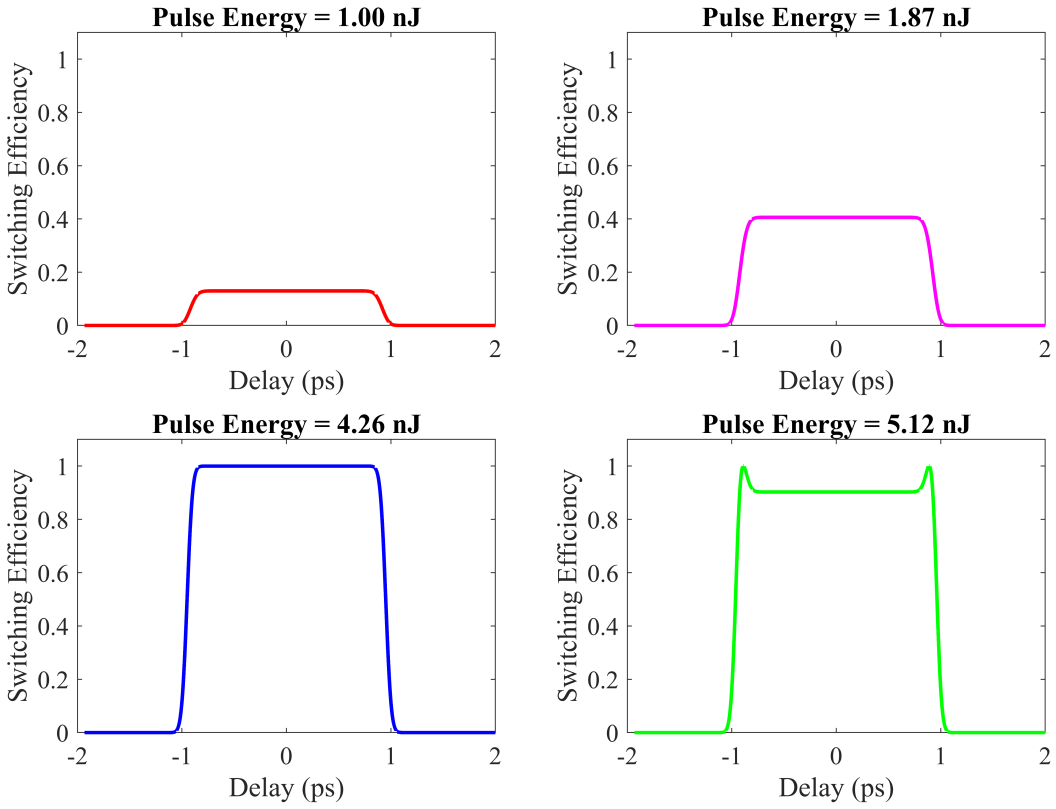

(a)

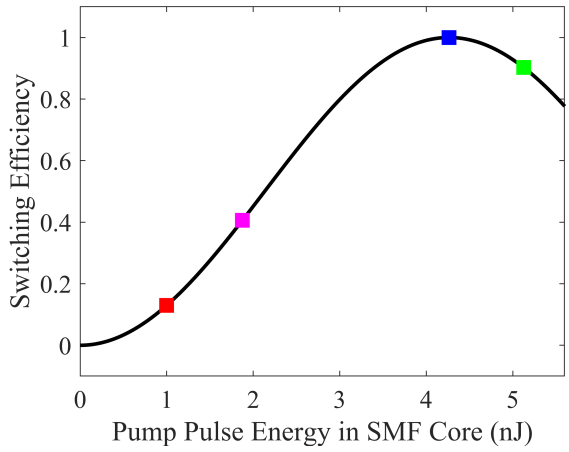

(b)

Figure 2.3: Simulated Kerr switching response for a 1550 nm signal and 1650 nm pump. This model neglects any evolution in the spectral and temporal profile of the pump and assumes a pump pulse of width $T_{\mathrm{FWHM}} = 150$ fs. (a) Instantaneous switching efficiency vs. delay for varying values of pump pulse energy. (b) Instantaneous switching efficiency at time zero vs. pump pulse energy. A switching efficiency of unity is achieved for pump pulses with energy $U_{\mathrm{pump}} = 4.26$ nJ.

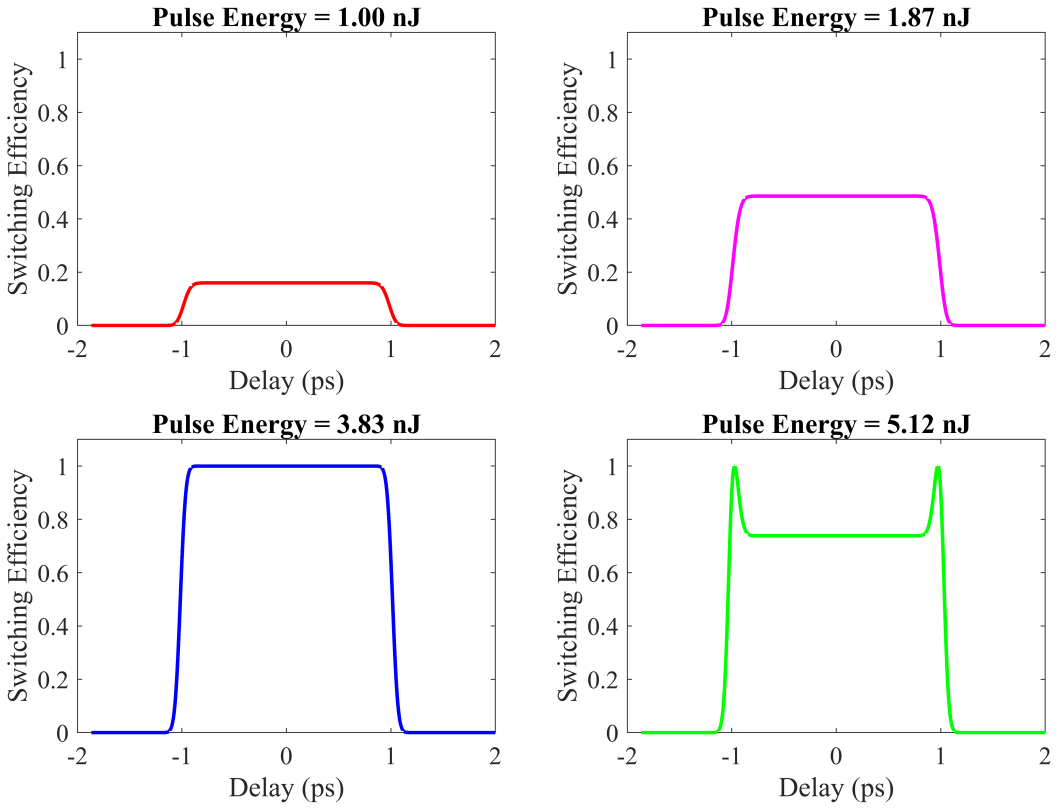

(a)

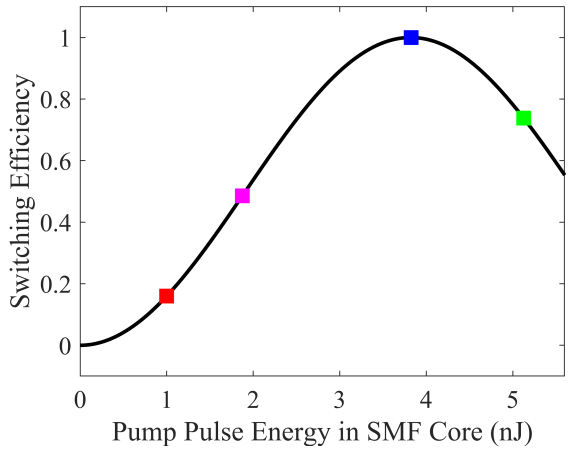

(b)

Figure 2.4: Simulated Kerr switching response for a 1300 nm signal and 1550 nm pump. This model neglects any evolution in the spectral and temporal profile of the pump and assumes a pump pulse of width $T_{\mathrm{FWHM}} = 150$ fs. (a) Instantaneous switching efficiency vs. delay for varying values of pump pulse energy. (b) Instantaneous switching efficiency at time zero vs. pump pulse energy. A switching efficiency of unity is achieved for pump pulses with energy $U_{\mathrm{pump}} = 3.83$ nJ.

Chapter 3

Preliminary experiments

3.1 Summary

Having reviewed the relevant theory to understand the basic operation of a Kerr switch, in this chapter we now turn our attention towards implementing an experimental setup to perform telecom-wavelength single photon switching. We begin by providing a detailed overview of the experimental setup we constructed, including key equipment specifications. We will then explain our procedure for measuring the polarization switching response, and provide preliminary experimental results. Finally, we describe obstacles that arose during these initial Kerr switching experiments to motivate the numerical work discussed in Chapter 4. Further experimental results are later provided in Chapter 5.

3.2 Experimental design

The experimental design described in this section is largely influenced by the arrangement used in reference [1], although the setup we built has several differences to implement switching of telecom-wavelength signal photons and to account for differences in equipment.

The overall experimental setup is depicted in Fig. 3.1. To synchronously generate the signal and pump fields we use in our Kerr switch, we use a mode-locked femtosecond (fs)

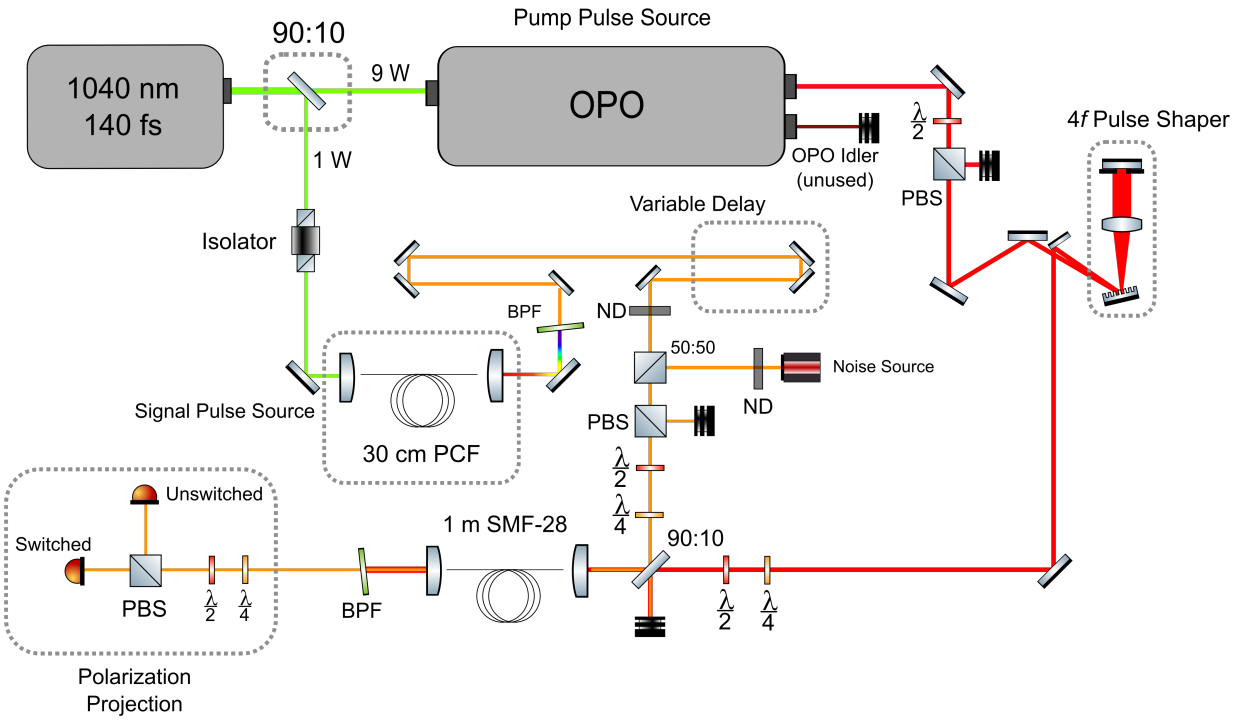

Figure 3.1: Experimental setup schematic. OPO: optical parametric oscillator; PBS: polarizing beamsplitter; $\frac{\lambda}{4}$: quarter-wave plate; $\frac{\lambda}{2}$: half-wave plate; PCF: photonic crystal fibre; BPF: bandpass filter; ND: neutral density filter.

fibre laser (Coherent Fidelity HP) which produces ultrafast 1040 nm pulses with a temporal FWHM of 140 fs. This laser produces an average output power of 10 W with a repetition rate of 80 MHz, or 125 nJ per pulse. Although the wavelength and power are not directly user-tunable, the laser provides limited control over the chirp of the pulses by adjusting the group delay dispersion (GDD) in software. The light from the fs laser is then split by a 90:10 beamsplitter; up to 1 W of light passes through an optical isolator (in order to prevent any back-reflected light from coupling back into the laser) and is then coupled into a length of photonic crystal fibre (PCF) to generate our signal pulses. The remaining 9 W is sent into an optical parametric oscillator (OPO) (Coherent Levante IR fs) to produce the pump pulses for our switch. The OPO in turn produces two output fields with a typical pulse FWHM of 150 fs: one with a shorter wavelength known as the "signal" (not to be confused with the signal field in the context of Kerr switching) and one with a longer wavelength known

as the "idler." The wavelengths of the two OPO output fields can be tuned over the ranges of 1320 nm to 2000 nm and 2170 nm to 5000 nm, respectively, which allows us to use the shorter-wavelength field as a versatile pump field in our Kerr switch. The signal and pump fields are coupled together into a 1-m length of SMF-28 Ultra fibre (Thorlabs P1-SMF28Y-FC-1) which acts as the Kerr medium for the switch; this fibre is hereafter referred to as the "switching fibre." Finally, the pump field is spectrally filtered out and the final polarization of the signal field is measured.

3.2.1 Signal pulse generation

In order to assess the performance of the Kerr switch for quantum communication at different telecom bands, it is important to have the ability to select from a variety of signal wavelengths. We implement a cost-effective signal source with a "tunable" wavelength by using supercontinuum generation (SCG) in a 30-cm length of PCF, which was custom-manufactured by Photonics Bretagne. The PCF has a cladding diametre of 134 µm and is designed with a microstructure consisting of multiple rings of air holes which confines the coupled light into a small core diameter of 4.50 µm. This structure enhances the nonlinearity of the fibre and promotes SCG, which results in a considerably broadened pulse spectrum as a result of various simultaneous nonlinear effects such as SPM, FWM, and SRS [7].

Two 30-cm samples of PCF were initially cleaved from the quantity ordered from Photonics Bretagne. Because the holes in the microstructure of the PCF sample are exposed to air after cleaving, it was important that the ends of the fibre were protected in order to avoid contamination due to dust which could potentially burn due to the high intensity of the 1040 nm pulses. Moreover, in order to promote coupling of light into and out of the PCF, a transitioning medium (such as another piece of conventional optical fibre or fused silica) should be spliced onto each end of the PCF to allow the mode size to gradually increase between the PCF core and free space. On one 30 cm PCF sample, 50 cm lengths of HI Flexcore 1060 fibre were spliced onto both ends. On the other sample, both tips were

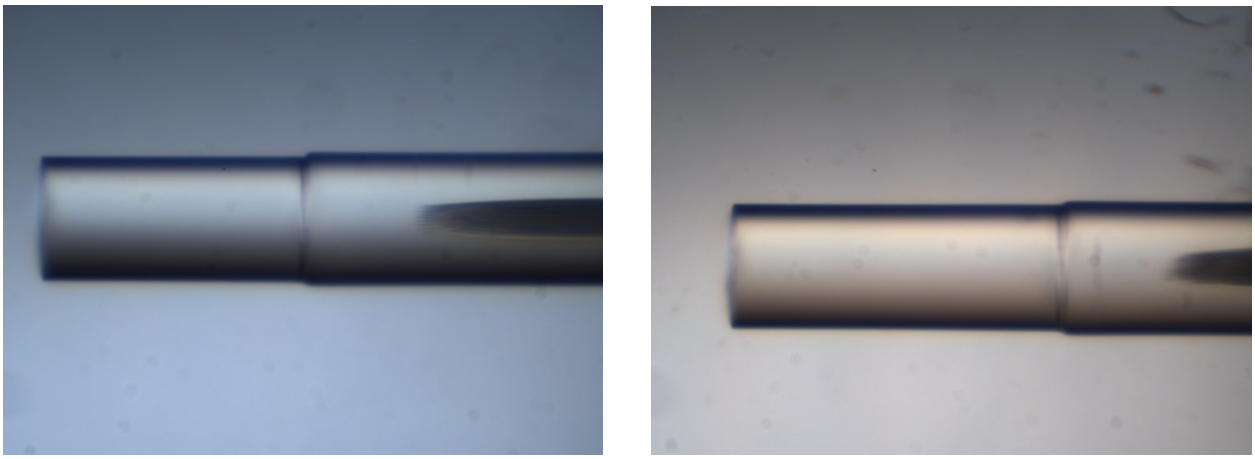

(a) (b)

Figure 3.2: Pure silica end caps of length (a) 280 µm and (b) 340 µm spliced onto the 30 cm length of photonic crystal fibre (PCF). Photos courtesy of H. Ding, National Research Council of Canada.

first heated in order to collapse the holes over a length of approximately 125 µm. End caps consisting of 280 µm and 340 µm lengths of pure silica rods were then spliced onto the ends of the PCF, as depicted in Fig. 3.2. These silica rods were custom-produced by Polymicro Technologies and have a core diametre of 126.7 µm to approximately match the cladding diametre of the PCF. This second sample was ultimately implemented in our SCG source; the other sample has not been tested due to the fragility of the PCF and potential hazards of attempting to switch out the PCF sample in the setup.

The PCF is mounted between two translation stages, with aspheric lenses of focal length 3.1 mm positioned at both ends to couple light from the fs laser into and out of the fibre. To determine the optimum beam waist for coupling the 1040 nm pulses, a monochromatic camera (The Imaging Source DMK 37BUX178) was used to compare the beam waist at the input and output of the PCF. A two-lens Galilean telescope was positioned before the PCF to match the input beam waist to the output beam waist of approximately 0.5 mm. The resulting output spectrum is measured using a near-infrared (NIR) spectrometer (OceanInsight NIRQuest512-2.5) with a wavelength measurement range of 900 nm to 2500 nm and a resolution of approximately 3.3 nm. As depicted in Fig. 3.3, the spectrum of the input

1040 nm pulses broadens by several hundreds of nm. The supercontinuum pulses then pass through a spectral bandpass filter chosen to match our desired signal pulse wavelength and spectral width. To generate C-band signal pulses, we use a 1550 nm bandpass filter with a 25 nm FWHM spectral width (Edmund Optics stock no. 87-834).

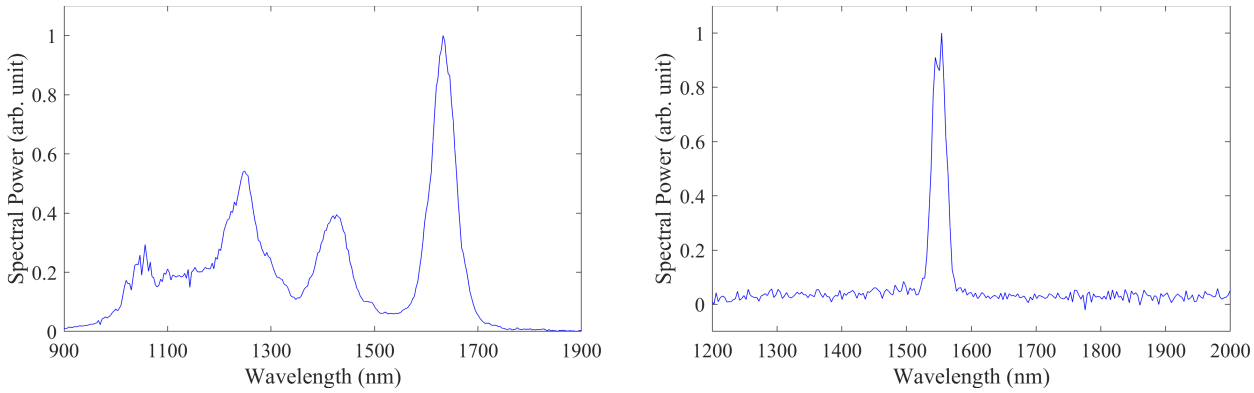

Figure 3.3: Spectrum for photonic crystal fibre (PCF) signal source. The 30 cm length of PCF is pumped to produce (a) a supercontinuum spectrum which is passed through a bandpass filter from which (b) a 1550 nm signal is obtained.

Typically 0.8 W of 1040 nm light is coupled into the PCF with an efficiency of approximately 70%; however, this coupling was often frequently adjusted due to drift in the output power attributed to instability in the PCF mounting setup. To limit airflow-related instability in the PCF setup, an acrylic box was constructed around the PCF with holes at the front and back to allow optical access.

The spectrally-filtered signal pulse is then directed onto a retroreflector mounted on a motorized translation stage (Thorlabs MTS50-Z8) which acts as a delay line in order to vary the time of arrival of the signal pulses at the Kerr medium. This stage has a 50 mm travel range and minimum step size of 0.05 µm, and is operated using a DC servo motor controller (Thorlabs KDC101).

Following the delay line, the signal is then attenuated using variable neutral density (ND) filters and linearly polarized using a PBS.

3.2.2 Pump pulse generation

This section describes how the OPO is used as a versatile pump field source for the Kerr switch setup. Using software, the higher-frequency field from the OPO can be set between 1320 nm and 2000 nm, producing pulses of approximately 150 ps duration. A polarizing beamsplitter (PBS) and half-wave plate (HWP) mounted in a motorized rotation stage (Thorlabs K10 CR1) are used to vary the amount of pump power being used in the switch. This rotation stage has a stepper motor and a minimum angular step size of 0.03°. After this power control stage, the pump field is directed into a folded $4f$ pulse shaper which allows us to tune the spectral and temporal profile of the pump pulses.

The $4f$ pulse shaper uses a blazed reflective diffraction grating (Thorlabs GR25-0616) in order to spatially separate the frequency components of the pulse according to:

$$d\left[\sin\theta_i + \sin\theta_d\right] = m\lambda \tag{3.1}$$

where d is the grating spacing, θ_i and θ_d are the angles of incidence and diffraction of the field (relative to the surface normal of the grating), λ is the wavelength of a single frequency component, and m is the order of diffraction. The grating used in our setup has a grating density of $1/d = 600$ lines/mm, with a blaze angle optimized for a wavelength of 1.6 µm. A plano-convex lens with focal length $f = 15$ cm is placed $1f$ away from the grating to collect the $m = 1$ diffraction order. In the Fourier plane of the lens (a distance of $2f = 30$ cm from the grating), each spectral component with frequency ω_k of a Gaussian pulse is located at a position

$$X_k = \alpha\omega_k, \tag{3.2}$$

where

$$\alpha = \frac{{\lambda_0}^2 f}{2\pi c d\cos\theta_d}. \tag{3.3}$$

Each spectral component has a finite spatial width of

$$\Delta x_0 = \sqrt{2\ln 2} \cdot \frac{\cos\theta_i}{\cos\theta_d} \frac{f\lambda_0}{\pi w_{\text{in}}}, \tag{3.4}$$

where w_{in} is the beam waist of the pulse incident on the grating. A mirror is placed at the Fourier plane to redirect the pulses back through the lens and onto the grating, where the spectral components are recombined.

A slit with a variable width is placed in front of the mirror to act as a mask, allowing us to tune the spectral width (and hence temporal profile) of the pulse by physically blocking parts of the spectrum, effectively acting as a "flat-top" spectral filter.

Although this feature would not be explored until after the work discussed in Chapter 4, the folded $4f$ pulse shaper also allows us to tune the chirp of the pump pulses, which will later prove crucial to compensating for the dispersion characteristics of our switching fibre. Consider a small variation δf in the lens-mirror distance (relative to the focal length f), and a small variation Δf in the mirror-grating distance (relative to $2f$). As shown in [29], the GDD imparted on the pulse is then given by

$$\text{GDD} = -\frac{\lambda_0}{\pi c^2 f^2}[(\delta f + \Delta f)(f^2 + \delta f(\delta f + \Delta f)(\cot(90^\circ - \theta_d) - \cos(90^\circ - \theta_i)\csc(90^\circ - \theta_d)], \tag{3.5}$$

where the positive direction is defined as pointing from the grating to the mirror.

Eq. 3.5 tells us that if the lens-mirror distance is kept fixed at f (so that $\delta f = 0$), then a positive chirp is applied by moving the mirror and lens closer to the grating, and a negative chirp is applied by moving the mirror and lens away from the grating.

3.2.3 Kerr switch setup and signal detection

Having generated our signal and pump pulses, we simultaneously couple them into the 1-m length of SMF-28 used as our Kerr medium. This switching fibre is mounted between two

translation stages in a similar fashion as the PCF, and is pulled taut in order to minimize bend/stress-induced polarization effects in the fibre.

A quarter-wave plate (QWP) and half-wave plate is placed in the paths of both the signal and pump fields in order to set their initial polarizations. The signal and pump beams are then combined using a non-polarizing beamsplitter (Thorlabs BSN12) which nominally has a reflectance:transmission (R:T) ratio of 10:90 for unpolarized light. In practice, the (R:T) ratio is different for s- and p-polarized light incident at 45° relative to the surface normal (e.g. approximately 15:85 and 2:98, respectively, at a wavelength of 1550 nm). Aspheres of focal length 18.40 mm are used to couple the signal and pump fields into and out of the fibre. Coupling efficiencies of the signal and pump into this fibre are typically around 75%.

Cascaded spectral bandpass filters (Thorlabs FB1550-40 × 1 and FBH1550-40 × 2) are placed at the output of the SMF to eliminate the pump light. These filters are centred at 1550 nm with a FWHM of 40 nm, and collectively provide a nominal 135 dB of attenuation outside their pass band. The remaining signal field then passes through a QWP and HWP which are used to compensate for any polarization evolution due to birefringence intrinsic to the fibre itself. A PBS is positioned after these waveplates to project the signal onto horizontal (H) and vertical (V) polarizations.

Each output port of the PBS is coupled into 10-metre lengths of SMF-28 which each lead to a superconducting nanowire single-photon detector (SNSPD) contained in a Quantum Opus One unit. These SNSPDs are rated with detection efficiencies of >80% at O- and C-band telecom wavelengths, and have a recovery time of 50 ns which corresponds to a maximum count rate of approximately 2×10^7 s^{-1}, or 0.25 photons per signal pulse. Upon absorbing a photon, the nanowires transition between a superconducting and non-superconducting state, generating an electronic signal which is detected by a time-to-digital converter (TDC) (Swabian Instruments Time Tagger 20) used to measure photon count rates in two channels corresponding to H and V polarizations. An additional QWP and HWP are placed after each output port of the projection stage PBS to optimize the detection efficiency

of the SNSPDs, which depends on the polarization of the impinging photons. The 10-metre fibres are shielded with a stainless steel jacket to minimize detection of ambient light from the surroundings; the coupling efficiency of the signal into these fibres is approximately 75%.

The various optical components in the setup (fibres, beamsplitters, mirrors, lenses, wave-plates, etc.) contribute to some loss in the signal. However, the dominant sources of loss that we consider are the 75% coupling efficiencies into the various SMFs. Combined with the >80% detection efficiencies of the SNSPDs, we estimate that the total loss between the number of signal photons entering the switching fibre and the number of signal counts measured by the TDC is 3 dB.

3.2.4 Initial calibration of setup

In order to achieve maximum Kerr switching in accordance with Eq. 2.29, it is critical to optimize the initial polarizations of the signal and pump fields and establish the optimal signal-pump delay so that the two pulses fully walk through each other in the switching fibre. The signal field polarization is first set by adjusting the QWP and HWP before the switching fibre to send in H-polarized light; we then adjust the birefringence-compensating QWP and HWP after the switching fibre to cancel out any polarization evolution in the fibre (in the absence of the pump) which is determined by maximizing H-polarized photon counts and minimizing V-polarized counts at the SNSPDs. The positions of the compensating QWP and HWP are confirmed by repeating this process for an initially V-polarized signal.

Next, we determine the optimal pump polarization and signal delay. The pump field is turned on and the QWP and HWP are adjusted so that the input polarization is approximately 45° relative to the signal polarization. The pump power is increased to approximately 4 nJ/pulse, which should generate near-unity switching. Then, the stage position of the retroreflector in the signal path is adjusted until counts are observed in the "switched" polarization channel. The stage position is scanned in order to measure the full temporal profile of the switching curve; the centre of this curve corresponds to time zero. The pump

polarization is optimized by adjusting the QWP and HWP until the switched counts are maximized at a fixed pump power.

In order to properly measure the Kerr switching efficiency, the overall total detection efficiencies at the SNSPDs (taking into account the coupling efficiencies of the various fibres) must be balanced as closely as possible so that the total counts across both polarization channels reflects the total number of initial signal counts as the delay is scanned. This is determined by rotating the HWP after the switching fibre with the signal on and pump off, and verifying that the signal counts reported by the two SNSPD channels increase and decrease in accordance with Malus's law. The coupling of the signal into the shielded SNSPDs is adjusted until the peak count rate, measured as the HWP is rotated, is equal in both channels.

3.3 Data collection and processing

We evaluate the performance of the Kerr switch at a fixed pump power by measuring the pulse switching efficiency of the signal versus the pump-signal delay. The switching efficiency is determined by measuring the count rates in both SNSPD channels as the delay stage is scanned through a series of positions about the time-zero position. At each position, the total counts from the Time Tagger are measured over a period of 10 ms while the stage is stationary; the counts are divided by this interval to calculate the count rate in each channel. The switching efficiency at each position is then defined as:

$$\eta_{\text{pulse}} = \frac{\text{Count rate in "switched" channel}}{\text{Total count rate in both channels}} \tag{3.6}$$

where "switched" channel refers to the SNSPD measuring the counts for the polarization the signal is rotated onto when the switch is active (i.e. if the signal is initially H-polarized, then the switched channel measures V-polarized counts and vice versa). Because the optical power of the signal tends to drift over time due to instability in the PCF, the switching

efficiency is calculated for each delay stage position and is normalized to the total count rate measured at that position, rather than being normalized to the total count rate at the beginning of the scan. The switching efficiency at time zero is then plotted against pump power in order to determine the optimum pump power for maximum switching efficiency (ideally unity), and the switching curve at that optimal pump power is used to determine the temporal width of the switch.

The pump itself is characterized by estimating the power coupled into the switching fibre, and measuring the spectral profile after the fibre to monitor any nonlinear evolution in the pump. To expedite power measurements, the pump power is monitored by using an AR-coated beam sampler (Thorlabs BSF10-C), positioned immediately before the switching fibre, to reflect a fixed fraction of the total pump power with an R:T ratio of 0.0357:1. The beam is reflected at near-normal incidence in order to avoid any polarization-dependent variance in the reflectance and transmittance. The power of this reflected beam is then measured using a photodiode power sensor (Thorlabs S122C), and the total pump power coupled into the fibre is estimated based on the R:T ratio and the measured coupling efficiency into the fibre. After the fibre, a motorized mirror mount (Thorlabs MFF101) is used to pick off the pump in order to measure the spectral profile using a spectrometer (Ocean Optics NIRQuest) equipped with an integrating sphere.

To accurately calculate the switching efficiency and assess the viability of the Kerr switch as a temporal filter, our data processing requires us to account for noise which accompanies the signal being measured by the SNSPDs. This noise consists of leakthrough from the pump which passes through the spectral filters, ambient light from the laboratory environment, and dark counts inherent to the SNSPDs. We evaluate this noise by taking the average and standard deviation over 50 measurements of the count rate in each SNSPD channel, with the signal blocked. Because we wish to use the Kerr switch as a filter, the noise present in the switched channel is referred to as the "intrinsic" noise of the Kerr switch. The average noise count in each channel is then subtracted as a constant background from the measured

switched/unswitched counts before calculating the switching efficiency.

To avoid saturating the SNSPDs, the signal is attenuated using ND filters until approximately 0.1 counts/pulse are measured. As a safety consideration, the switching efficiency and noise measurements are first taken with ND filters positioned *after* the switching fibre in order to attenuate both the signal and pump in case that nonlinear broadening of the pump generates a significant amount of light within the pass band of the spectral filters. This configuration is hereafter referred to "back-attenuation." If the back-attenuated pump does not appear to generate appreciable leakthrough noise, then the measurements are repeated with the ND filters relocated into the signal path before the 90:10 beamsplitter, in order to attenuate only the signal; this configuration is referred to as "front-attenuation."

3.4 Preliminary results for C-band signal switching

Following the procedure described above, we demonstrate Kerr switching of C-band single photons given the following parameters: $\lambda_s = 1550$ nm, $\Delta\lambda_s = 25$ nm, $\lambda_p = 1650$ nm, $\Delta\lambda_p = 23.6$ nm. Here, $\Delta\lambda_s$ and $\Delta\lambda_p$ are the spectral FWHM of the signal and pump, respectively. Using the $4f$ pulse shaper, $\Delta\lambda_p$ is decreased to 23.6 nm from the initial 32.2 nm spectral width of the 1650 nm pulses generated by the OPO. This results in reduced nonlinear spectral broadening after the switching fibre, as shown in Fig. 3.4. The results in this section are obtained with the ND filters positioned for back-attenuation.

The switching efficiency and intrinsic noise vs pump power are depicted in Fig. 3.5. Although the maximum switching efficiency increases with pump power, it appears to saturate at a value of approximately 96% starting at 6.5 nJ/pulse, rather than following the expected $\sin^2$ dependence. The switching curve at 6.5 nJ/pulse has a temporal FWHM of 2.0 ps, which is consistent with the predicted width based on the simple model discussed in Section 2.6. However, the shape of the switching curve is quite asymmetric and the pump power required for near-unity switching is much larger than what was estimated by the model;

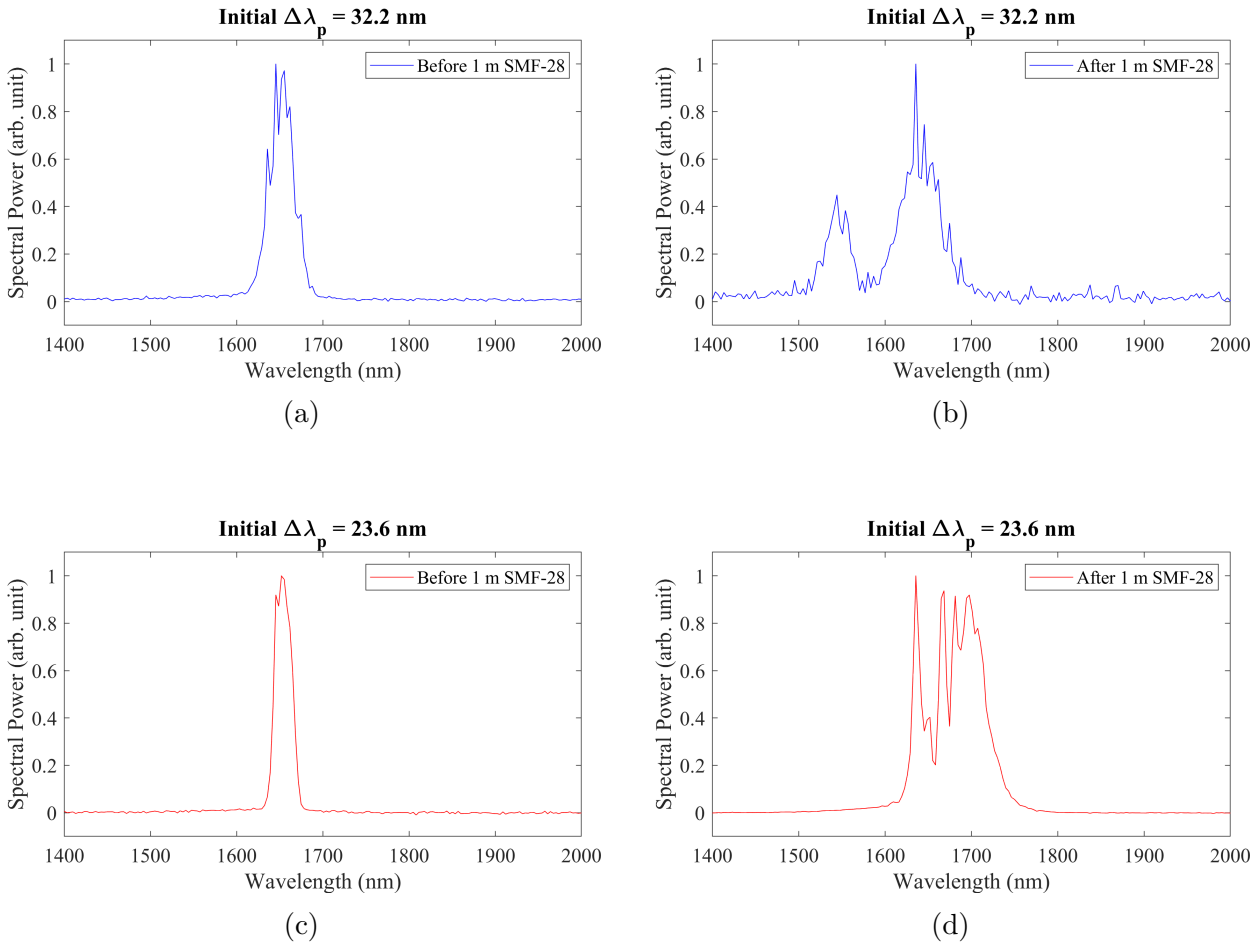

Figure 3.4: Comparison of 1650 nm pump spectrum before and after the Kerr medium. The pump spectrum with an initial FWHM of 32.2 nm (blue) is illustrated (a) before and (b) after the 1 m length of SMF-28, with an average pump power of 2.5 nJ/pulse. The pump spectrum with an initial FWHM of 23.6 nm (red) is illustrated (c) before and (d) after the fibre, with an average pump power of 2.7 nJ/pulse.

these observations suggest that the temporal profile of the pump evolves drastically due to dispersion and/or nonlinear effects in the fibre, reducing the peak pulse intensity at a given average power.

Upon moving the ND filters to front-attenuate the signal, the noise counts due to nonlinear broadening of the pump saturated the detectors at the optimal pump power and proved to be too large to take any measurements, even after attempting to reduce the nonlinear broadening by further reducing the initial pump spectral width using the $4f$ pulse shaper.

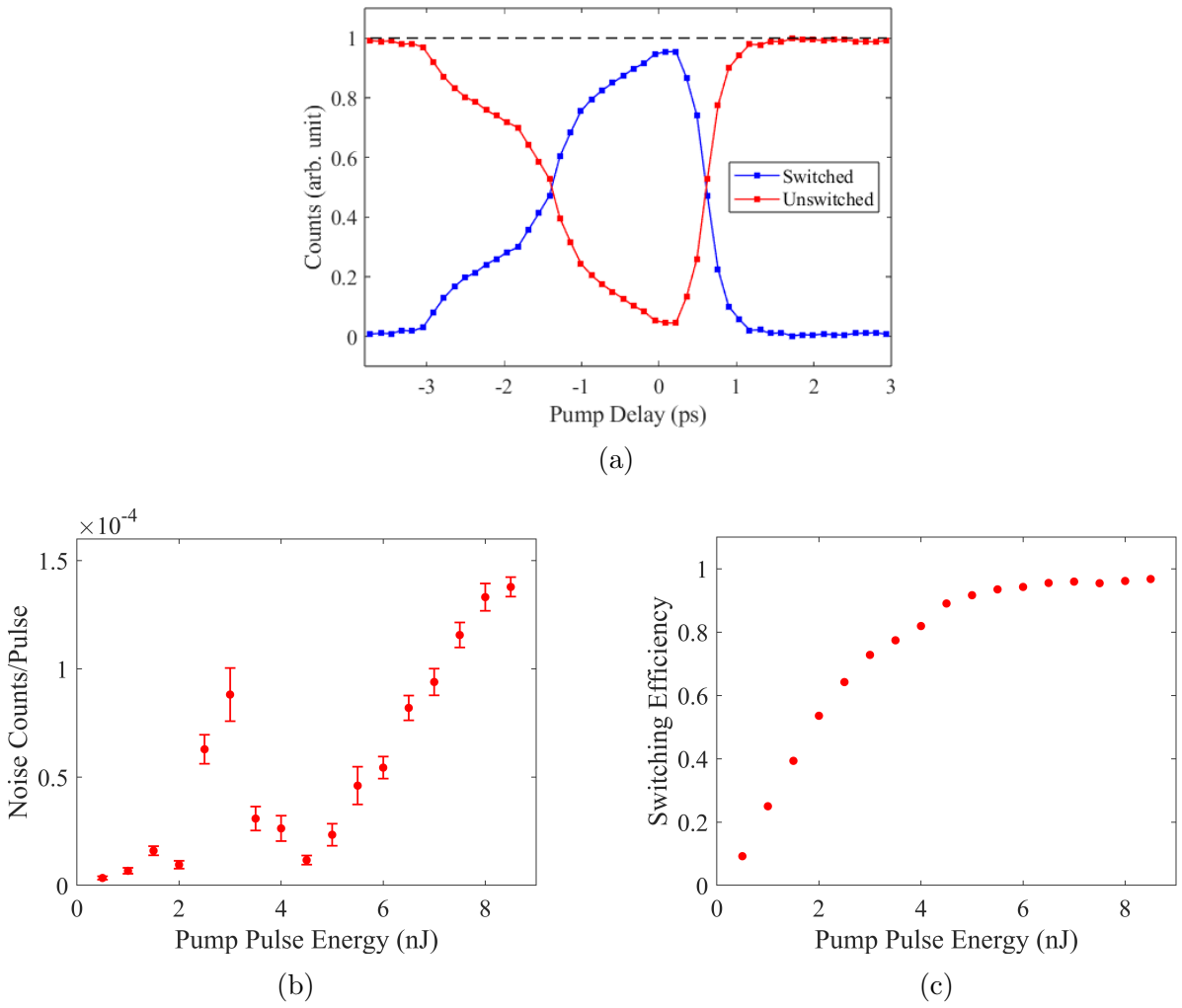

Figure 3.5: Switching response and intrinsic noise of a C-band Kerr switch with back-attenuation. The switch is implemented with the following parameters: $\lambda_s = 1550$ nm, $\Delta\lambda_s = 25$ nm, $\lambda_p = 1650$ nm, $\Delta\lambda_p = 23.6$ nm. (a) Temporal profile for the Kerr switch measured at a pump pulse energy of 6.5 nJ. (b) Intrinsic noise of the Kerr switch vs pump pulse energy, relative to the repetition rate of 80 MHz. Error bars reflect the standard deviation in the measured noise count rate at each pump power. (c) Peak switching efficiency vs pump pulse energy. Error bars are omitted as only one trial was performed at each pump pulse energy. The solid lines in (a) are guides for the eye.

Therefore, while the switch demonstrates near-unity polarization switching of single photons, the intrinsic noise due to the pump is far too large for it to be used as a temporal noise filter in the configuration tested. Further investigation will be required in order to mitigate leakthrough noise due to the pump.

3.5 Preliminary results for O-band signal switching

Before further investigating methods to mitigate pump leakthrough for the C-band switch, we proceeded to experimentally assess switching of O-band signal photons to see if the problem persists. This section discusses the necessary changes to the experimental setup to implement an O-band Kerr switch, and preliminary experimental switching results.

Relatively minimal reconfiguration was required in order to adapt the setup for O-band switching. To generate the signal pulses, the 1550 nm bandpass filter after the PCF was replaced with a 1.3 µm bandpass filter (Thorlabs FBH1300-12). The spectral parameters of the signal are $\lambda_s = 1295$ nm and $\Delta\lambda_s = 14.6$ nm, while the pump was set to $\lambda_p = 1550$ nm, $\Delta\lambda_p = 32.7$ nm to correspond with a transform-limited temporal FWHM of 108 fs. As before, $\Delta\lambda_s$ and $\Delta\lambda_p$ are the spectral FWHM of their respective fields. The pump is spectrally eliminated after the switching fibre using a combination of bandpass and shortpass filters (2 x Thorlabs FBH1300-30 and 1 x AVR Optics FF01-1326/SP-25) which collectively provide >160 dB extinction. The signal and pump spectra are depicted in Fig. 3.6.

During initial testing, the switch attained maximum switching efficiency for a pump power of 3.94 nJ/pulse with temporal FWHM of 2.4 ps, as shown in Fig. 3.7, which is consistent with the estimate from the numerical model. The pump spectrum appeared to broaden quite less considerably than that used for switching C-band signal, as shown in Fig. 3.6(c), with sufficiently low leakthrough to allow measuring with front-attenuation. However, the switching efficiency peaks only at 93% for switching both H and V polarizations.

Upon making some adjustments to the $4f$ line in an attempt to further optimize the switching efficiency, we discovered that the pump spectrum evolves differently after the switching fibre depending on the positions of the grating, mirror, and lens in the folded $4f$ line, as seen in Fig. 3.8. For the same pump power, the pump spectrum would again broaden to the point of saturating the detectors with leakthrough noise.

Until this point, it was assumed that the dominant parameter which determines the extent of the nonlinear broadening of the pump was the initial spectral width; however, it

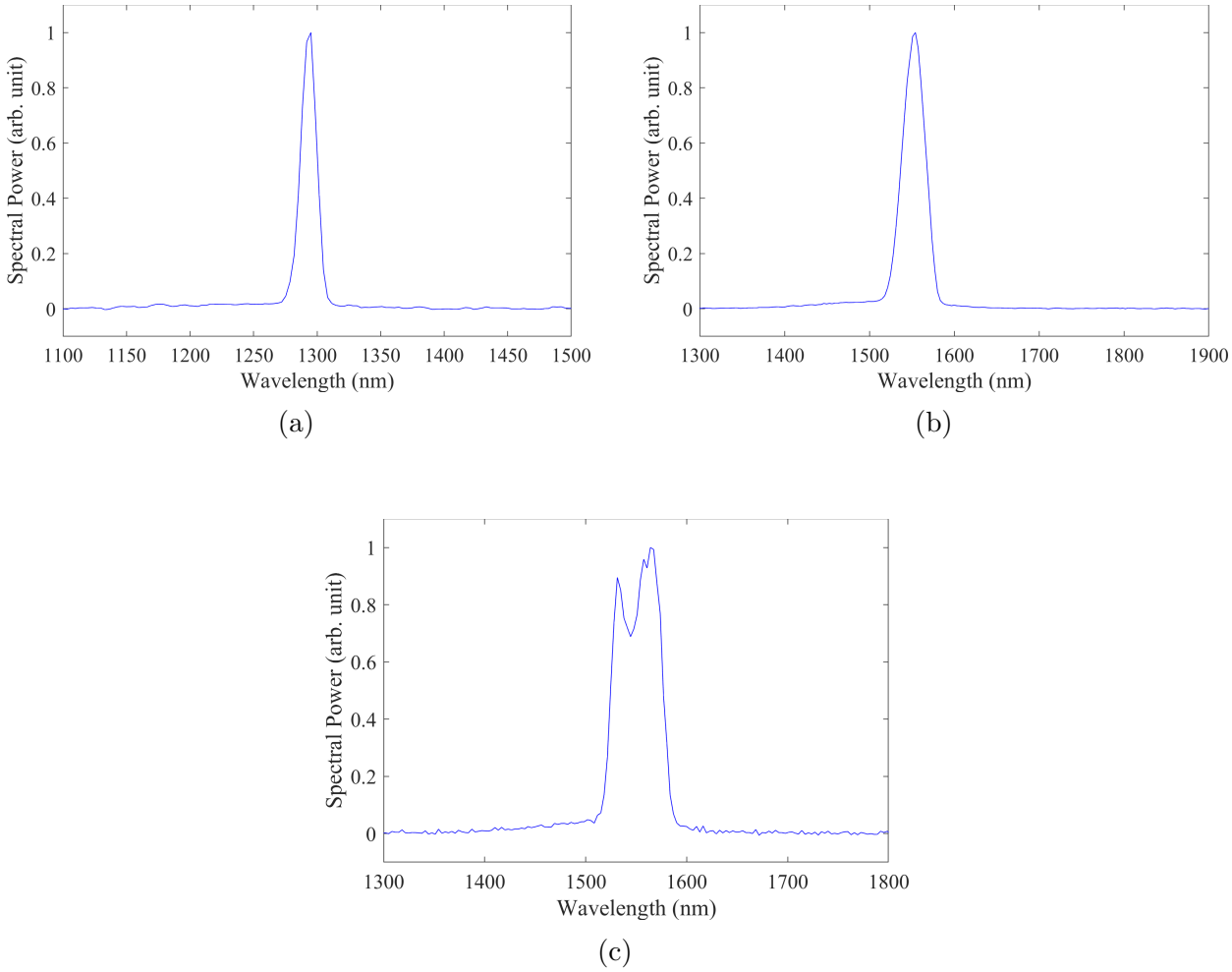

Figure 3.6: Signal and pump spectra for preliminary O-band Kerr switch experiments. The (a) signal spectrum is centred at 1295 nm with a width of 14.6 nm, and the (b) pump spectrum is centred at 1550 nm with an initial width of 32.7 nm. (c) The pump spectrum after the SMF is broadened, given a power of 3.93 nJ/pulse in the fibre.

is clear from these observations that the chirp imparted by the $4f$ line also has significant impact, as varying the positions of the lens and mirror will add group delay dispersion to the pump pulse as discussed in Section 3.2.2. We therefore turned our attention to numerically studying the nonlinear evolution of the pump to see if the impact of chirp can be predicted and controlled as a means of mitigating pump leakthrough noise.

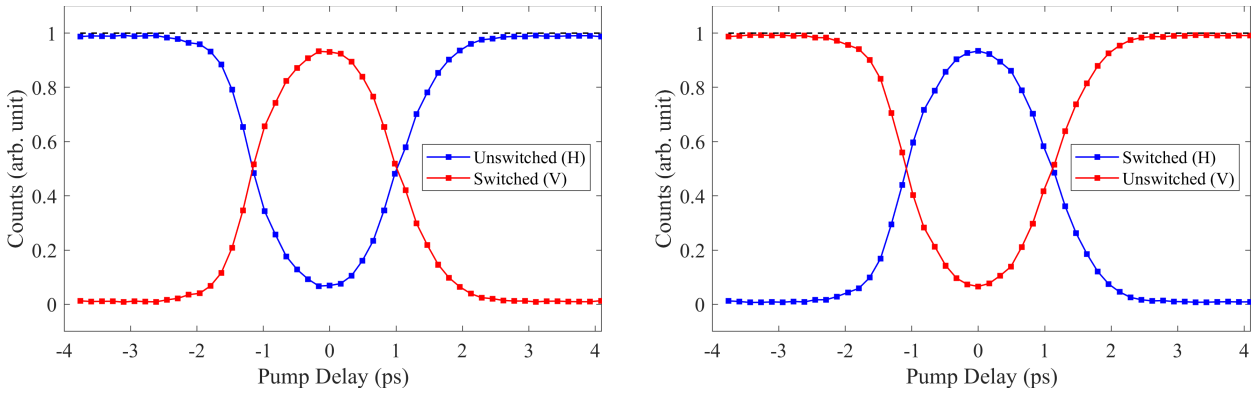

(a) (b)

Figure 3.7: Preliminary switching curves for O-band Kerr switch. (a) Switching curve for horizontal to vertical signal polarization. (b) Switching curve for vertical to horizontal signal polarization. The pump power is set to 3.94 nJ/pulse, and the initial pump bandwidth is 32.7 nm. The solid lines are guides for the eye.

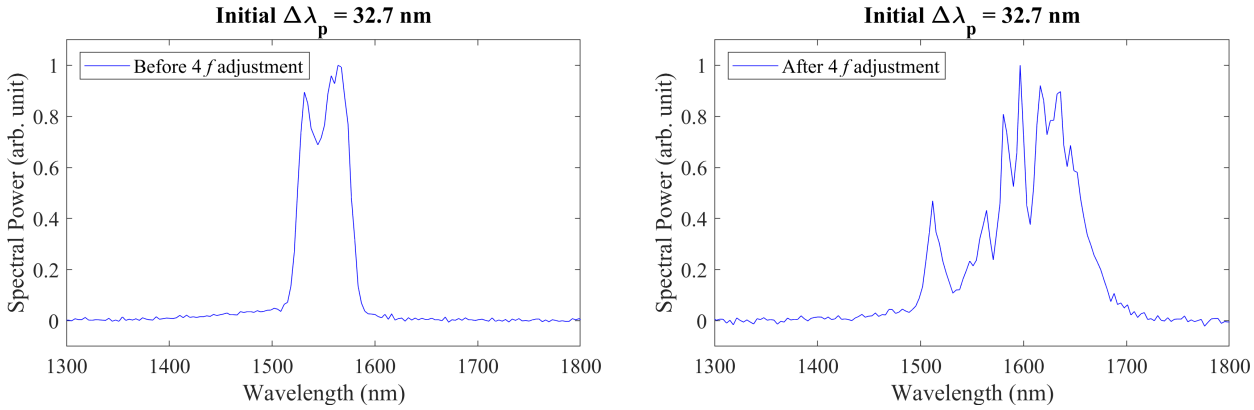

(a) (b)

Figure 3.8: Change in 1550 nm pump spectrum (a) before and (b) after $4f$ filter adjustments, for the same initial width (32.7 nm) and power (3.94 nJ/pulse).

Chapter 4

Modelling of pump field evolution

4.1 Summary

In this chapter, we study the evolution of optical pulses in single-mode fibres in order to better understand the behaviour of the pump pulses in our Kerr switch setup. We start by introducing the generalized pulse propagation equation which describes the nonlinear evolution of a pulse in a single-mode fibre, which is obtained from a theoretical treatment provided in [7]. Based on a split-step Fourier method prescription also provided in [7], we construct a numerical model to solve the generalized pulse propagation equation and validate it by comparing the resulting simulated pulse spectra with experimentally-measured spectra. Finally, we incorporate the temporally-evolving pump in our Kerr switch numerical model to predict the complete behaviour of the switch.

4.2 Generalized pulse propagation equation

Throughout our discussion of nonlinear effects in Chapter 2, we assumed an instantaneous medium response, which is valid when the length of optical pulses is large relative to the response time of the silica fibre medium. However, in order to accurately predict the nonlinear evolution of pulses, it is necessary to consider a time-varying response when the pulse width

is short compared to the Raman response time scale of 0.1 ps. Moreover, when operating away from the zero-dispersion wavelength of a fibre, we must include the effects of dispersion on the temporal shape of the pulse as it propagates [7].

As provided in [7], the evolution of optical pulses in a fibre can be described by the generalized pulse propagation equation:

$$\frac{\partial A}{\partial z} + \frac{\alpha}{2}A + \frac{i\beta_2}{2}\frac{\partial^2 A}{\partial T^2} - \frac{\beta_3}{6}\frac{\partial^3 A}{\partial T^3} = i\gamma\left(|A|^2 A + \frac{i}{\omega_0}\frac{\partial}{\partial T}\left(|A|^2 A\right) - T_R A\frac{\partial |A|^2}{\partial T}\right). \tag{4.1}$$

In the above expression, $A = A(z,T)$ is the electric field amplitude of the pulse along the axial direction, but normalized so that $|A|^2$ represents the optical power of the pulse. α is the absorption coefficient of the fibre, which is approximately 0.2 dB/km from 1490 nm to 1625 nm for SMF-28 [28]; β_2 and β_3 are respectively the second- and third-order dispersion of the fibre; and γ is the nonlinear parameter described in Section 2.3. T_R is the first moment of the Raman response function, which describes the time-dependent response of the medium, and has a value of approximately 3 fs for silica fibres [7]. It is defined as:

$$T_R = \int_{-\infty}^{\infty} tR(t)\,dt \approx f_R \int_0^{\infty} th_R(t)\,dt, \tag{4.2}$$

where the nonlinear response function $R(t) = (1 - f_R)\delta(t) + f_R h_R(t)$ accounts for both the Kerr and Raman contributions to the nonlinear response. f_R is the fractional contribution of the delayed Raman response to the nonlinear polarization P_{NL}, and $h_R(t)$ itself is the Raman response of the medium, which satisfies $\int_0^{\infty} h_R(t)\,dt = 1$ [7]. Eq. 4.1 is valid when the pulse envelope does not vary rapidly over short time scales, i.e. compared to the optical frequency [7].

In order to simulate our pump pulse evolution, we numerically solve the generalized pulse propagation equation in MATLAB using the split-step Fourier method (SSFM). The following procedure is based on an example provided in [7], but has been adapted to solve

Eq. 4.1. This numerical method first requires us to express Eq. 4.1 in the form:

$$\frac{\partial A}{\partial z} = (\hat{D}\hat{N})A, \tag{4.3}$$

where $\hat{D}$ is a differential operator that includes the effects of loss and dispersion within the medium:

$$\hat{D} = -\frac{\alpha}{2} + \frac{i\beta_2}{2}\frac{\partial^2}{\partial T^2} - \frac{\beta_3}{6}\frac{\partial^3}{\partial T^3}, \tag{4.4}$$

and $\hat{N}$ is an operator which describes the nonlinear effects within the fibre:

$$\hat{N} = i\gamma\left(|A|^2 + \frac{i}{\omega_0}\frac{1}{A}\frac{\partial}{\partial T}(|A|^2 A) - T_R\frac{\partial |A|^2}{\partial T}\right). \tag{4.5}$$

Because our switching medium fibre is only 1 metre long, we assume that optical loss is negligible and set $\frac{\alpha}{2}A = 0$ from this point forward.

The split-step Fourier method is used to obtain an approximate solution for Eq. 4.1 by assuming that the $\hat{D}$ and $\hat{N}$ operators act independently on the pulse over a small distance h so that

$$A(z+h,T) = \exp\Big[h(\hat{D}+\hat{N})\Big] \approx \exp\left(\frac{h}{2}\hat{N}\right)\exp\Big(h\hat{D}\Big)\exp\left(\frac{h}{2}\hat{N}\right)A(z,T). \tag{4.6}$$

The nonlinear and dispersion effects are applied in a "leap-frog" pattern, where the effect due to $\hat{N}$ is partially computed at both boundaries of each length segment, while the effect due to $\hat{D}$ is computed between them. Starting with an initial pulse amplitude $A(z=0,T)$, the final amplitude can be computed by sucessively applying the exponential operators over the total length of the simulated medium. If the total length L is divided into M equal segments of length h, then

$$A(z=L,T) = \exp\left(-\frac{h}{2}\hat{N}\right)\left[\prod_{i=1}^{M}\exp\Big(h\hat{N}\Big)\exp\Big(h\hat{D}\Big)\right]\exp\left(\frac{h}{2}\hat{N}\right)A(z=0,T). \tag{4.7}$$

The effect of $\hat{D}$ is computed in the Fourier domain using a fast Fourier transform (FFT) algorithm in the time domain, which allows us to replace the differential operator $\frac{\partial}{\partial T}$ with $-i\Omega$ where Ω is the Fourier domain frequency, so that

$$\hat{D} \xrightarrow{\mathcal{F}} \tilde{D}(\Omega) = \frac{i\beta_2}{2}\Omega^2 + i\frac{\beta_3}{6}\Omega^2, \tag{4.8}$$

where we have neglected the term association with optical loss and $\mathcal{F}$ denotes the Fourier transform operation. This is used to speed up computation time, as $\tilde{D}(\Omega)$ can be stored as an array of complex numbers and multiplied element-wise with an array containing the Fourier transform of the pulse amplitude, $\tilde{A}(z,\Omega) = \mathcal{F}\{A(z,T)\}$, rather than having to numerically compute the time derivatives. The pulse amplitude is then transformed back into the time domain before applying the effect of the $\hat{N}$ operators.

Before numerically solving Eq. 4.1, it is convenient to normalize it in terms of the second- and third-order dispersion β_2 and β_3 of the medium at the optical frequency ω_0; and the $1/e^2$ width T_0, peak power P_0, and dispersion length $L_D = T_0/|\beta_2|^2$ of the optical pulse. The normalized form of the equation is given by

$$\begin{aligned}\frac{\partial U}{\partial \xi} =& -\frac{i\,\mathrm{sgn}(\beta_2)}{2}\frac{\partial^2 U}{\partial \tau^2} + \frac{1}{6}\frac{\beta_3}{|\beta_2|T_0}\frac{\partial^3 U}{\partial \tau^3} \\ &+ iN^2\left(|U|^2U + \frac{i}{\omega_0 T_0}\frac{\partial}{\partial \tau}(|U|^2U) - \frac{T_R}{T_0}U\frac{\partial}{\partial \tau}|U|^2\right),\end{aligned} \tag{4.9}$$

where $\mathrm{sgn}(\beta_2) = \pm 1$ denotes the sign of β_2; and $\tau = T/T_0$, $\xi = z/L_D$, and $U = A/\sqrt{P_0}$ are the normalized time, length, and pulse amplitude, respectively. The parameter N (not to be confused with the $\hat{N}$ operator) is the soliton order of the pulse and is given by $N^2 = \gamma P_0 T_0^2/|\beta_2|$ [7]. The normalized $\hat{D}$ and $\hat{N}$ are therefore given by

$$\hat{D}_n = -i\frac{\mathrm{sgn}(\beta_2)}{2}\frac{\partial^2}{\partial \tau^2} + \frac{1}{6}\frac{\beta_3}{|\beta_2|T_0}\frac{\partial^3}{\partial \tau^3} \tag{4.10}$$

and

$$\hat{N}_n = iN^2 \left(|U|^2 + \frac{i}{\omega_0 T_0} \frac{1}{U} \frac{\partial}{\partial \tau} (|U|^2 U) - \frac{T_R}{T_0} \frac{\partial}{\partial \tau} |U|^2 \right). \tag{4.11}$$

The values of β_2 and β_3 for SMF-28 can be obtained from the dispersion parameter $D_{\text{fibre}}(\lambda)$ (see Section 2.6) using the relations:

$$\beta_2 = -\frac{\lambda^2}{2\pi c} D_{\text{fibre}}(\lambda) \tag{4.12}$$

$$\frac{dD_{\text{fibre}}}{d\lambda} = \left(\frac{2\pi c}{\lambda^2} \right)^2 \beta_3 + \frac{4\pi c}{\lambda^3} \beta_2 \tag{4.13}$$

Using the above normalization, the amplitude of simulated unchirped Gaussian pulse launched into the fibre is simply given by $U(\xi = 0, \tau) = \exp(-\tau^2/2)$. However, a pulse with a linear chirp is instead given by

$$U(\xi = 0, \tau) = \exp\left(-\frac{1 + iC}{2} \tau^2 \right). \tag{4.14}$$

C is the dimensionless chirp parameter, and is positive for positively-chirped pulses (i.e., pulses whose frequency increases from front to back) and negative for negatively-chirped pulses. For a pulse with a fixed spectral $1/e^2$ width $\Delta\omega$, C has the effect of increasing the temporal width so that:

$$1 + C^2 = \Delta\omega^2 T_0^2. \tag{4.15}$$

The chirp parameter is related to the total GDD applied to a pulse, and carries the same sign:

$$C = \text{GDD} \cdot \Delta\omega^2, \tag{4.16}$$

or, in terms of the spectral wavelength FWHM $\Delta\lambda$:

$$C = \text{GDD} \cdot \frac{c^2 \pi^2}{\lambda_0^4 \ln 2} \Delta\lambda. \tag{4.17}$$

As discussed in Section 3.2.2, the setup of the folded $4f$ pulse shaper can be tuned in order to impart a chirp onto the pump pulse, per Eq. 3.5. Therefore, experimentally applying GDD onto a pulse amounts to adjusting the position of the lens and mirror relative to the reflective grating.

4.3 Mitigating spectral broadening

We implement the SSFM in MATLAB to simulate the propagation of a 1550 nm pump pulse through a length of SMF-28 Ultra fibre, and study the effect of initial spectral width and chirp on the nonlinear evolution of the pulse. The script for the SSFM is provided in Appendix A.1. Throughout all simulations, we set the following fixed parameters: $L = 1$ m, and $\lambda_p = 1550$ nm.

The effect of chirping the pulse is illustrated in Fig. 4.1. Here, we set $\Delta\lambda_p = 32.7$ nm and the optical power to 3.94 nJ/pulse to match the pump parameters used in the preliminary O-band switching experiments at the end of the previous chapter. As seen in Fig. 4.1(a), an unchirped pulse with GDD = 0 fs^2 begins to temporally narrow over the first several cm of the fibre, resulting in an increasing peak intensity. After approximately 8 cm, the intensity appears to peak, to the point where higher-order dispersive and non-linear effects cause the pulse to undergo soliton fission. Due to Raman scattering, this results in the transfer of energy into a dispersive wave with a distinct, frequency-downshifted spectral peak that travels at a slower group velocity than the original pulse [7]. The central peak itself has also broadened and developed fringes; these fringes suggest that the central peak in fact consists of two temporally-separated solitons, which collectively interfere to produce spectral modulation (analogously to two spectrally-separated coherent fields interfering to create temporal modulation) [7]. Soliton fission still occurs when the pulse is given an initial positive or negative chirp of GDD = $\pm$ 15000 fs^2, as shown in Fig. 4.1(b) and (c); however, in both cases it occurs later in the fibre. In the case of a positively-chirped pulse, this can

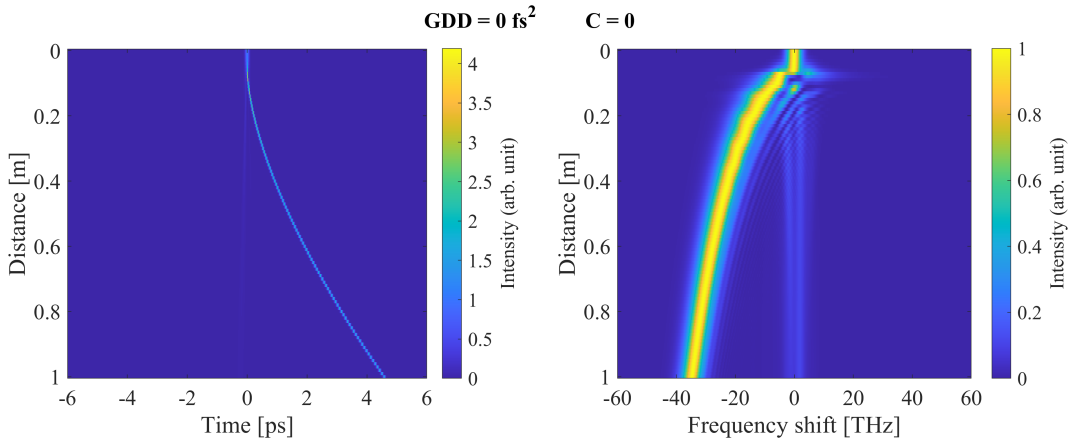

(a)

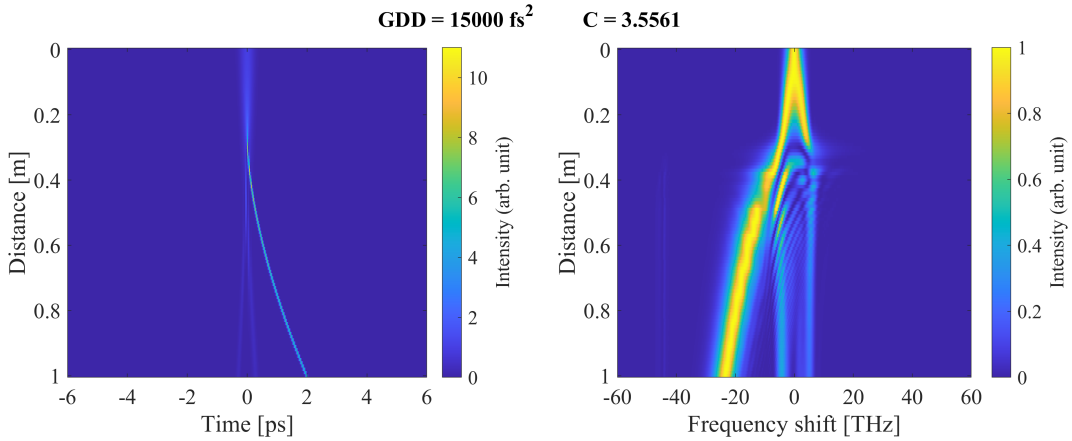

(b)

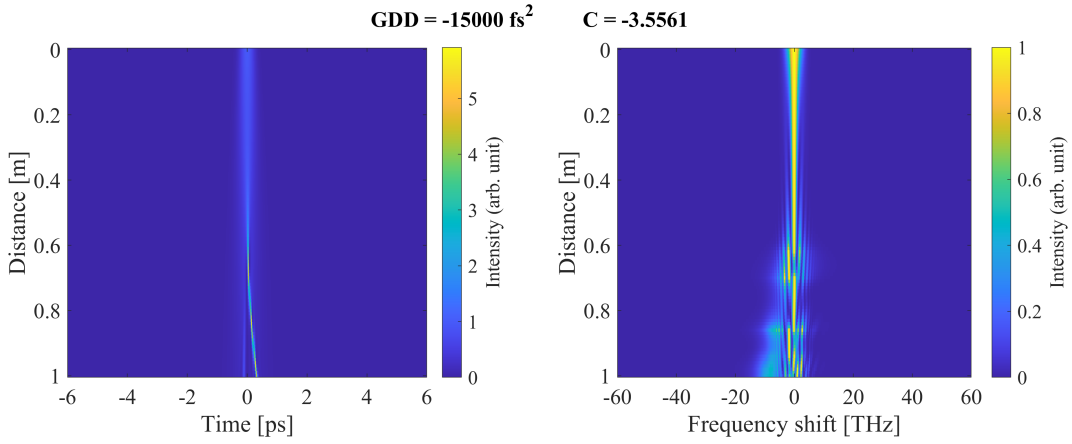

(c)

Figure 4.1: Simulated evolution of 1550 nm pump pulses for different initial chirps. The input pulse has an energy of 3.94 nJ and is initially given (a) no chirp (GDD = 0 fs^2), (b) a positive chirp (GDD = +15000 fs^2), and (c) a negative chirp (GDD = -15000 fs^2). In all three cases, the pulse undergoes soliton fission, resulting in a corresponding broadening of the spectral profiles; however, fissioning is delayed for chirped pulses.

be attributed to the anomalous dispersion "canceling out" the initial chirp so that the pulse travels longer in the fibre before fissioning. In contrast, the spectrum of a negatively-chirped pulse initially narrows due to self-phase modulation, before broadening with an oscillatory structure. The pulse begins to narrow in time as the spectrum broadens, which results in an increase in the peak intensity before the pulse eventually undergoes fission [7].

To validate our numerical model, we compare our simulated output spectra with spectral data measured in the lab. The pump spectrum is measured after the switching fibre for input powers of 1.25 nJ/pulse, 2.5 nJ/pulse, and 3.94 nJ/pulse. The pump is given an initial spectral FWHM of 32.7 nm, which is set by tuning the variable slit width. The positions of the components in the $4f$ line are set by eye so that the grating-to-lens and lens-to-mirror distances are both kept at approximately $f = 15$ cm, producing the output spectrum seen in Fig. 3.8(b). Within the MATLAB script, the initial GDD is manually adjusted until the simulated output spectrum is good agreement with the corresponding measured output spectra at all three optical powers. As shown in Fig. 4.2, the SSFM model closely replicates the experimental nonlinear evolution of the pump when the initial GDD is set to +25730 fs^2. As the optical power increases, the spectrum broadens considerably between 1500 nm and 1700 nm and develops additional peaks. At 3.94 nJ/pulse, most of the power has down-shifted in frequency; this behaviour is consistent with the simulated soliton fission in Fig. 4.1.

To further assess the effect of reducing the pump bandwidth, simulated and experimental spectra are also compared for $\Delta\lambda_p = 25$ nm. The experimental pulses are produced with the pulse shaper components kept in the same positions as per the 32.7 nm bandwidth pulses, to maintain the same GDD of +25730 fs^2. Only the variable slit width is reduced in order to tune the initial pump spectral width. As shown in Fig. 4.3, reducing the initial spectral width has relatively minimal impact on the output spectral width at higher powers, compared to the 32.7 nm pulses. In both cases, soliton fission causes the spectrum to broaden significantly across the range of 1500 nm to 1700 nm. The SSFM model still

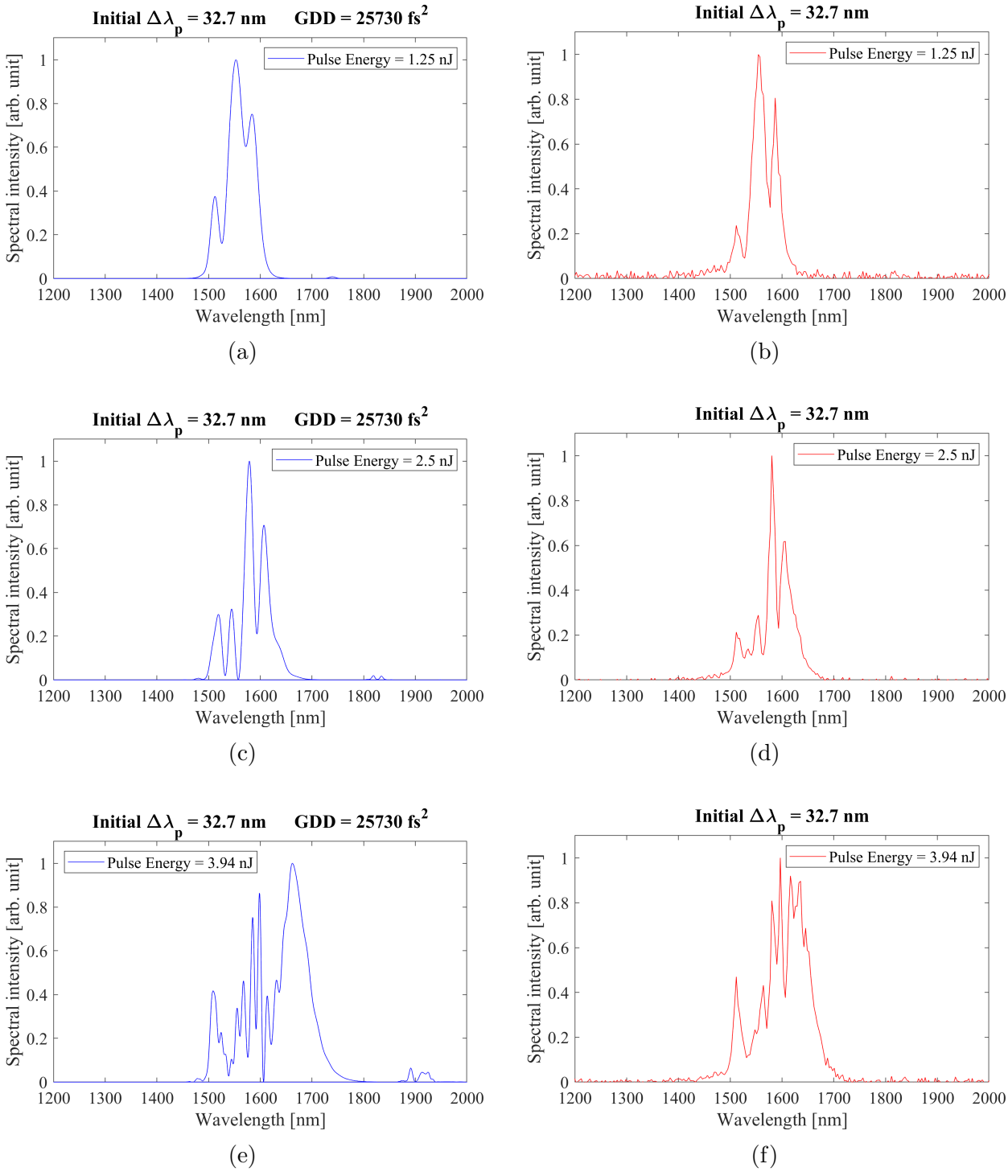

Figure 4.2: Comparison of simulated vs measured 1550 nm pump spectra at different powers, given an initial 32.7 nm bandwidth. The simulated (blue) and experimentally measured (red) pump spectra are depicted for pulse energies of (a)(b) 1.25 nJ; (c)(d) 2.5 nJ; and (e)(f) 3.94 nJ, respectively. The simulated pulses are initially positively chirped, with GDD = +25730 fs^2

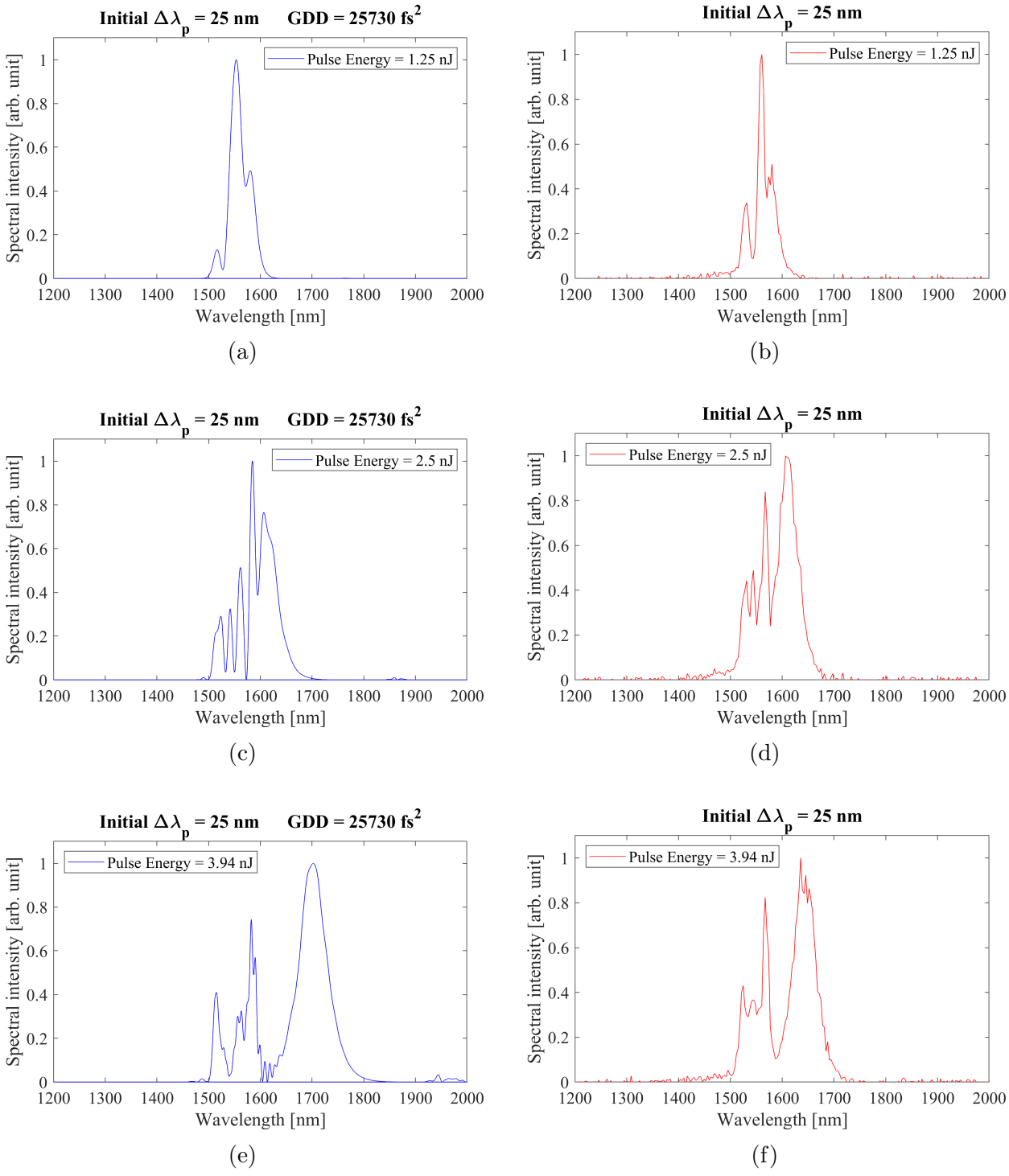

Figure 4.3: Comparison of simulated vs measured 1550 nm pump spectra at different powers, given an initial 25 nm bandwidth. The simulated (blue) and experimentally measured (red) pump spectra are depicted for pulse energies of (a)(b) 1.25 nJ; (c)(d) 2.5 nJ; and (e)(f) 3.94 nJ, respectively. The simulated pulses are initially positively chirped, with GDD = +25730 fs^2

accurately reproduces the overall spectral evolution, although with slightly less agreement with the extent of the spectral broadening. This could be attributed to the model using a Gaussian profile for the initial pulse spectrum. In reality, the folded $4f$ line acts like a box-top filter; therefore, only the 32.7 nm pulses produced with the slit completely open are expected to have a Gaussian spectrum.

The good agreement between the simulated and experimental pulse evolution suggests that the model can be reliably used to estimate the GDD applied by the $4f$ pulse shaper, allowing us to control the initial chirp by appropriately tuning the lens and mirror positions according to Eq. 3.5.

Using the SSFM model, we are able to avoid soliton fission and minimize spectral broadening by applying a sufficiently large positive chirp to the pulse. As shown in Fig. 4.4, a 32.7 nm bandwidth pulse with GDD = +60000 fs^2 broadens to a spectral FWHM of 52.2 nm, and closely reproduces the shape of the low-noise output pump spectrum seen in Fig. 3.8(a). We can therefore attribute the observed changes in the output pump spectrum to the adjustments made to the lens and mirror positions during realignment of the $4f$ line. Moreover, we remark that setting an appropriate chirp is more important in minimizing the spectral noise generated by the pump in our Kerr switch, compared to naively adjusting the initial bandwidth.

4.4 Modelling switching response with evolving pump

Because the SSFM model produces the temporal profile of the pump pulse as it propagates through the fibre, we can incorporate it into the numerical model for the Kerr switch model first discussed in Section 2.6. Doing so allows us to predict the switching response while factoring in dispersive and nonlinear effects at a given chirp and optical power. Although the nonlinear phase is still calculated by integrating the pump intensity profile I_p using Eq. 2.28, the changing shape of $I_p(T, z)$ must be taken into account when integrating over the

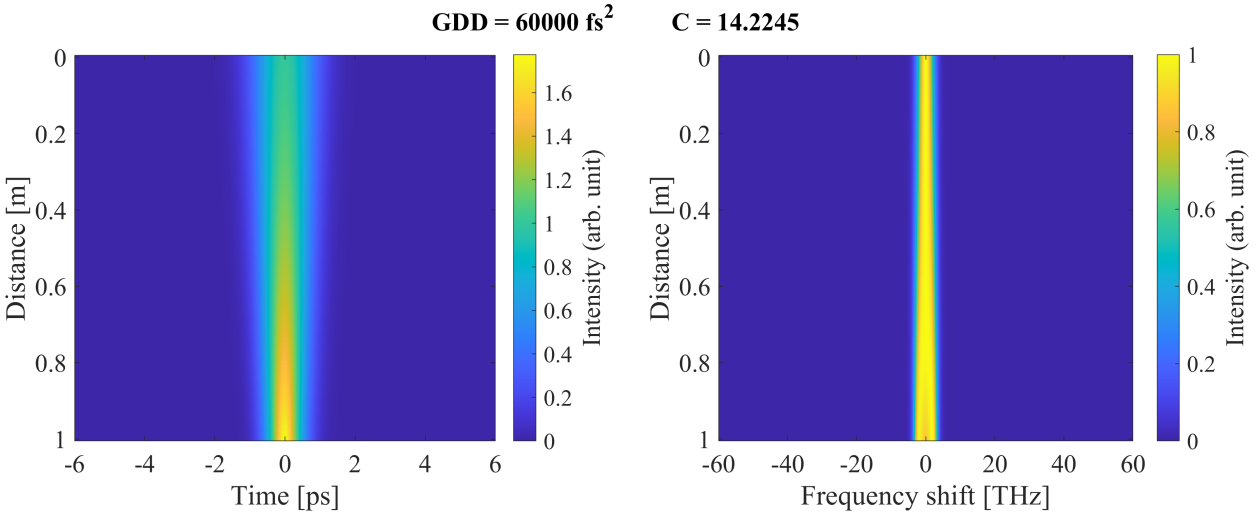

(a)

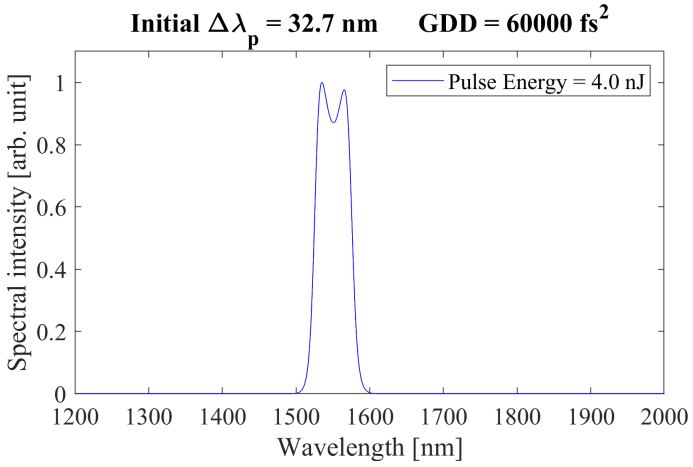

(b)

Figure 4.4: Simulated temporal and spectral evolution of positively-chirped 1550 nm pump pulse with an initial 32.7 nm width. The evolution over 1 m length of SMF-28 is depicted in (a), and the spectrum at the output of the fibre is given in (b). The simulated pulse has an energy of 4.0 nJ and is initially positively chirped, with GDD = +60000 fs^2

fibre length as the pulse propagates.

The fully-simulated Kerr switching response is shown in Fig. 4.5, and is computed using the MATLAB script provided in Appendix A.2. Here, we compute the pulse switching efficiency $\eta_{\text{pulse}}(T)$ according to Eq. 2.30, where we estimate the 1295 nm signal pulse has a temporal width of 300 fs. This is based on an initial spectral width of 14.6 nm (as shown in Fig. 3.6), and the dispersion characteristics of the PCF used in the supercontinuum source. At 1.3 µm, the PCF has a dispersion parameter of approximately $D = 60$ ps/(nm · km) at this wavelength (as provided by the manufacturer). Assuming the signal wavelength is generated early in the PCF, the signal pulse will continue to travel through approximately 30 cm of PCF and become negatively chirped. Because the signal wavelength is relatively close to the SMF-28 zero dispersion wavelength of 1317 nm, we assume that the pulse does not undergo signficiant temporal broadening in the switching fibre itself.

As shown in Fig. 4.5(b), using an initial chirp of GDD = +60000 fs^2 we find that that the total switching efficiency η_{pulse} reaches unity at time zero with an optical pump power

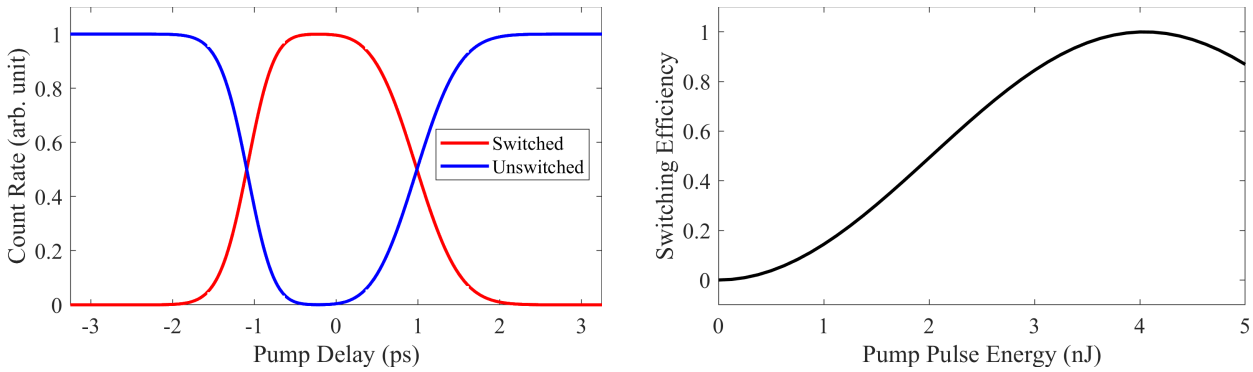

(a) (b)

Figure 4.5: Simulated Kerr switching response with evolving positively-chirped 1550 nm pump pulse. (a) Pulse switching efficiency vs delay for a pump with an initial spectral width of 32.7 nm, a power of 4.00 nJ/pulse, and an initial GDD of 60000 fs^2. (b) The maximum pulse switching efficiency is plotted from 0 to 5 nJ/pump pulse, and reaches a peak at 4.00 nJ/pulse.

of 4.00 nJ/pulse. At this power, the switching curve in (a) has a FWHM of 2.1 ps, and remains within 2% of the maximum value over a flat-top width of 0.76 ps. Because of the continuous evolution of the pump pulses, the pulse switching curve is slightly asymmetric but still closely resembles the curve obtained in Fig. 3.7. The shallow slopes of the curve compared to the simple numerical model can be attributed to the initial chirp significantly widening the initial pulse to T_{FWHM} to 1542 fs, compared to the Fourier-limited value of 108 fs. In spite of this, the picosecond-scale width is promising for using the switch as a temporal filter. In the next chapter, we revisit the experimental setup with a controlled initial pump chirp.

Chapter 5

Experimental results with pulse shaping

5.1 Summary

Now armed with the insight of how chirp affects the pump pulse propagation, in this chapter we revisit the experimental setup for switching O-band single photons, while controlling chirp in order to reduce nonlinear spectral broadening of the pump. We accordingly characterize the the Kerr switch performance, and demonstrate the use of the Kerr switch in temporally filtering out CW noise in a quantum channel.

5.2 Switching response with chirped pump

Based on the simulated pulse propagation and Kerr switching response in Section 4.4, we adjust the lens and mirror positions in the $4f$ line in order to apply an initial GDD of approximately +60000 fs^2. Using Eq. 3.5, and with the grating incidence and diffraction angles set to $\theta_i = 49.1°$ and $\theta_d = 10°$, respectively. This is achieved by collectively moving the lens and mirror closer to the grating by $\Delta f = 3$ cm so that the grating-lens distance is 12 cm and the lens-mirror distance is $f = 15$ cm. As before, we proceed to scan through the

pump-signal delay for pump powers ranging from 0.0 to 5.0 nJ/pulse, and measure both the corresponding switching curve and intrinsic noise of the switch. To obtain uncertainties for the switching efficiency at each pump power, we take the standard deviation across 5 trials. As before, the uncertainty of the noise level is based on the standard deviation across 50 measurements of the noise count rate in the switched channel. The setup is configured to switch signal photons from V to H, and the ND filters are positioned to front-attenuate the signal.

While scanning the delay stage position over a large range, we notice that our Kerr switching response appears to consist of two peaks with differing heights. The presence and relative heights of these peaks is correlated with the coupling of light into a higher-order spatial mode in the PCF used to generate our signal field. Due to the group velocity mismatch of the different spatial modes, one 1040 nm pulse coupled into the PCF produces multiple signal pulses separated slightly in time, each of which has a different "time zero" in the Kerr switching response. Depending on the adjustment of the coupling into the PCF, these peaks are separated by approximately 10 to 18 ps in pump-signal delay, which is much shorter than the pulse repetition period of $1/(80\text{ MHz}) = 12.5$ ns.

We qualitatively observe the spatial distribution of the output supercontinuum pulses using a monochromatic camera, and measure the corresponding switching response vs delay. As shown in Fig. 5.1, when the spatial distribution of the output field visually resembles a TEM_{10} Hermite-Gaussian mode, the switching response has two distinct peaks of comparable height. If the spatial distribution instead resembles a TEM_{00} mode, one switching peak is more dominant. This higher-order fibre mode effectively introduces an additional temporal mode into our signal, since the pump pulses can only switch the signal pulses from one mode at a time. To account for this in our data processing procedure, we first record the time zero delay stage positions for each of the observed peaks, then determine the maximum switching efficiency at a given pump power by adding the ratios of switched vs. unswitched counts at

each of the time zero positions TZ1 and TZ2, so that

$$\eta_{\text{pulse}} = \frac{\text{Switched count rate at TZ1}}{\text{Total count rate at TZ1}} + \frac{\text{Switched count rate at TZ2}}{\text{Total count rate at TZ2}}. \tag{5.1}$$

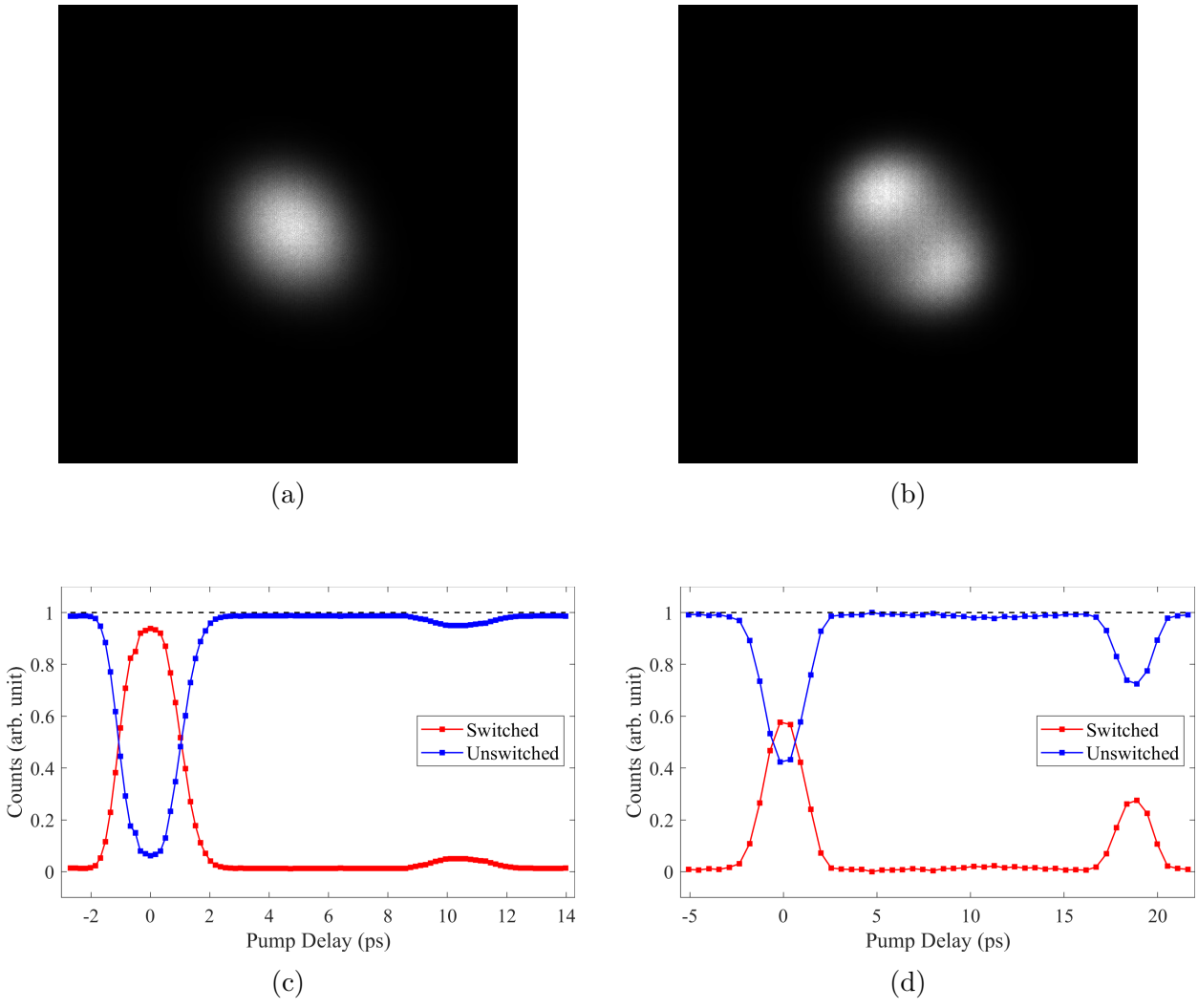

Figure 5.1: Observation of higher-order spatial mode from the photonic crystal fibre and comparison of switching curves. The spatial intensity profile of the supercontinuum generated in the PCF is measured by a monochromatic infrared camera, and contrast-enhanced to produce (a) and (b). In (a), the light is predominantly from the fundamental mode of the PCF, resulting in the switching curve in (c). In (b), the light originates from a higher-order transverse mode in the PCF, resulting in the switching curve in (d). The solid lines are guides for the eye.

However, in evaluating the temporal width of the Kerr switch, we only focus on the switching peak associated with the fundamental mode of the PCF. The resulting performance of the Kerr switch is summarized in Fig. 5.2. As seen in Fig. 5.2(a), the switching efficiency at time zero vs. pump power follows the expected $\sin^2$ dependence given by Eq. 2.29, and reaches a near-unity maximum value of $\eta_{\text{pulse}} = 98.77 \pm 0.01\%$ at a pump power of 4.0 nJ/pulse. At this pump power, the switching curve has a temporal FWHM of 2.4 ps as shown in Fig. 5.2(b). The switching efficiency stays within 2% of the peak over a flat-top of approximately 0.9 ps. The switch performance shows good agreement with the SSFM model, including the optimal pump power required for maximum switching, although the width of the switching curve is slightly larger. This is likely due to slight discrepancies in the dispersion and/or length of the fibre. The switching efficiency does not reach 100%, but this could be due to limitations of the broadband waveplates used to control the signal polarization in the setup, which may leave residual elliptical polarization.

As shown in Fig. 5.2(c), the positively-chirped pump undergoes relatively minimal nonlinear spectral broadening, and expands to a FWHM of 43.4 nm. Although the pump broadening is less than what was predicted in Fig. 4.4, this is likely attributable to the imprecision in measuring the exact positions of the $4f$ pulse shaper components, which were placed by eye. The leakthrough noise increases monotonically with pump power but remains low, reaching a value of $(2.26 \pm 0.08) \times 10^{-4}$ counts/pulse at the optimum pump power of 4.0 nJ/pulse, as shown in Fig. 5.2(d).

In summary, our switch successfully demonstrates near-unity Kerr switching of O-band signal photons. Our results indicate that our SSFM model successfully predicts the performance of our setup, and confirms that positively chirping the pump can keep the intrinsic noise of the Kerr switch low by minimizing pump leakthrough.

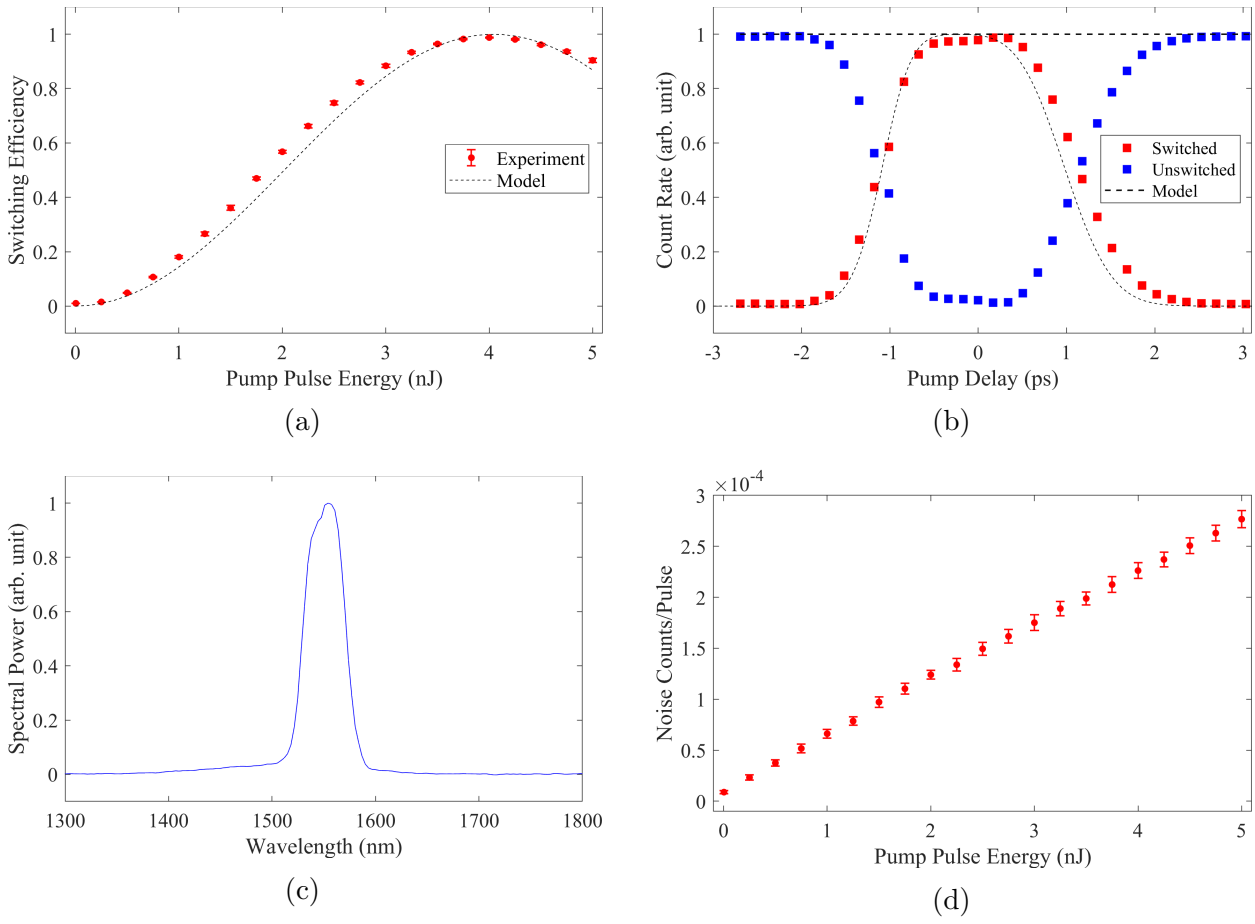

Figure 5.2: Measured Kerr switch characteristics with positively-chirped 1550 nm pump. The pump has an initial width and power of 32.7 nm and 4.0 nJ/pulse, respectively. (a) The peak switching efficiency at time zero reaches a peak of $98.7 \pm 0.01\%$ at a pump power of 4.0 nJ/pulse. The error bars reflect the standard deviation across 5 trials at each pump power. (b) The switching curve at the optimum pump power of 4.0 nJ/pulse has a temporal FWHM of 2.4 ps. (c) The corresponding pump spectrum measured after the switching fibre has a broadened width of 43.4 nm. (d) The noise counts vs. pump power reaches a rate of 2.3×10^{-4} counts per pulse at the optimum pump power. The error bars reflect the standard deviation in the measured noise count rate at each pump power. Note that the signal counts associated with the higher order PCF mode were subtracted from the total counts to produce the plot shown in (b).

5.3 Demonstration of temporal noise rejection

Now that we have determined the optimal configuration for Kerr switching, we are at last ready to demonstrate temporal noise filtering using the Kerr switch. In the previous section, we demonstrated that the Kerr switch allows photons to be switched and detected with near-unity efficiency, provided they are appropriately synchronized with the pump. Our goal is to now show that the Kerr switch simultaneously allows us to reject noise photons, distributed randomly in time, which fall outside of the switching window.

We introduce a CW laser (Newport LPM1310-05E) into our setup to emulate random noise present in a quantum channel. As shown in Fig. 5.3, this source has an O-band wavelength of $\lambda_{\text{noise}} = 1310$ nm and a spectral FWHM of $\Delta\lambda_{\text{noise}} = 10.8$ nm, which was chosen in order to fall within the pass band of the spectral filters. As shown in Fig. 3.1, the CW field is combined with the signal field using a 50:50 beamsplitter, before both fields pass through the PBS, ensuring that they are co-polarized. An ND wheel positioned in front of the CW laser is used to manually tune the optical power.

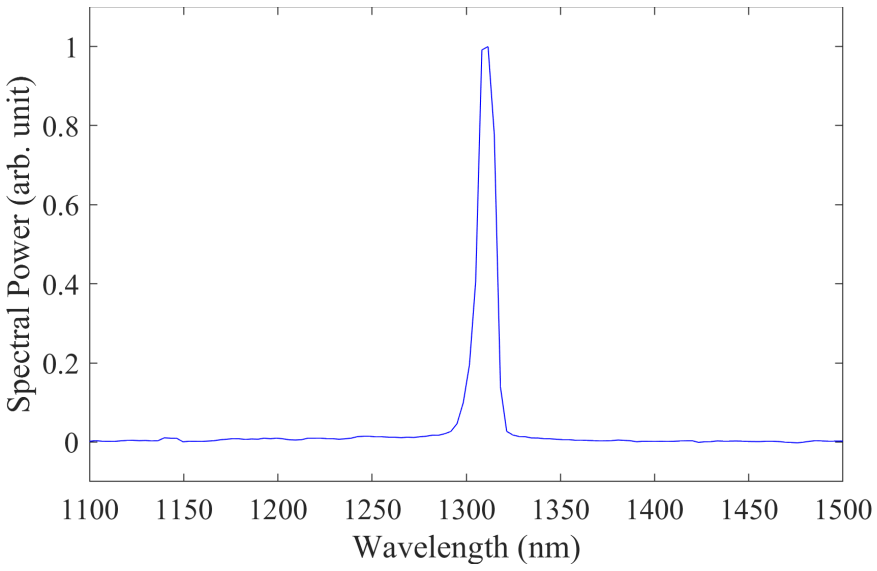

Figure 5.3: Spectrum of CW 1310 nm noise source. The FWHM is 10.8 nm.

Switch status	**Pump status**	**Measurement channel**
On	Unblocked	Ch 1: Switched counts (H)
Off	Blocked	Ch 2: Unswitched counts (V)

Table 5.1: Measurement configurations for noise rejection demonstration.

To demonstrate noise rejection, we vary the amount of CW light introduced into the quantum channel using the ND wheel, with the signal itself turned off. For each CW attenuation level, we measure and compare the SNSPD count rates with Kerr switching turned off (i.e. pump field blocked) and with Kerr switching turned on (i.e. pump field unblocked). When Kerr switching is off, the unswitched count rate is measured; and when Kerr switching is on, the switched count rate is measured. With the pump field off, the unswitched counts define the amount of noise photons introduced into the quantum channel. They also represent Bob's measurements *without* temporal filtering. With the pump field on, the switched counts correspond to Bob's measurements *with* temporal filtering. For clarity, the measurement configurations for this procedure is summarized in Table 5.1. The amount of CW light introduced into the setup is logarithmically increased over a range of 1.8×10^3 counts/second to 7.6×10^6 counts per second. This upper limit was set by the saturation limit of the detectors.

The noise filtering results are illustrated in Fig. 5.4. In Fig. 5.4(a), we compare the background rate per pulse vs. the amount of noise counts introduced into the quantum channel when the Kerr switch is on and off. Although the presence of the pump results in a noise floor of 2.2×10^{-4} counts/pulse due to pump leakthrough, we see a net reduction in detected noise counts when more than 1.8×10^4 counts/second are introduced into the quantum channel. At the maximum introduced noise level of 7.6×10^6 counts/second (near the saturation limit of the detectors), we observe an overall reduction in the detected noise counts by 18.2 dB.

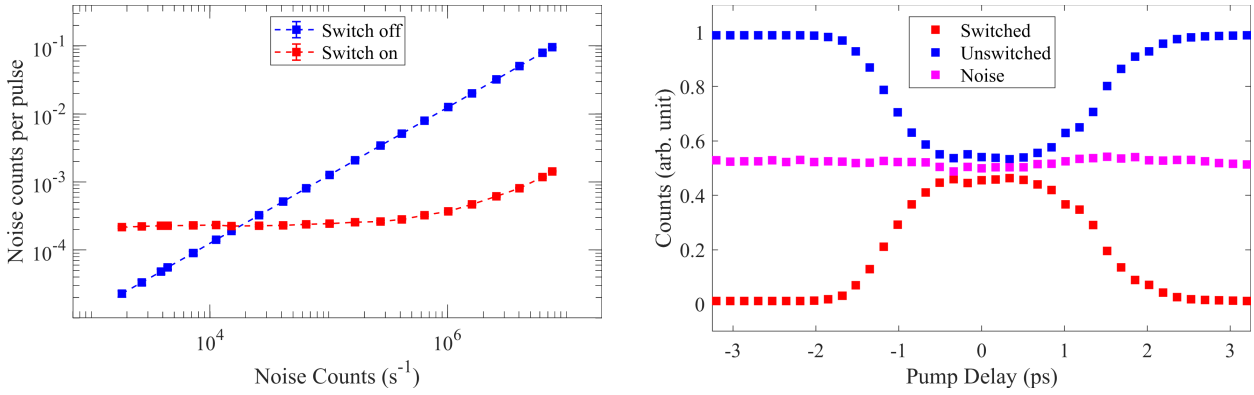

Figure 5.4: Noise rejection of O-band Kerr switch. The pump is set to 4.0 nJ/pulse to provide optimal switching. (a) Total noise counts detected in the "switched" path with pump field on (red) and total noise counts detected in the "unswitched" path with the pump field off (blue), vs the number of noise counts introduced by the CW noise source. (b) Switching curve when noise counts (pink) are introduced into the channel together with the signal so that on average the noise contributes approximately half of the total counts (blue) detected in the "unswitched" path.

To confirm that the CW photons are largely filtered out while the signal photons are permitted to pass, we perform a delay scan as depicted in Fig. 5.4(b) to measure Kerr switching when both signal and noise are present in the quantum channel with comparable count rates. The magenta curve indicates the unswitched counts when only CW noise is present; the blue curve represents the unswitched counts when both signal *and* noise are present; and the red curve shows the switched counts. The pump is on and set to 4.0 nJ/pulse for all measurements. As the delay is scanned, we observe the familiar Kerr switching trace; except that at time zero, the unswitched count rate decreases until it approximately reaches the level of the raw CW counts. Because the remaining unswitched count rate remains above the CW background, this suggests that it is primarily signal pulses synchronized with the pump that are getting switched, while the randomly-distributed noise photons are mostly unaffected. We note that the unswitched counts do not quite reach the noise floor level due to the aforementioned presence of delayed higher-order PCF modes, which effectively increases the noise floor slightly when the signal is turned on. During these measurements,

the signal and noise levels are both set to approximately 0.05 photons/pulse (as measured at the SNSPDs).

The results from this proof-of-principle demonstration show that our telecom Kerr switch setup is able to temporally filter out random noise from a quantum channel, while allowing the desired signal photons to pass through with near-unity efficiency and be detected. This is in spite of our emulated noise field having a similar wavelength as the signal and having a comparable average optical power. We remark that the noise reduction factor of 18.2 dB could be readily improved by shortening the switching fibre to narrow the width of the switching curve until the flat-top is eliminated. Shortening the fibre would also have the benefit of reducing the relative impact of nonlinear effects on the pump field, which means less chirping would be required to limit leakthrough noise.

Chapter 6

Conclusions and future work

6.1 Project summary

In this work, we have implemented an ultrafast, all-optical Kerr switch in a 1-m length of SMF-28 single-mode fibre (SMF), and demonstrated its use as a temporal gate to filter out noise in a telecom quantum key distribution (QKD) optical channel. Our setup enables us to switch our desired O-band signal between horizontal and vertical polarizations at picosecond-scale speeds with a near-unity switching efficiency of 98.77±0.01%. When random noise is additionally introduced into the quantum channel, our setup attenuates the rate of extraneous detector counts due to noise by up to 18.2 dB , while allowing the polarization-switched signal photons to pass through and be detected by a single-photon detector.

We have also presented a complete numerical model of the Kerr switch, which takes into account the nonlinear evolution of our pump field as it travels through the length of SMF-28. This model allows us to predict the optimal experimental parameters for the Kerr switch to achieve unit switching efficiency, while minimizing the impact of leakthrough noise inherent to the pump. Based on these numerical results, we found that imparting sufficient pre-chirp onto our pump pulses is critical in minimizing nonlinear spectral broadening, which can otherwise result in enough spectral noise to completely saturate our detectors.

6.2 Outlook and future work

Considering the economic significance of implementing QKD in existing telecommunications infrastructure [1, 25], our proposed technique may help enable the transmission of quantum signals through a bright fibre network by reducing the impact due to random noise from coexisting classical channels. This technique is relatively cost-effective; our setup is almost exclusively implemented using off-the-shelf components that can be easily swapped for different signal and pump wavelengths, with our only major custom item being the photonic crystal fibre used to generate our signal pulses. Moreover, the pump pulse energies required are in the nanojoule range, which is well within the optical powers possible by typical commercial pulsed femtosecond lasers [30]. This is especially important since one femtosecond oscillator could be used to simultaneously pump multiple Kerr switches, each corresponding to a different state in a QKD measurement basis.

Many short- and long-term goals follow from this proof-of-principle demonstration. In the short-term, we aim to further optimize the filtering capability of the switch with an appropriate selection of switching fibre length. In the longer-term, we wish to assess the performance of our temporal noise filtering scheme in a telecom-wavelength QKD experiment, and determine the corresponding improvement in secret key rate in a noisy and/or lossy channel for various lengths of channel fibre [1]. We also hope to revisit switching C-band single photons, using appropriate modifications to the numerical model in Chapter 4 to determine and implement the optimal parameters required to avoid the extensive leakthrough noise we previously encountered. Given the relative modularity of our setup, and the close agreement between our numerical model and experimental results, we can also attempt to implement switching for other telecom wavelength bands. The numerical model can also be easily adapted to study Kerr switching in other types of commercial single-mode fibre, as long as the dispersion characteristics of the fibre are known. This work may also enable other applications of telecom-wavelength Kerr switching in addition to noise filtering, such as preparing and measuring QKD qubit states for time-bin encoding [2, 31, 32].

It is important to note that all-optical switching is only one technique to filter noise. Kerr switching would likely continue to be used in addition to passive filtering techniques (such as spectral or spatial mode filtering), in addition to electronic temporal filtering being used as a coarse stage [1]. We remark that the near-unity switching efficiency we report applies only to the signal counts detected by the SNSPDs. As mentioned in Section 3.2.3, we estimate that the total loss of signal photons due to fibre coupling and SNSPD detection efficiencies is approximately 3 dB. Therefore, introducing the switch allows for an increased tolerance to noise at the cost of greater channel loss and reduced secret key rate, which would need to be accounted for in the QKD protocol being employed [1, 20, 25, 33].

Appendix A

Scripts for numerical models

A.1 Pulse propagation model

```
% This code solves the normalized pulse propagation equation with the split-step Fourier method including terms for third-order dispersion, delayed material response, and Raman scattering
% Code follows example procedure by G. P. Agrawal, Nonlinear Fiber Optics, 5th ed. (2013)

clear all; clc; close all;
set(0,'defaultAxesFontSize',14,'defaultAxesFontName','Times New Roman');

%%
%--Specify input parameters
c = 299792458; % [m/s]
lambda0 = 1550e-9; % center wavelength [m]
```

```
w0 = 2*pi*c/(lambda0); % Laser frequency
n0 = 1.4677; % Group index at 1550 nm
n2 = 2.2e-20; % in units of m^2/W
Aeff = pi*(5.2e-6)^2; % m^2; mode field area
gamma = w0*n2/(c*Aeff);
beta2 = -2.082372364144358e-26; % -20.8 ps^2/km in s^2/m
beta3 = 1.260203809851104e-40; % s^3/m
sgnbeta2 = sign(beta2);

%--User-prompted parameters
dlambda_FWHM = input('Enter input pulse bandwidth FWHM in nm: '
   ).*1e-9;
L_fib = input(('Enter fiber length (in m): ')); % Fiber length
   [m].
D2 = input('Enter GDD in fs^2 (GDD > 0 for positive chirp, GDD
   < 0 for negative chirp): ').*(10^-15)^2;
C = D2*(c^2*pi^2 / (lambda0^4 * log(2))) * dlambda_FWHM.^2;

dw0 = (pi/(sqrt(log(2))))*(c/(lambda0^2))*dlambda_FWHM; %
   spectral 1/e half width [rad/s]
T0 = sqrt(1+C^2)/dw0; % 1/e half-width of incident chirped
   pulse [s]
T0_Flimited = 1/dw0; % Half-width of equivalent unchirped pulse
    [s]
T_FWHM = T0*2*sqrt(log(2)); % FWHM of incident chirped pulse [s
   ]
T_FWHMfs = T_FWHM*10^15 % FWHM of incident chirped pulse [fs]
```

```
31
32 % Laser power and repetition rate
33 P_avg = input('Enter average laser power in mW: ').*1e-3; %
      average cw power of laser [W]
34 repRate = 80e6; % repetition rate of laser [Hz]
35
36 T_R = 3e-15; % Raman response first moment / time constant [s]
37 tau_R = T_R / T0; % Normalized Raman response first moment /
      time constant
38 L_D = (T0^2)/abs(beta2); % Dispersion length [m]
39
40 distance_intervals = [0:0.01:1]';
41
42 xi_distance = L_fib.*distance_intervals./L_D; % Dimensionless
      lengths in units of L_D
43
44 P0 = (0.94*P_avg/repRate)/T_FWHM; % Peak power [W]; based on
      300 mW average cw power at 80 MHz rep rate
45 N = sqrt(gamma*P0*T0^2/abs(beta2)); % Soliton order
46 s = 1/(w0*T0);
47
48 % ---set simulation parameters
49 nt = 4096; Tmax = 32; % FFT points and window size % NOTE: you
      may need to adjust the simulation domain to avoid wraparound
       effects.
50 dtau = (2*Tmax)/nt; % step size in tau
51
```

```
%---Normalized time and angular frequency arrays
tau = (-nt/2:nt/2-1)*dtau; % normalized temporal grid, time is
   in units of amplitude 1/e half-width T0
omega = fftshift(-nt/2:nt/2-1)*(pi/Tmax); % normalized omega
   array, in units of 2*pi/T0
freq = fftshift(omega)/(2*pi); % normalized freq. array, in
   units of 1/T0

%---Input field "master" profile
U_input = exp(-0.5*(1+i*C).*tau.^2);
temp_input = fftshift(ifft(U_input)); % Frequency spectrum
spect_input = abs(temp_input).^2; % input spectrum
spect_input = spect_input./max(spect_input); % normalize

figure(1) % Create figure for plotting input vs. final output
   pulses
subplot(3,1,1);
plot (tau.*T0*10^12, abs(U_input).^2, '--k'); hold on; % Time
   domain pulse shape plot (intensity)
axis([-1 1 0 inf]);
xlabel('Time [ps]');
ylabel('Intensity (arb. unit)');
title(["\Delta\lambda_{FWHM} = " + dlambda_FWHM*10^9 + " nm
   ||   T_{FWHM} = " + round(T_FWHMfs,2) + " fs   ||   P_{avg}
   = " + P_avg*1000 + " mW", "C = " + C + "   ||   L_{fibre} =
   " + L_fib + " m"]);
```

```
% title("Input and Output Pulse Shape and Spectrum for L = " +
   xi_distance(end) + " L_{D}");
subplot(3,1,2);
plot ((freq./T0)/10^12, spect_input, '--k'); hold on; %
   Frequency spectrum plot
axis([-50 50 0 1.1]);
xlabel('Frequency shift [THz]');
ylabel('Spectral Power (arb. unit)');

%---Set up simulation intervals
for ii = 1:1:length(distance_intervals)
U = U_input; % Copy "master" input field profile into array
step_num = round(20*xi_distance(ii)*N^2); % No. of z steps
if step_num < 1 % Ensure this value is at least equal to 1.
step_num = 1;
end
dxi = xi_distance(ii)/step_num; % step size in z

%---Store dispersive phase shifts to speedup code
dispersion = exp((0.5*i*sgnbeta2*omega.^2 + i*beta3/(6*abs(
   beta2)*T0).*omega.^3).*dxi); % phase factor
hhz = i*N^2*dxi; % nonlinear phase factor

% % -- Beginning of main loop
% scheme: 1/2N -> D -> 1/2N;

```

```
93  temp1 = U.*exp((abs(U).^2 + (i*s).*(1./U).*(gradient(abs(U)
       .^2.*U)./gradient(tau)) - tau_R.*(gradient(abs(U).^2)./
       gradient(tau)))*hhz/2); % note hhz/2
94
95  % Remove any errors (NaN) due to division by zero
96  NaNtemp1_ind = find(isnan(temp1));
97  if isempty(NaNtemp1_ind) == 0
98  for nn = 1:length(NaNtemp1_ind)
99  temp1(NaNtemp1_ind(nn)) = U(NaNtemp1_ind(nn))*exp((abs(U(
       NaNtemp1_ind(nn)))^2)*hhz/2);
100 end
101 end
102
103 for n = 1:step_num
104 f_temp1 = ifft(temp1).*dispersion;
105 U = fft(f_temp1);
106 temp1 = U.*exp((abs(U).^2 + (i*s).*(1./U).*(gradient(abs(U)
       .^2.*U)./gradient(tau)) - tau_R.*(gradient(abs(U).^2)./
       gradient(tau)))*hhz);
107 % Remove any errors (NaN) due to division by zero
108 NaNtemp1_ind = find(isnan(temp1));
109 if isempty(NaNtemp1_ind) == 0
110 for nn = 1:length(NaNtemp1_ind)
111 temp1(NaNtemp1_ind(nn)) = U(NaNtemp1_ind(nn)).*exp((abs(U(
       NaNtemp1_ind(nn))).^2)*hhz);
112 end
113 end
```

```
114
115 end
116
117 U = temp1.*exp(-(abs(U).^2 + (i*s).*(1./U).*(gradient(abs(U)
       .^2.*U)./gradient(tau)) - tau_R.*(gradient(abs(U).^2)./
       gradient(tau)))*hhz/2);
118
119 % First pass: remove any errors (NaN) due to division by zero
120 NaNU_ind = find(isnan(U));
121 if isempty(NaNU_ind) == 0
122 for nn = 1:length(NaNU_ind)
123 U(NaNU_ind(nn)) = temp1(NaNU_ind(nn)).*exp(-(abs(U(NaNU_ind(nn)
       )).^2)*hhz/2);
124 end
125 end
126
127 % Second pass: any persisting NaN is due to U values so small
       that we
128 % must force exp(-(abs(U(NaNU_ind(nn))).^2)*hhz/2) to evaluate
       to 1.
129 NaNU_ind = find(isnan(U));
130 if isempty(NaNU_ind) == 0
131 for nn = 1:length(NaNU_ind)
132 U(NaNU_ind(nn)) = temp1(NaNU_ind(nn));
133 end
134 end
135
```

```
136 temp1 = fftshift(ifft(U)); % Fourier transform
137 spect1 = abs(temp1).^2; % output spectrum
138 spect1 = spect1./max(spect1); % normalize
139
140 % % -- End of main loop
141
142 U_plot(ii,:) = U;
143 spect_plot(ii,:) = spect1;
144
145 U_plot(1,:) = U_input;
146 spect_plot(1,:) = spect_input;
147
148 end
149
150 %----Plot output pulse shape and spectrum
151
152 X1 = tau.*T0*10^12;
153 Y1 = L_fib.*distance_intervals;
154 Z1 = [abs(U_plot).^2];
155
156 X2 = (freq./T0)/10^12;
157 Y2 = L_fib.*distance_intervals;
158 Z2 = [spect_plot];
159
160 figure(2) % Create figure for plotting evolution of pulse
161 subplot(2,1,1)
162 imagesc(X1, Y1, Z1);
```

```
xlim([-6 6]);
zlim([0 inf]);
xlabel('Time [ps]');
ylabel('Distance [m]');
cb2 = colorbar;
ylabel(cb2,'Intensity (arb. unit)');
zlabel('Intensity (arb. unit)');
title(["GDD = " + round(D2*10^30,0) + " fs^2          C = " + C
   ]);
subplot(2,1,2)
imagesc(X2, Y2, Z2);
xlim([-60 60]);
zlim([0 inf]);
xlabel('Frequency shift [THz]');
ylabel('Distance [m]');
cb1 = colorbar;
ylabel(cb1,'Intensity (arb. unit)');
zlabel('Spectral Power (arb. unit)');
set(gcf, 'Position',  [1245,130,551,808]);

figure(1) % Plot final output pulse shape and spectrum
subplot(3,1,1)
plot(tau.*T0*10^12, abs(U).^2, '-b'); hold off;
legend("Input Pulse","Output Pulse",'Location','northwest');
subplot(3,1,2)
plot((freq./T0)/10^12, spect1, '-b'); hold off;
legend("Input Pulse","Output Pulse",'Location','northwest');
```

```
%----Plot spectrum WRT wavelength
lambdaplot = c./(((freq./T0)+c/lambda0)).*10^9;
subplot(3,1,3)
plot(lambdaplot, spect1, '-b')
xlim([1200 2000])
ylim([0 1.1])
xlabel('Wavelength [nm]');
ylabel('Spectral Power [arb. unit]');
legend("Output Pulse",'Location','northwest');
set(gcf, 'Position',  [175,188,442,614]);

figure(3)
%----Plot spectrum WRT wavelength
lambdaplot = c./(((freq./T0)+c/lambda0)).*10^9;
plot(lambdaplot, spect1, '-b')
% title(["\Delta\lambda_{FWHM} = " + dlambda_FWHM*10^9 + " nm
    ||   T_{FWHM} = " + round(T_FWHMfs,2) + " fs   ||   P_{avg
  } = " + P_avg*1000 + " mW", "C = " + C + "   ||   L_{fibre}
  = " + L_fib + " m"]);
xlim([1200 2000])
ylim([0 1.1])
xlabel('Wavelength [nm]');
ylabel('Spectral intensity [arb. unit]');
set(gcf, 'Position',  [658,561,516,299]);
```

A.2 Kerr switch model with pump pulse evolution

```
% This code solves the normalized pulse propagation equation with the split-step Fourier method
% Includes terms for third order dispersion, delayed material response, and Raman scattering
% Code follows example procedure by G. P. Agrawal, Nonlinear Fiber Optics, 5th ed. (2013)

% Switching code adapted from previous code provided by Kate Fenwick, 2022

% This code computes the cross-correlation of the signal and pump temporal profiles to
% predict the measured count rates vs. delay, due to the finite width of
% the signal pulses. It also plots the switching efficiency defined by the
% phase imparted due to XPM.

clear all; clc;
close all;
set(0,'defaultAxesFontSize',14,'defaultAxesFontName','Times New Roman');
%%
%---Specify parameters of signal and pump fields, and fibre.
c = 299792458; % [m/s]

```

```
lambdaSig_nm = 1295; % Signal wavelength (nm)
lambdaPump_nm = 1550; % Pump wavelength (nm)
lambdaPump = lambdaPump_nm*10^-9; % initial center wavelength
   of pump [m]
lambdaSig = lambdaSig_nm*10^-9; % signal wavelength (m)

w0 = 2*pi*c/(lambdaPump); % Initial centre frequency, pump [rad
   /s]
n0 = 1.4677; % Group index at 1550 nm
n2 = 2.2e-20; % Nonlinear refractive index [m^2/W]

dlambdaPump_FWHM = input('Enter input pump bandwidth FWHM in nm
   : ').*1e-9; % FWHM pump pulse width
D2 = input('Enter GDD in fs^2 (GDD > 0 for positive chirp, GDD
   < 0 for negative chirp): ').*(10^-15)^2;
C = D2*(c^2*pi^2 / (lambdaPump^4 * log(2))) * dlambdaPump_FWHM
   .^2;
dw0 = (pi/(sqrt(log(2))))*(c/(lambdaPump^2))*dlambdaPump_FWHM;
   % spectral 1/e half width [rad/s]
T0 = sqrt(1+C^2)/dw0; % 1/e half-width of incident chirped pump
    pulse [s]
T0_Flimited = 1/dw0; % Half-width of equivalent unchirped pump
   pulse [s]
T_FWHM = T0*2*sqrt(log(2)); % FWHM of incident chirped pump
   pulse [s]
T_FWHMfs = T_FWHM*10^15 % FWHM of incident chirped pump pulse [
   fs]
```

```
36
37
38 T_FWHM_sig = 290e-15; % FWHM of incident chirped pulse [s] (
      Estimated from PCF dispersion curve, assuming 12 nm FWHM, 60
       ps/(nm*km) at 1300 nm, signal wavelength propagating in 28
      cm of fibre)
39 T0_sig =  T_FWHM_sig/(2*sqrt(log(2))); % 1/e half-width of
      incident signal pulse [s]
40
41 % Laser power and repetition rate
42 P_avg = input('Enter average laser power in mW: ').*1e-3; %
      average cw power of laser [W]
43 repRate = 80e6; % repetition rate of laser [Hz]
44
45 MFR = 5.2e-6; % Mode field radius of fibre at 1550 nm [m]
46 Aeff = pi*MFR^2; % [m^2]; mode field area
47 gamma = w0*n2/(c*Aeff); % Nonlinear parameter of fibre [1/(W m)
      ]
48 lambda_ZDW = 1317; % Zero dispersion wavelength of fibre (nm)
49 S0 = 0.088; % Zero dispersion slope of the fiber (ps/(nm^2*km))
50
51 L_fib = input(('Enter fiber length (in m): ')); % Fiber length
      [m].
52
53 %% Walkoff Calculation
54
```

```
55 % We first determine the difference in the reciprocals of the
      walk-off.
56 % This quantity is dw in the B-integral we need to evaluate.
57
58 % We use an approximation for SMF-28 fiber dispersion from
      Corning.
59 lambda = [1200:0.1:1700]; % Wavelength (nm)
60 D = (S0/4).*(lambda - lambda_ZDW^4./(lambda.^3)); % Dispersion
      Parameter [ps/(nm*km)], nominally valid only for 1200 nm to
      1625
61
62 % Integrate to get 1/vg, up to some constant offset. (Only need
       to consider
63 % relative offset. since it is the difference in 1/vg that we
      care about.)
64 vgInv = cumtrapz(lambda, D)*(10^-12)/1000; % Unit conversion
      from [ps/km] to [s/m];
65
66 vgpInv = vgInv(find(lambda==lambdaPump_nm));
67 vgsInv = vgInv(find(lambda==lambdaSig_nm));
68
69 dw = (vgpInv) - (vgsInv); % Walk-off [s/m]
70
71 %% Second- and Third-Order Dispersion Calculation
72
73 D_SI = D.*(10^-12)./(10^-9 * 10^3); % Scale to [s/m^2]
74
```

```
75 dDdlambda = gradient(D)./gradient(lambda);  % Dispersion
     Parameter slope (ps/(nm^2*km))
76 dDdlambda_SI = gradient(D_SI)./gradient(lambda.*10^-9); %
     Scaled to (s/m^3)
77
78 beta2_sig = -(lambdaSig)^2*(D(find(lambda==lambdaSig_nm))
     *(10^-12)/((10^-9)*(10^3)))/(2*pi*c); % GVD parameter for
     signal [s^2/m]
79 beta2_pump = -(lambdaPump)^2*(D(find(lambda==lambdaPump_nm))
     *(10^-12)/((10^-9)*(10^3)))/(2*pi*c); % GVD parameter for
     pump [s^2/m]
80 beta3_pump = ((lambdaPump^2 / (2*pi*c))^2 * dDdlambda_SI(find(
     lambda==lambdaPump_nm))) - (lambdaPump^2 / (2*pi*c))^2 * (4*
     pi*c/lambdaPump^3)*beta2_pump;  % Third-order dispersion of
     fibre. [s^3/m]
81
82 sgnbeta2 = sign(beta2_pump); % Sign of GVD parameter
83
84 LD_sig = T0^2/abs(beta2_sig); % Signal dispersion length (
     Gaussian pulse broadens by a factor of sqrt(2) (m)
85 LD_pump = T0^2/abs(beta2_pump); % Pump dispersion length (m)
86
87 %%
88 % Simulation/pulse propagation equation parameters
89
90 T_R = 3e-15; % Raman response first moment / time constant [s]
     (Esimate from Agrawal (2019)).
```

```
91 tau_R = T_R / T0; % Normalized Raman response first moment /
      time constant
92
93 distance_intervals = [0:0.01:1]'; % Intervals along the fibre
      at which to monitor the pulse evolution.
94 xi = L_fib.*distance_intervals./LD_pump; % Dimensionless
      lengths in units of L_D
95
96 z = xi.*LD_pump; % steps to integrate [m]
97 dw_normed = dw*LD_pump/T0; % Walkoff in units of normalized
      time / normalized distance
98
99 P0 = (0.94*P_avg/repRate)/T_FWHM; % Peak power [W]; based on
      300 mW average cw power at 80 MHz rep rate
100 N = sqrt(gamma*P0*T0^2/abs(beta2_pump)); % Soliton order
101 s = 1/(w0*T0);
102 Lw = T_FWHM_sig/dw; % Walkoff length [m] (Pulses pass through
      each other by one FWHM)
103
104 %---set simulation parameters
105 nt = 8192; Tmax = 32; % FFT points and window size
106 dtau = (2*Tmax)/nt; % step size in tau
107
108 %---Normalized time and angular frequency arrays
109 tau = (-nt/2:nt/2-1)*dtau; % normalized temporal grid, time is
      in units of amplitude 1/e half-width T0
```

```
omega = fftshift(-nt/2:nt/2-1)*(pi/Tmax); % normalized omega
   array, in units of 2*pi/T0
freq = fftshift(omega)/(2*pi); % normalized freq. array, in
   units of 1/T0

%---Input pump field "master" profile
U_input = exp(-0.5*(1+i*C).*tau.^2);
temp_input = fftshift(ifft(U_input)); % Frequency spectrum
spect_input = abs(temp_input).^2; % input spectrum
spect_input = spect_input./max(spect_input); % normalize

U_sig = exp(-0.5.*tau.^2.*(T0/T0_sig)^2); % Field profile of
   signal pulse

figure(1) % Create figure for plotting input vs. final output
   pulses
subplot(3,1,1);
plot (tau.*T0*10^12, abs(U_input).^2, '--k'); hold on; % Time
   domain pulse shape plot (intensity)
axis([-1 1 0 inf]);
xlabel('Time [ps]');
ylabel('Intensity (arb. unit)');
title(["\Delta\lambda_{FWHM} = " + dlambdaPump_FWHM*10^9 + " nm
      ||   T_{FWHM} = " + round(T_FWHMfs,2) + " fs   ||   P_{
   avg} = " + P_avg*1000 + " mW", "C = " + C + "   ||   L_{
   fibre} = " + L_fib + " m"]);
```

```
% title("Input and Output Pulse Shape and Spectrum for L = " +
   xi_distance(end) + " L_{D}");
subplot(3,1,2);
plot ((freq./T0)/10^12, spect_input, '--k'); hold on; %
   Frequency spectrum plot
axis([-50 50 0 1.1]);
xlabel('Frequency shift [THz]');
ylabel('Spectral Power (arb. unit)');

%---Set up simulation intervals
for ii = 1:1:length(distance_intervals)
U = U_input; % Copy "master" input field profile into array
step_num = round(20*xi(ii)*N^2); % No. of z steps
if step_num < 1 % Ensure this value is at least equal to 1.
step_num = 1;
end
dxi = xi(ii)/step_num; % step size in z

%---Store dispersive phase shifts to speedup code
dispersion = exp((0.5*i*sgnbeta2*omega.^2 + i*beta3_pump/(6*abs
   (beta2_pump)*T0).*omega.^3).*dxi); % phase factor
hhz = i*N^2*dxi; % nonlinear phase factor

% % ---Beginning of main loop
% scheme: 1/2N -> D -> 1/2N;

```

```
151 temp1 = U.*exp((abs(U).^2 + (i*s).*(1./U).*(gradient(abs(U)
       .^2.*U)./gradient(tau)) - tau_R.*(gradient(abs(U).^2)./
       gradient(tau)))*hhz/2); % note hhz/2
152
153 % Remove any errors (NaN) due to division by zero
154 NaNtemp1_ind = find(isnan(temp1));
155 if isempty(NaNtemp1_ind) == 0
156 for nn = 1:length(NaNtemp1_ind)
157 temp1(NaNtemp1_ind(nn)) = U(NaNtemp1_ind(nn))*exp((abs(U(
       NaNtemp1_ind(nn)))^2)*hhz/2);
158 end
159 end
160
161 for n = 1:step_num
162 f_temp1 = ifft(temp1).*dispersion;
163 U = fft(f_temp1);
164 temp1 = U.*exp((abs(U).^2 + (i*s).*(1./U).*(gradient(abs(U)
       .^2.*U)./gradient(tau)) - tau_R.*(gradient(abs(U).^2)./
       gradient(tau)))*hhz);
165
166 % First pass: remove any errors (NaN) due to division by zero
167 NaNtemp1_ind = find(isnan(temp1));
168 if isempty(NaNtemp1_ind) == 0
169 for nn = 1:length(NaNtemp1_ind)
170 temp1(NaNtemp1_ind(nn)) = U(NaNtemp1_ind(nn)).*exp((abs(U(
       NaNtemp1_ind(nn))).^2)*hhz);
171 end
```

```
172 end
173
174 end
175
176 U = temp1.*exp(-(abs(U).^2 + (i*s).*(1./U).*(gradient(abs(U)
       .^2.*U)./gradient(tau)) - tau_R.*(gradient(abs(U).^2)./
       gradient(tau)))*hhz/2);
177
178 % First pass: remove any errors (NaN) due to division by zero
179 NaNU_ind = find(isnan(U));
180 if isempty(NaNU_ind) == 0
181 for nn = 1:length(NaNU_ind)
182 U(NaNU_ind(nn)) = temp1(NaNU_ind(nn)).*exp(-(abs(U(NaNU_ind(nn)
       )).^2)*hhz/2);
183 end
184 end
185
186 % Second pass: any persisting NaN is due to U values so small
       that we
187 % must force exp(-(abs(U(NaNU_ind(nn))).^2)*hhz/2) to evaluate
       to 1.
188 NaNU_ind = find(isnan(U));
189 if isempty(NaNU_ind) == 0
190 for nn = 1:length(NaNU_ind)
191 U(NaNU_ind(nn)) = temp1(NaNU_ind(nn));
192 end
193 end
```

```
194
195 temp1 = fftshift(ifft(U)); % Fourier transform
196 spect1 = abs(temp1).^2; % output spectrum
197 spect1 = spect1./max(spect1); % normalize
198
199 % % --End of main loop
200
201 U_plot(ii,:) = U;
202 spect_plot(ii,:) = spect1;
203
204 U_plot(1,:) = U_input;
205 spect_plot(1,:) = spect_input;
206
207 end
208
209 %%
210 %----Plot output pulse shape and spectrum
211
212 X1 = tau.*T0*10^12;
213 Y1 = L_fib.*distance_intervals;
214 Z1 = [abs(U_plot).^2];
215
216 X2 = (freq./T0)/10^12;
217 Y2 = L_fib.*distance_intervals;
218 Z2 = [spect_plot];
219
220 figure(2) % Create figure for plotting evolution of pulse
```

```
subplot(2,1,1)
% s = surf(X1, Y1, Z1);
% waterfall(X1, Y1, Z1);
% s.EdgeColor = 'none';
imagesc(X1, Y1, Z1);
xlim([-4 4]);
zlim([0 inf]);
xlabel('Time [ps]');
ylabel('Distance [m]');
zlabel('Intensity (arb. unit)');
% title("Pulse evolution for L = " + xi_distance + " L_{D}");
title(["\Delta\lambda_{FWHM} = " + dlambdaPump_FWHM*10^9 + " nm
      ||   T_{FWHM} = " + round(T_FWHMfs,2) + " fs   ||   P_{
   avg} = " + P_avg*1000 + " mW", "C = " + C + "   ||   L_{
   fibre} = " + L_fib + " m"]);
subplot(2,1,2)
imagesc(X2, Y2, Z2);
xlim([-50 50]);
zlim([0 inf]);
xlabel('Frequency shift [THz]');
ylabel('Distance [m]');
zlabel('Spectral Power (arb. unit)');
set(gcf, 'Position',  [1299,119,437,614]);

figure(1) % Plot final output pulse shape and spectrum
subplot(3,1,1)
plot(tau.*T0*10^12, abs(U).^2, '-b'); hold off;
```

```
245 legend("Input Pulse","Output Pulse",'Location','northwest');
246 subplot(3,1,2)
247 plot((freq./T0)/10^12, spect1, '-b'); hold off;
248 legend("Input Pulse","Output Pulse",'Location','northwest');
249 %----Plot spectrum WRT wavelength
250 lambdaplot = c./(((freq./T0)+c/lambdaPump)).*10^9;
251 subplot(3,1,3)
252 plot(lambdaplot, spect1, '-b')
253 xlim([1200 2000])
254 ylim([0 1.1])
255 xlabel('Wavelength [nm]');
256 ylabel('Spectral intensity [arb. unit]');
257 legend("Output Pulse",'Location','northwest');
258 set(gcf, 'Position',  [81,132,439,614]);
259
260 figure(3)
261 %----Plot spectrum WRT wavelength
262 lambdaplot = c./(((freq./T0)+c/lambdaPump)).*10^9;
263 plot(lambdaplot, spect1, '-b')
264 ylim([0 1.1])
265 % semilogy(lambdaplot, spect1, '-b') % Plot vs log scale to see
      noise floor
266 xlim([1200 2000])
267 title(["\Delta\lambda_{FWHM} = " + dlambdaPump_FWHM*10^9 + " nm
      ||   T_{FWHM} = " + round(T_FWHMfs,2) + " fs   ||   P_{
    avg} = " + P_avg*1000 + " mW", "C = " + C + "   ||   L_{
    fibre} = " + L_fib + " m"]);
```

```
xlabel('Wavelength [nm]');
ylabel('Spectral Power [arb. unit]');
set(gcf, 'Position',  [663,548,464,278]);

%%
%%%% SWITCH CODE BELOW

%% Calculate switch efficiency vs time

% Calculate pump power
peakPow = 0.94*P_avg*(1/repRate)./T_FWHM; % Peak power
I0 = peakPow/Aeff; % Input pump intensity peak (W/m^2) as a
   function of z
Upulse = (P_avg/repRate)*10^9; % Pulse energy in nJ

% Iterate through delay steps T, integrate phi through whole
   fiber for each delay step
phi = []; % Nonlinear phase gained for Gaussian pulse

for ii = 1:length(tau)
for nn = 1:length(xi)
overlapIndex = find( abs(tau - (tau(ii) - dw_normed*xi(nn))) <
   dtau/2 );
if isempty(overlapIndex) % Pulse is "outside" the length window
Ipump(nn) = 0;
else
```

```
291 Ipump(nn) = I0.*Z1(nn, overlapIndex); % Note: Z1 contains
      normalized INTENSITY values, not amplitude (already squared)
292 end
293 end
294 IT(ii,:) = Ipump; % For diagnosing shape of I(T,z) = I(T-dw*z)
      if needed
295 phi(ii) = 8/3*pi*n2/lambdaSig*trapz(z,Ipump); % Integrate WRT
      SI units
296 end
297
298 % Calculate switch efficiency ("intrinsic switch response")
299 SwitchEfficiency = (sin(phi/2)).^2;
300
301 %%
302 % With appropriate delay, the switch efficiency to plot vs
      power is determined at the centre of the switching
      efficiency trace profile.
303
304 figure(4)
305 plot(-(tau-dw_normed*L_fib./LD_pump/2)*T0*10^12,
      SwitchEfficiency, '-r','LineWidth',2) % Plotting vs pump
      delay, relative to the signal. "Negative" delay means the
      pump arrives *early*.
306 hold on
307 plot(-(tau-dw_normed*L_fib./LD_pump/2)*T0*10^12, 1-
      SwitchEfficiency, '-b','LineWidth',2)
308 ylim([0 1.1])
```

```
yticks([0:0.2:1])
xlim([-3.25 3.25])
xlabel('Pump Delay (ps)');
ylabel('Switching Efficiency');
in_titlestr = sprintf('Efficiency, Pulse Energy = %.2f nJ',
   Upulse);
% title(in_titlestr);
legend("Switched","Unswitched",'Location','east','fontsize',10)
   ;
set(gcf, 'Position', [350,137,520,300])
hold off;

%%

SwitchCounts = xcorr(SwitchEfficiency, abs(U_sig).^2)/trapz(abs
   (U_sig).^2); % Measured curve of observed counts is given by
    the cross-correlation between the signal and pump.
% e.g. if SwitchCounts reaches unity, but with no flat top,
   then the
% flat-top portion of SwitchEfficiency exactly matches the
   complete width of the signal
% Note: here the signal is being time-shifted, so it is being
   plotted
% relative to signal delay

tau_xcorr = [-length(SwitchCounts)/2:1:(length(SwitchCounts)
   /2-1)].*dtau;
```

```
328
329 figure(5)
330 plot(-(tau_xcorr-dw_normed*L_fib./LD_pump/2)*T0*10^12,
      SwitchCounts, '-r','LineWidth',2) % Plotting vs pump delay,
      relative to the signal. "Negative" delay means the pump
      arrives *early*.
331 hold on
332 plot(-(tau_xcorr-dw_normed*L_fib./LD_pump/2)*T0*10^12, 1-
      SwitchCounts, '-b','LineWidth',2)
333 ylim([0 1.1])
334 yticks([0:0.2:1])
335 xlim([-3.25 3.25])
336 xlabel('Pump Delay (ps)');
337 ylabel('Count Rate (arb. unit)');
338 in_titlestr = sprintf('Count Rate, Pulse Energy = %.2f nJ',
      Upulse);
339 % title(in_titlestr);
340 legend("Switched","Unswitched",'Location','east','fontsize',10)
      ;
341 set(gcf, 'Position', [900,137,520,300])
342 hold off;
343
344 simtrace = [SwitchCounts; -(tau_xcorr-dw_normed*L_fib./LD_pump
      /2)*T0*10^12];
```

References

[1] F. Bouchard, D. England, P. J. Bustard, K. L. Fenwick, E. Karimi, K. Heshami, and B. Sussman, "Achieving Ultimate Noise Tolerance in Quantum Communication", Phys. Rev. Appl. **15**, 024027 (2021).

[2] D. England, F. Bouchard, K. Fenwick, K. Bonsma-Fisher, Y. Zhang, P. J. Bustard, and B. J. Sussman, "Perspectives on all-optical Kerr switching for quantum optical applications", Applied Physics Letters **119**, 160501 (2021).

[3] C. Kupchak, J. Erskine, D. England, and B. Sussman, "Terahertz-bandwidth switching of heralded single photons", Opt. Lett. **44**, 1427 (2019).

[4] C. H. Bennett and G. Brassard, "Quantum cryptography: Public key distribution and coin tossing", Theoretical Computer Science **560**, Theoretical Aspects of Quantum Cryptography – celebrating 30 years of BB84, 7 (2014).

[5] M. A. Nielsen and I. L. Chuang, *Quantum Computation and Quantum Information: 10th Anniversary Edition* (Cambridge University Press, USA, 2011).

[6] R. W. Boyd, *Nonlinear Optics*, 4th ed. (Academic Press, 2020).

[7] G. P. Agrawal, *Nonlinear Fiber Optics*, 6th ed. (Academic Press, 2019).

[8] E. Pelucchi, G. Fagas, I. Aharonovich, D. Englund, E. Figueroa, Q. Gong, H. Hannes, J. Liu, C.-Y. Lu, N. Matsuda, J.-W. Pan, F. Schreck, F. Sciarrino, C. Silberhorn, J. Wang, and K. D. Jöns, "The potential and global outlook of integrated photonics for quantum technologies", Nature Reviews Physics **4**, 194 (2021).

[9] Government of Canada, *Canada's National Quantum Strategy*, (2022) https://ised-isde.canada.ca/site/national-quantum-strategy/en/canadas-national-quantum-strategy.

[10] G. P. Agrawal, *Fiber-Optic Communication Systems*, 5th ed. (Wiley, 2021).

[11] R. L. Rivest, A. Shamir, and L. Adleman, "A Method for Obtaining Digital Signatures and Public-Key Cryptosystems", Commun. ACM **21**, 120 (1978).

[12] H.-K. Lo, M. Curty, and K. Tamaki, "Secure quantum key distribution", Nature Photonics **8**, 595 (2014).

[13] P. W. Shor, "Polynomial-Time Algorithms for Prime Factorization and Discrete Logarithms on a Quantum Computer", SIAM Journal on Computing **26**, 1484 (1997).

[14] Y. Cao, Y. Zhao, Q. Wang, J. Zhang, S. X. Ng, and L. Hanzo, "The Evolution of Quantum Key Distribution Networks: On the Road to the Qinternet", IEEE Communications Surveys & Tutorials **24**, 839 (2022).

[15] R. Bala, S. Asthana, and V. Ravishankar, "Combating errors in quantum communication: an integrated approach", Scientific Reports **13**, 2979 (2023).

[16] C. E. Shannon, "Communication theory of secrecy systems", The Bell System Technical Journal **28**, 656 (1949).

[17] W. K. Wootters and W. H. Zurek, "A single quantum cannot be cloned", Nature **299**, 802 (1982).

[18] E. Diamanti, H.-K. Lo, B. Qi, and Z. Yuan, "Practical challenges in quantum key distribution", npj Quantum Information **2**, 16025 (2016).

[19] V. Zapatero, T. van Leent, R. Arnon-Friedman, W.-Z. Liu, Q. Zhang, H. Weinfurter, and M. Curty, "Advances in device-independent quantum key distribution", npj Quantum Information **9**, 10 (2023).

[20] M. Takeoka, S. Guha, and M. M. Wilde, "Fundamental rate-loss tradeoff for optical quantum key distribution", Nature Communications **5**, 5235 (2014).

[21] K. A. Patel, J. F. Dynes, I. Choi, A. W. Sharpe, A. R. Dixon, Z. L. Yuan, R. V. Penty, and A. J. Shields, "Coexistence of High-Bit-Rate Quantum Key Distribution and Data on Optical Fiber", Phys. Rev. X **2**, 041010 (2012).

[22] D. Bacco, M. Canale, N. Laurenti, G. Vallone, and P. Villoresi, "Experimental quantum key distribution with finite-key security analysis for noisy channels", Nature Communications **4**, 2363 (2013).

[23] K. Tamaki, M. Curty, G. Kato, H.-K. Lo, and K. Azuma, "Loss-tolerant quantum cryptography with imperfect sources", Phys. Rev. A **90**, 052314 (2014).

[24] A. Boaron, G. Boso, D. Rusca, C. Vulliez, C. Autebert, M. Caloz, M. Perrenoud, G. Gras, F. Bussières, M.-J. Li, D. Nolan, A. Martin, and H. Zbinden, "Secure Quantum Key Distribution over 421 km of Optical Fiber", Phys. Rev. Lett. **121**, 190502 (2018).

[25] S. Wang, Z.-Q. Yin, D.-Y. He, W. Chen, R.-Q. Wang, P. Ye, Y. Zhou, G.-J. Fan-Yuan, F.-X. Wang, W. Chen, Y.-G. Zhu, P. V. Morozov, A. V. Divochiy, Z. Zhou, G.-C. Guo, and Z.-F. Han, "Twin-field quantum key distribution over 830-km fibre", Nature Photonics **16**, 154 (2022).

[26] R. Valivarthi, M. G. Puigibert, Q. Zhou, G. H. Aguilar, V. B. Verma, F. Marsili, M. D. Shaw, S. W. Nam, D. Oblak, and W. Tittel, "Quantum teleportation across a metropolitan fibre network", Nature Photonics **10**, 676 (2016).

[27] Corning Incorporated, "Single-Mode Dispersion Measurement Method MM26", (2001).

[28] Corning Incorporated, "Corning SMF-28 Ultra Optical Fiber Product Information", (2013).

[29] N. Dimitrov, P. Lazarova, L. Stoyanov, I. Stefanov, and A. Dreischuh, "Dispersion control in a folded 4-f system for shaping femtosecond laser pulses", Proc. SPIE 10226, 19th International Conference and School on Quantum Electronics: Laser Physics and Applications, 102261D (2017).

[30] R. Paschotta, *Femtosecond Lasers*, (2005) https://www.rp-photonics.com/femtosecond_lasers.html.

[31] F. Bouchard, D. England, P. J. Bustard, K. Heshami, and B. Sussman, "Quantum Communication with Ultrafast Time-Bin Qubits", PRX Quantum **3**, 010332 (2022).

[32] F. Bouchard, K. Bonsma-Fisher, K. Heshami, P. J. Bustard, D. England, and B. Sussman, "Measuring ultrafast time-bin qudits", Phys. Rev. A **107**, 022618 (2023).

[33] R. Wang, Z.-Q. Yin, F.-Y. Lu, S. Wang, W. Chen, C.-M. Zhang, W. Huang, B.-J. Xu, G.-C. Guo, and Z.-F. Han, "Optimized protocol for twin-field quantum key distribution", Communications Physics **3**, 149 (2020).